Quantum theory of plasmon-mediated light emission by non-Gaussian noise of a tunnel junction

Doctoral thesis for obtaining the

academic degree Doctor of

Natural Sciences

submitted by

Fei Xu

at the

Faculty of Science

Department of Physics

Konstanz, 2017

Date of the oral examination: 19/07/2017

1. Reviewer: Prof. Alfred Leitenstorfer

2. Reviewer: Prof. Wolfgang Belzig

3. Reviewer: Prof. Guido Burkard

"The real voyage of discovery consists not in seeking new lands but seeing with new eyes."

Marcel Proust

Abstract

In this thesis, motivated by the recent experiments that detect the light emission from the STM junctions and observe the unusual but interesting photon emission related to electron-electron interactions, we propose and establish a model circuit and theoretically investigate these enhanced light emission from a tunnel junction coupled to a surface plasmon polariton (SPP).

It is known that the current noise can be characterized as the photon emission or absorption probability due to the coupling between the environment circuit and the current. To model and specify this coupling between the electrical current and the electromagnetic environment, by introducing the phase operator $\varphi(t) = \frac{e}{\hbar}\int_{-\infty}^{t} dt' U(t')$ to describe the voltage fluctuation across the junction, we can transfer the calculation of the tunnelling rate Γ into the evaluation of the correlation function $\langle e^{i\varphi(t)} e^{-i\varphi(0)} \rangle$. For a simple case, such as a harmonic environment where the equilibrium density matrix in the $\varphi-$ representation is a Gaussian, it just follows the $P(E)$ theory, offering the maximum energy for tunneling at the bias voltage eV, as we all understand and expect.

Next, we go further, beyond the limit of the Gaussian action, and turn into checking the non-Gaussian contributions to the light emission. By means of the Keldysh path integral method, we expand the action of the tunnel conductor up to the fourth order of the phase φ. Under the assumption $g_c z_\omega^2 \ll 1$ motivated by the experiment, in the lowest order of tunnel conductance g_c and the weak coupling to the detector α, we derive the expression for the total transition rate of the tunneling electrons.

Through the numerical plotting, we analyse the properties and find out that the non-Gaussian terms is responsible for the overbias light emission shown in the experiments and our work well reproduces the experimental observation, clearly exhibiting the emitted photons with energy larger than the bias voltage $h\nu > eV$.

Moreover, we continue the studying and check how the temperature affects the contribution. At zero temperature, the energy threshold at eV is evidently displayed while it is sensitively smearing out by the increase of the temperature, due to the softening of the Fermi edge. In addition, we also find a possibility to distinguish the Gaussian and non-Gaussian contribution by setting the plasmon resonance far from the bias voltage.

With the study of the intensity properties, we find that the thermally induced overbias light emission can overmask the contribution from the quantum noise, but can be distinguished by characteristic spectral differences.

Finally, we expand furthermore to the six-order fluctuation, giving rise to the three-electron tunneling processes, which is considered by the experiments as well. And from the numerical fitting to the experiments, we show a fairly nice agreement and propose a good way to explain the unusual experimental phenomena closing to the conductance quantum G_0 as well as extending our calculations beyond the tunneling limit $F \neq 1$.

Zusammenfassung

Diese theoretische Arbeit ist durch die jüngsten Experimente zur Detektion der Lichtemission aus STM-Kontaken und der Beobachtung der ungewöhnlichen, aber interessanten Photonenemission im Zusammenhang mit Elektron-Elektronen-Wechselwirkungen motiviert. Hierzu schlagen wir eine geeignete Modellschaltung vor und untersuchen diese Lichtemissionen theoretisch an einem Tunnel-Übergang, der mit einer Oberflächenplasmon-Polariton (SPP)-Mode gekoppelt ist.

Es ist bekannt, dass das Storm= Rauschen aufgrund der Kopplung zwischen einer Umgebung und dem Strom durch die Photonenemissions- oder Absorptionrate charakterisiert werden kann. Um diese Kopplung zwischen dem elektrischen Strom und der elektromagnetischen Umgebung zu modellieren und zu spezifizieren, kann durch Einführen des Phasenoperators $\varphi(t) = \frac{e}{\hbar}\int_{-\infty}^{t} dt' U(t')$ zur Beschreibung der Spannungsfluktuationen an dem Kontakt die Berechnung der Tunnelrate Γ in die Auswertung der Korrelationsfunktion $\langle e^{i\varphi(t)} e^{-i\varphi(0)} \rangle$ übertragen werden. Für den einfachen Fall, einer harmonischen Umgebung, folgt die P(E)-Theorie und es zeigt sich, dass die maximale Energie zum Tunneln durch die Spannung eV gegeben ist, wie man erwartet.

Als nächstes gehen wir, über die Gaussche Wirkung hinaus, und behandeln die nicht-Gausschen Beiträge zur Lichtemission. Mit Hilfe der Keldysh-Pfad-Integralmethode erweitern wir die Wirkung des Tunnelkontaktes bis zur vierten Ordnung der Phase φ. Mit geeigneten Approximationen leiten wir den Beitrag niedrigster Ordnung in der Tunnelleitfähigkeit g_c und im Grenzfall der schwachen Kopplung zum Detektor α den Ausdruck für die Gesamtemissions ab.

Durch numerisches Auswerten analysieren wir die Eigenschaften der Lichtemission und finden heraus, dass die nicht-Gauss'schen Fluktuationen für die Lichtemission. Im Bereich oberhalb eV verantwortlich ist Unsere Arbeite reproduziert auch die experimentellen Ergebnisse, die einen deutlichen Knick bei der Vorspannung eV zeigen.

Darüber hinaus haben wir den Einfluss einer endlichen Temperatur untersucht. Bei Null Temperatur wird die Energieschwelle bei eV deutlich angezeigt, während sie aufgrund der Verschmierung der Fermikante bei endlichen Temperaturen aufgeweicht wird. Damit zeigen wir auch eine Möglichkeit, die Gaussschen

und Nichtgaussschen durch Einstellen der Plasmonresonanz abseits der Schwellenspannung zu unterscheiden.

Mit der Untersuchung der Intensitätseigenschaften finden wir, dass die thermisch induzierte hochenergetische Lichtemission den Quanteneffekt überdecken kann, sich aber charakteristisch in der spektralen Verteilung unterscheidet.

Schliesslich erweitern wir weiter auf die Fluktuation der sechs Ordnungen, was zu den Dreielektronentunnelprozessen führt, die auch in Experimenten beobachted werden. Mit der numerischen Anpassung an die Experimente können wir die Übereinstimmung mit unserer Theorie zeigen.

Acknowledgements

I would like to express my deep gratitude to my supervisor Prof. Wolfgang Belzig for his patience, excellent guidance and supervision during my PhD studies. After such a long time working with him, I've learned a lot from the frequent and very helpful discussions. Thanks for all that and much more.

I wish to thank Dr. Federica Haupt who introduced the background knowledge to me, and Dr. Cecilia Holmqvist and Dr. Gianluca Rastelli who helped me a lot to check the paper.

I am also very thankful to Dr. Gianluca Rastelli, Dr. Milena Filipovic, Dr. Peter Machon, Johannes Buelte for useful discussions and help and the other present and former members of our research group, and all colleagues who enrich my experience and understanding of work and outside work.

Many many thanks to our secretaries Sabine Lucas and Letizia Bruscaglioni for their kindness, help and assistance.

I sincerely thank the Welcome Center Team at the University of Konstanz, for their help, warmhearted, support, and always nice and welcoming atmosphere every time when I have problems during the daily life.

I gratefully acknowledge support from my parents, my sister and my teacher in college for their love, care, and encouragement throughout this journey.

Contents

Chapter 1

Introduction

The idea of this thesis originates from the photon detector, which absorbs the emitted photons and count the number of them within a given time, thus obtaining the counting distribution by repeating such measurements. As we know, all electrons in a circuit can not be absorbed, but we can make use of the coupling between the electrical current I and the electromagnetic field, then leading to the distribution of the transferred charge. There are such many experiments in nanostructures extracting fruitful information from the measured current fluctuations. Nevertheless, it provides a theoretical scheme to develop this knowledge by studying the statistics of the transferred charge.

In this introduction chapter, we list some background knowledge about the tunneling mechanism with or without an environment and exhibit the method we'll use to treat and calculate such photon emission or absorption spectrum problems.

1.1 Keldysh Path Integral Methods

The path integral (PI) is a formulation of quantum mechanics developed by Feynman in 1948 [1] based on the fact that the propagator can be written as a sum over all possible paths, not just the classic one, between the initial and final points. The quantum particle takes all paths and each path contributes $e^{iS/\hbar}$ with S is the action along the path. Although most if not all calculations in quantum mechanics

can be done much more easily by using the standard formulations by Schroedinger, Heisenberg and others, the path integral turns out to be considerably more useful in more complicated situations, such as the field theory [2–5].

As we have learned in quantum mechanics [6, 7], the propagator $K(q',t;q,0)$ from the initial spacetime point $(q,0)$ to the final point (q',t) is expressed as the amplitude $\langle q'|\psi(T)\rangle = \langle q'|e^{-iHt}|q\rangle$ (here $\hbar$ is set to be 1), and finally via the PI can be derived as

$$K(q',t;q,0) \equiv \langle q'|e^{-iHt}|q\rangle = \int \mathcal{D}q(t)e^{iS[q(t)]}. \tag{1.1}$$

In quantum field theory, the Green's function or correlation function generally formed by the vacuum expectation value of a time-ordered product of Heisenberg field operators [8], can have a PI expression as:

$$G(t,t') = \langle 0|Tq(t)q(t')|0\rangle = \frac{\int \mathcal{D}qq(t)q(t')e^{iS}}{\int \mathcal{D}qe^{iS}}. \tag{1.2}$$

If we consider the time t to be a complex number, and assume it to be pure imaginary, so that we can write $t = -i\beta$, where $\beta = 1/k_BT$ is real. Then the Eq. 1.1 becomes

$$K(q',-i\beta;q,0) \equiv \langle q'|e^{-\beta H}|q\rangle = \sum_j e^{-\beta E_j}\langle q'|j\rangle\langle j|q\rangle, \tag{1.3}$$

with E_j is the energy of the state $|j\rangle$. By putting $q' = q$ and doing the integral over q, we hence get

$$\int dqK(q,-i\beta;q,0) = \sum_j e^{-\beta E_j} = Tr[e^{-\beta H}] \equiv Z, \tag{1.4}$$

which shows that the propagator evaluated at negative imaginary time is related to the partition function. And this also means that the path integral proposes a nice way to do statistical mechanics [9, 10].

In the out-of-equilibrium many-body system [8, 11], it is useful to introduce the Keldysh formalism. This formulation is usually starting from an interacting Hamiltonian $H = H_0 + H_I(t)$ and assumes that the system begins at $t = -\infty$ at the

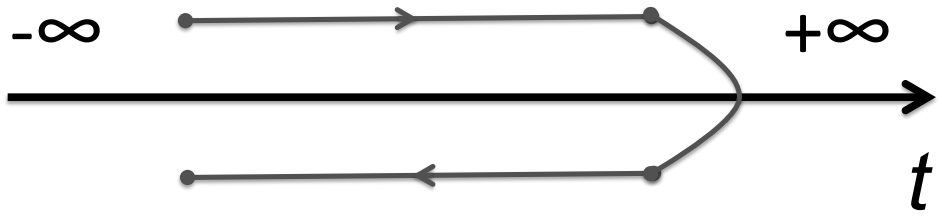

FIGURE 1.1: The closed time contour $\mathcal{C}$. Time evolution follows the forward and backward branches.

ground (or equilibrium) state of the non-interacting Hamiltonian H_0. And then adiabatically switching the interaction on, it arrives at $t = +\infty$ at the unknown final state. The Keldysh technique is to establish the time evolution along the two-branch contour $\mathcal{C}$ (Fig. 1.1), thus no matter what the state is at $t = +\infty$, after the backward evolution the system goes back to the known initial state anyway.

1.1.1 Boson system

For the simplest bosonic system, which is equivalent to a harmonic oscillator $H = \omega_0 a^\dagger a$ with $a, a^\dagger$ being the bosonic annihilation and creation operators satisfying the commutation relation $[a, a^\dagger] = 1$. The bosonic coherent state $|\varphi\rangle$ is defined as the eigenstate of the annihilation operator $a|\varphi\rangle = \varphi|\varphi\rangle$ ($\langle\varphi|a^\dagger = \langle\varphi|\bar{\varphi}$), following $\langle\varphi|H(a^\dagger, a)|\varphi'\rangle = H(\bar{\varphi}, \varphi')\langle\varphi|\varphi'\rangle$. One can split the real correlated bosonic field $\varphi(t)$ into two components $\varphi^+(t)$ and $\varphi^-(t)$ that belong to the forward and backward parts of the time contour respectively.

Then with the definition of the Green functions

$$G(t, t') = -i \int \mathcal{D}\bar{\varphi}\varphi e^{iS[\bar{\varphi},\varphi]}\varphi(t)\bar{\varphi}(t') \equiv -i\langle\varphi(t)\bar{\varphi}(t')\rangle, \tag{1.5}$$

and the assumption that the time on the backward part is always after that on the forward part, one can write down the Green's functions as [12–14]:

$$\begin{aligned} G^T(t,t') &= -i\langle\varphi^+(t)\bar{\varphi}^+(t')\rangle = \frac{Tr\{T[a(t)a^\dagger(t')]\rho_0\}}{Tr\{\rho_0\}} \\ &= \theta(t-t')G^>(t,t') + \theta(t'-t)G^<(t,t'); \end{aligned} \tag{1.6}$$

$$\begin{aligned} G^<(t,t') &= -i\langle\varphi^+(t)\bar{\varphi}^-(t')\rangle = \frac{Tr\{a^\dagger(t')a(t)\rho_0\}}{Tr\{\rho_0\}} \\ &= -ine^{-i\omega_0(t-t')}; \end{aligned} \tag{1.7}$$

$$\begin{aligned} G^>(t,t') &= -i\langle\varphi^-(t)\bar{\varphi}^+(t')\rangle = \frac{Tr\{a(t)a^\dagger(t')\rho_0\}}{Tr\{\rho_0\}} \\ &= -i(n+1)e^{-i\omega_0(t-t')}; \end{aligned} \tag{1.8}$$

$$\begin{aligned} G^{\tilde{T}}(t,t') &= -i\langle\varphi^-(t)\bar{\varphi}^-(t')\rangle = \frac{Tr\{\tilde{T}[a(t)a^\dagger(t')]\rho_0\}}{Tr\{\rho_0\}} \\ &= \theta(t'-t)G^>(t,t') + \theta(t-t')G^<(t,t') \end{aligned} \tag{1.9}$$

where $\rho_0 = \exp\{-\beta(H-\mu N)\} = \exp\{-\beta(\omega_0-\mu)a^\dagger a\}$ is the equilibrium density matrix and n is the bosonic occupation number. Here, the symbols T and $\tilde{T}$ mean the time-ordering and the anti-time-ordering, respectively. So that, the action S can be obtained as

$$S[\bar{\varphi},\varphi] = \iint dtdt' \begin{pmatrix} \bar{\varphi}^+(t) & \bar{\varphi}^-(t) \end{pmatrix} \begin{pmatrix} G^T & G^< \\ G^> & G^{\tilde{T}} \end{pmatrix}^{-1}_{(t,t')} \begin{pmatrix} \varphi^+(t') \\ \varphi^-(t') \end{pmatrix}. \tag{1.10}$$

By introducing the Keldysh rotation, we can define the new fields ϕ and χ:

$$\phi = \frac{1}{2}(\varphi^+ + \varphi^-), \qquad \chi = \varphi^+ - \varphi^-. \tag{1.11}$$

And this algebraic manipulation on the Green's functions can be written as

$$\begin{aligned} -i\langle\alpha(t)\beta(t')\rangle &= \begin{pmatrix} \frac{1}{2}(G^< + G^>) & \theta(t-t')(G^> - G^<) \\ \theta(t'-t)(G^< - G^>) & 0 \end{pmatrix} \\ &\equiv \begin{pmatrix} G^K & G^R \\ G^A & 0 \end{pmatrix} \\ &= \begin{pmatrix} -i\frac{(1+2n)}{2}e^{-i\omega_0(t-t')} & -i\theta(t-t')e^{-i\omega_0(t-t')} \\ i\theta(t'-t)e^{-i\omega_0(t-t')} & 0 \end{pmatrix} \end{aligned} \tag{1.12}$$

where $\alpha, \beta = \phi, \chi$ and hereby the Eq. 1.10 becomes

$$S[\phi,\chi] = \iint dtdt' \begin{pmatrix} \bar{\phi}(t) & \bar{\chi}(t) \end{pmatrix} \begin{pmatrix} 0 & (G^A)^{-1} \\ (G^R)^{-1} & (G^{-1})^K \end{pmatrix}_{(t,t')} \begin{pmatrix} \phi(t') \\ \chi(t') \end{pmatrix}, \quad (1.13)$$

in which the matrix of the inverted Green functions has the expression after doing the Fourier transform with respect to $(t - t')$:

$$\begin{aligned} \begin{pmatrix} 0 & (G^A)^{-1} \\ (G^R)^{-1} & (G^{-1})^K \end{pmatrix} &= \begin{pmatrix} \frac{2n+1}{2}(\frac{1}{\omega-\omega_0+i\eta} - \frac{1}{\omega-\omega_0-i\eta}) & \frac{1}{\omega-\omega_0+i\eta} \\ \frac{1}{\omega-\omega_0-i\eta} & 0 \end{pmatrix}^{-1} \\ &= \begin{pmatrix} 0 & \omega-\omega_0-i\eta \\ \omega-\omega_0+i\eta & (2n+1)i\eta \end{pmatrix}. \end{aligned} \quad (1.14)$$

In addition, for the complex field $\varphi(t)$, it can be parameterized by its real and imaginary parts which are respectively characterised with real fields $p(t)$ and $q(t)$ [14]. Therefore the action can take the form of the Feynman Lagrangian action of the harmonic oscillator, written on the Keldysh contour

$$S[q(t)] = \int_{\mathcal{C}} dt[\frac{1}{2}(\dot{q}(t))^2 - \frac{\omega_0^2}{2}q^2(t)]. \quad (1.15)$$

Next like the above treatment, one can split the real $q(t)$ field into two components: $q^+(t)$ and $q^-(t)$, and also perform the similar Keldysh rotation: $q^{\pm} = q_1 \pm q_2$. So the action takes the form:

$$S[q_1,q_2] = \int dt[-2q_2\frac{d^2q_1}{dt^2} - U(q_1+q_2) + U(q_1-q_2)] \quad (1.16)$$

with the arbitrary single particle potential $U(q)$ is used to instead of $\frac{\omega_0^2}{2}q^2$, which is just the Keldysh form of the Feynman path integral.

1.1.2 Fermion system

For a fermion system, due to the Pauli exclusion principle, for a single quantum state with energy ϵ_0, it is occupied either by one particle or zero. The Hamiltonian is formed as $H = \epsilon_0 c^\dagger c$ with $c, c^\dagger$ being the fermonic annihilation and creation

operators satisfying the anti-commutation relation $\{c, c^\dagger\} = 1$. Unlike the boson system has the bosonic coherent state φ, we need to introduce the fermonic coherent state [12] $|\psi\rangle$ parameterised by a Grassman number ψ, which is the eigenstate of the annihilation operator, giving

$$\begin{aligned} c|\psi\rangle &= \psi|\psi\rangle, && (1.17)\\ \langle\psi|c^\dagger &= \langle\psi|\bar{\psi}, && (1.18)\\ \langle\psi|H(c^\dagger, c)|\psi'\rangle &= H(\bar{\psi}, \psi)\langle\psi|\psi'\rangle. && (1.19) \end{aligned}$$

The Grassman numbers ψ and $\bar{\psi}$ are unrelated numbers and the Grassman integrals are defined as

$$\begin{aligned} \int d\psi 1 &= 0, && (1.20)\\ \int d\psi\psi &= 1. && (1.21) \end{aligned}$$

Similarly, we can write down the fermionic Green's functions as

$$\begin{aligned} \mathcal{G}^T(t,t') &= -i\langle\psi^+(t)\bar{\psi}^+(t')\rangle = \frac{Tr\{T[c(t)c^\dagger(t')]\rho_0\}}{Tr\{\rho_0\}}\\ &= \theta(t-t')\mathcal{G}^>(t,t') + \theta(t'-t)\mathcal{G}^<(t,t'); && (1.22)\\ \mathcal{G}^<(t,t') &= -i\langle\psi^+(t)\bar{\psi}^-(t')\rangle = \frac{Tr\{c^\dagger(t')c(t)\rho_0\}}{Tr\{\rho_0\}}\\ &= in_F e^{-i\epsilon_0(t-t')}; && (1.23)\\ \mathcal{G}^>(t,t') &= -i\langle\psi^-(t)\bar{\psi}^+(t')\rangle = \frac{Tr\{c(t)c^\dagger(t')\rho_0\}}{Tr\{\rho_0\}}\\ &= -i(1-n_F)e^{-i\epsilon_0(t-t')}; && (1.24)\\ \mathcal{G}^{\tilde{T}}(t,t') &= -i\langle\psi^-(t)\bar{\psi}^-(t')\rangle = \frac{Tr\{\tilde{T}[c(t)c^\dagger(t')]\rho_0\}}{Tr\{\rho_0\}}\\ &= \theta(t'-t)\mathcal{G}^>(t,t') + \theta(t-t')\mathcal{G}^<(t,t') && (1.25) \end{aligned}$$

where $Tr\{\rho_0\} = 1+\rho(\epsilon_0)$ gives the trace of the equilibrium density matrix, referring to the empty and the singly occupied state and n_F is the fermionic occupation number. Again, the symbols T and $\tilde{T}$ mean the time-ordering and the anti-time-ordering, respectively.

Since the Grassman fields $\bar{\psi}$ are not conjugated to ψ, following Larkin and

Ovchinnikov [15], the Keldysh rotation in the fermonic case is different from the bosonic one (Eq.1.11)

$$\phi_1(t) = \tfrac{1}{\sqrt{2}}(\psi^+(t) + \psi^-(t)); \qquad \chi_2(t) = \tfrac{1}{\sqrt{2}}(\psi^+(t) - \psi^-(t)), \tag{1.26}$$

$$\bar{\phi}_1(t) = \tfrac{1}{\sqrt{2}}(\bar{\psi}^+(t) - \bar{\psi}^-(t)); \qquad \bar{\chi}_2(t) = \tfrac{1}{\sqrt{2}}(\bar{\psi}^+(t) + \bar{\psi}^-(t)). \tag{1.27}$$

Thus, we can write the algebraic manipulation on the Green's functions as

$$\begin{aligned} -i\langle\psi_\alpha(t)\bar{\psi}_\beta(t')\rangle &= \begin{pmatrix} \theta(t-t')(\mathcal{G}^> - \mathcal{G}^<) & \mathcal{G}^> + \mathcal{G}^< \\ 0 & \theta(t'-t)(\mathcal{G}^< - \mathcal{G}^>) \end{pmatrix} \\ &\equiv \begin{pmatrix} \mathcal{G}^R & \mathcal{G}^K \\ 0 & \mathcal{G}^A \end{pmatrix} \\ &= \begin{pmatrix} -i\theta(t-t')e^{-i\epsilon_0(t-t')} & -i(1-2n_F)e^{-i\epsilon_0(t-t')} \\ 0 & i\theta(t'-t)e^{-i\epsilon_0(t-t')} \end{pmatrix} \end{aligned} \tag{1.28}$$

where $\alpha, \beta = (1, 2)$ and hereby, similarly as the Eq. 1.10 and Eq. 1.13, we can get

$$\mathcal{G}^{-1} = \begin{pmatrix} (\mathcal{G}^R)^{-1} & (\mathcal{G}^{-1})^K \\ 0 & (\mathcal{G}^A)^{-1} \end{pmatrix} = \begin{pmatrix} \epsilon - \epsilon_0 + i\eta & (1-2n_F)i\eta \\ 0 & \epsilon - \epsilon_0 - i\eta \end{pmatrix}. \tag{1.29}$$

1.2 Surface Plasmon Polaritons (SPPs)

As we learn, a plasmon is an elementary excitation consisting of collective free electron oscillations in solids and polaritons are named as the coupled states between the elementary excitations and the photons. Literally, the surface plasmon describes the phenomenon of the collective oscillation of the electrons on the surface of the metal while the plasmon- polariton characterises the coupled state between a plasmon and a photon. Thus, the surface plasmon polarities (SPPs) make a bridge to study the interaction between electrons and photons.

The surface plasmon polaritons (SPPs) can be seen as the excitation of a coupled state between a photon and a plasmon at the interface between a metal and a dielectric, in which we can use the Maxwell equations for interface/dielectric to solve and understand [16, 17]. As shown in the Fig. 1.2, combined with the

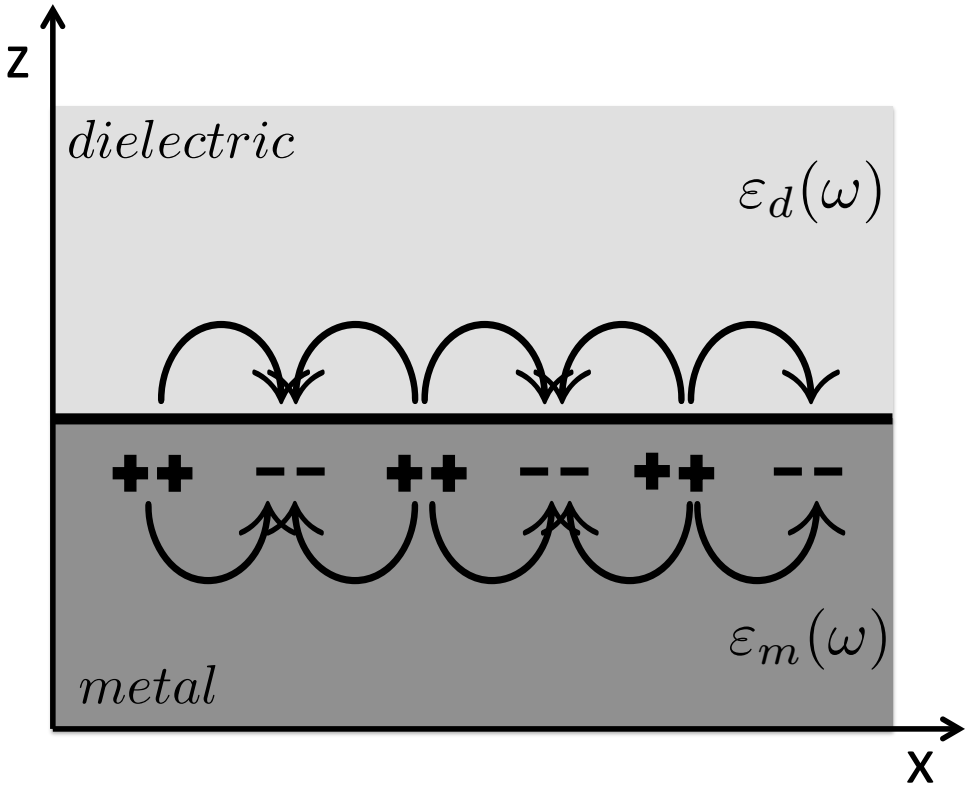

FIGURE 1.2: Sketch of the metal/dielectric interface with $\varepsilon_{m,d}$ the corresponding permittivity of the metal and dielectric.

Maxwell theory, we can get the dispersion relation of SPPs as

$$\omega = \sqrt{\frac{\varepsilon_m + \varepsilon_d}{\varepsilon_m \varepsilon_d}} c k_x \tag{1.30}$$

with the speed of light c and the wave vector k_x along the interface.

Fig. 1.3 depicts the dispersion relation, from which we can see that at low k, the SPP acts like a photon, but with the increase of k, the SPPs dispersion relation bends over and reaches an asymptotic limit called the "surface plasma frequency" $\omega_{sp} = \omega_p/\sqrt{1+\varepsilon_d}$, where $\omega_p = \sqrt{ne^2/m_0\varepsilon_0}$ is the quanta of volumn plasmons with energy $\hbar\omega_p \sim 10eV$. As is seen from the Fig. 1.3, there is $\omega_{sp} < \omega_p$, and in the free electron model of an electron gas, according to the metallic dielectric function

$$\varepsilon_m = 1 - \frac{\omega_p^2}{\omega^2}, \tag{1.31}$$

we can get that $\varepsilon_m < 0$, which means that surface plasmons are non-propagating collective oscillations of electron plasma near the surface.

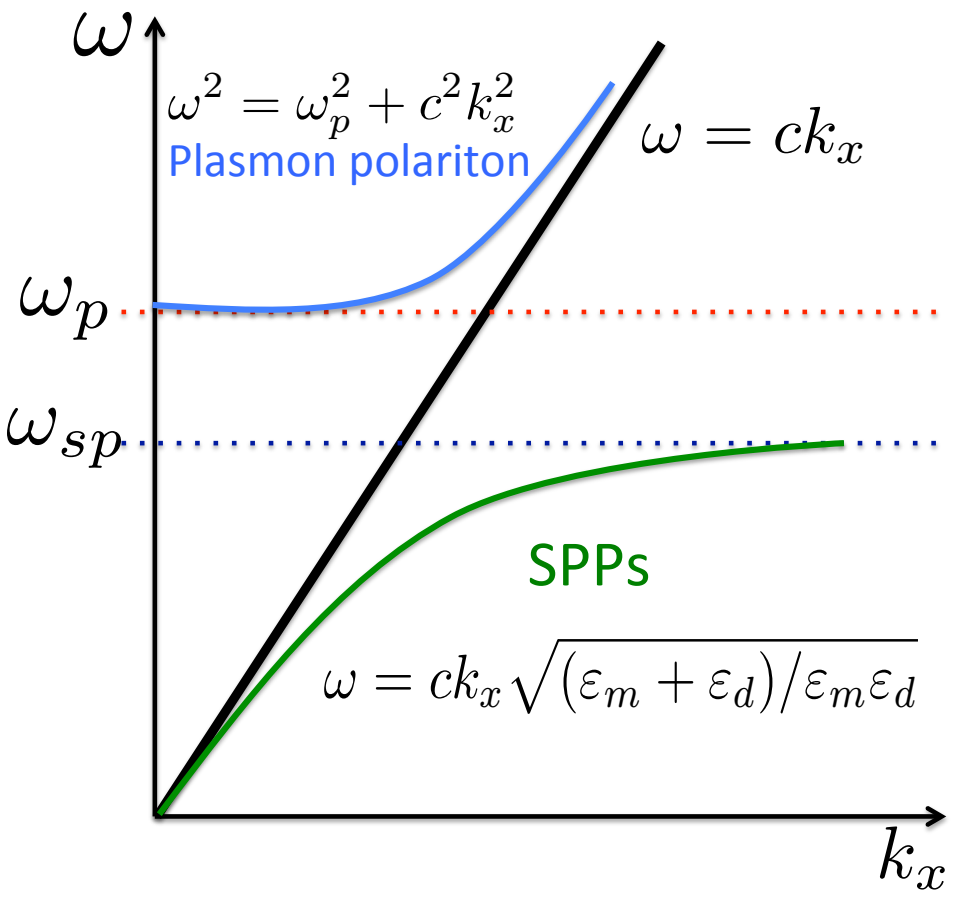

FIGURE 1.3: Sketch of the dispersion relation of SPPs. The SPPs have a shorter wavelength than the photon in the air (the black line), such that the out-of-plane component of the SPPs wave vector is purely imaginary and exhibits evanescent decay.

Hence, from the SPPs behaviour, we learn that such a wave can not radiate into air and is therefore trapped at the metal surface. So now, we can conclude that the surface plasmon polariton is a wave of surface charge propagating over the metal surface coupled with its electromagnetic field in the neighbouring dielectric medium [18–21], giving rise to its own unique properties. This coupling interaction results in the increase of the electric field at the surface, and perpendicularly , the exponential decay with distance from the surface. The perpendicular field is said to be evanescent or near field in nature due to its decay.

Besides, back to the Drude free electron model with $\varepsilon(\omega) = 1 - \frac{\omega_p^2}{\omega^2 + i\gamma\omega}$, we can review the plasmon resonance position in vacuum through three simple examples: Bulk metal, Metal surface and Metal sphere, whose permittivities are $\varepsilon = 0, -1, -2$, respectively. Thereby, we obtain the plasmon resonance position is

$\omega_p, \omega_p/\sqrt{2}, \omega_p/\sqrt{3}$ separately [17, 21, 22], which also points out that the electromagnetic waves can propagate along the metallic surface with a broad spectrum of eigenfrequencies $\omega \in [0, \omega_p/\sqrt{2}]$.

1.3 Electromagnetic Environment — the quantum harmonic LC oscillator

Specifically, elements like reservoirs and scattering regimes play an important part for the properties of nano-structures, however they do not give a full description of the real experiments. The systems we study are usually connected through an involved set of wiring and filters to the measurement and current/-voltage sources, rather than an ideal source. Clearly both inherent and external electromagnetic environments will change the transport properties of the nano-structure, for instance, causing the decoherence in the system [23–26].

Most studies concentrate on the time-averaged properties. Time-dependent fluctuations of the electrical current are also affected by the environment, which reduces the low-frequency fluctuations by a feedback loop: A current fluctuation δI induces a counter-acting voltage fluctuation $\delta V = -Z\delta I$ over the conductor, which in turn reduces the current by an amount of $-G\delta V$ (Here Z and G are the equivalent series impedance of the macroscopic voltage-biased circuit and the conductance of the mesoscopic system, respectively.).

One straightforward way to describe the electrical circuit from the classical to the quantum level is to use the framework of Hamiltonian description. The classical variables are replaced by the corresponding operators. For the simplest case, we can consider the well-known harmonic LC oscillator (Fig. 1.4) with the Hamiltonian's expression

$$H = \frac{Q^2}{2C} + \frac{\varphi^2}{2L}, \tag{1.32}$$

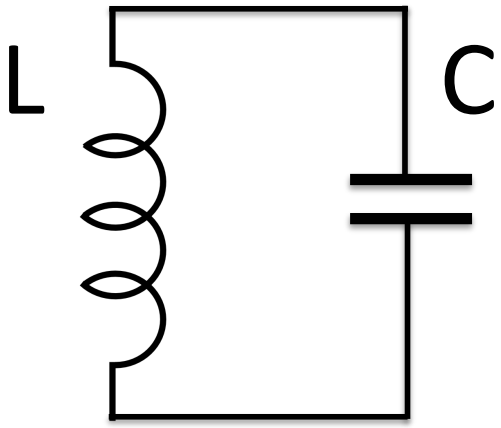

FIGURE 1.4: Sketch of LC oscillator with L and C denoting the inductance and capacitance respectively.

where the time derivative of φ describes the voltage across the inductor and Q is the corresponding charge on the capacitor.

Using the common annihilation and creation operators for bosons, which obey the commutation rule

$$[a, a^\dagger] = 1, \tag{1.33}$$

we can derive the relation

$$\varphi = \sqrt{\frac{\hbar Z_0}{2}}(a + a^\dagger), \tag{1.34}$$

$$Q = \frac{1}{i}\sqrt{\frac{\hbar}{2Z_0}}(a - a^\dagger), \tag{1.35}$$

which just gives us the general Hamiltonian form of a harmonic oscillator $H = \hbar\omega_0(a^\dagger a + \frac{1}{2})$, where

$$\omega_0 = \sqrt{\frac{1}{LC}}, \tag{1.36}$$

$$Z_0 = \sqrt{\frac{L}{C}}. \tag{1.37}$$

We then calculate the flux-flux correlation function through the above relation at the thermal equilibrium

$$\begin{aligned}\langle\varphi(t)\varphi(0)\rangle &= \frac{\hbar Z_0}{2}(\langle a^\dagger a\rangle e^{i\omega_0 t} + \langle aa^\dagger\rangle e^{-i\omega_0 t}) \\ &= \frac{\hbar Z_0}{2}[\coth(\frac{\beta\hbar\omega_0}{2})\cos(\omega_0 t) - i\sin(\omega_0 t)]. \end{aligned} \tag{1.38}$$

with $\beta = 1/k_B T$. It does reveal the zero-point fluctuation $\langle\varphi^2\rangle = \frac{\hbar Z_0}{2}$ by setting $t = 0$ and meanwhile predict that the quantum correlation function is not real, which means it can not be measured directly.

Considering the generalized impedance function of an LC oscillator [27]

$$Z(\omega) = Z_0\{\frac{\pi}{2}\omega_0[\delta(\omega-\omega_0)+\delta(\omega+\omega_0)] + \frac{i}{2}[\mathcal{P}(\frac{\omega_0}{\omega-\omega_0}) + \mathcal{P}(\frac{\omega_0}{\omega+\omega_0})]\}, \tag{1.39}$$

we can rewrite Eq. 1.38 of the flux-flux correlation function with $Z(\omega)$:

$$\begin{aligned}\langle\varphi(t)\varphi(0)\rangle &= \frac{\hbar}{\pi}\int_{-\infty}^{\infty}\frac{d\omega}{\omega}Re[Z(\omega)]\frac{e^{-i\omega t}}{1-e^{-\beta\hbar\omega}} \\ &= \frac{\hbar}{2\pi}\int_{-\infty}^{\infty}\frac{d\omega}{\omega}[\coth(\frac{\beta\hbar\omega}{2})+1]Re[Z(\omega)]e^{-i\omega t}. \end{aligned} \tag{1.40}$$

Thus, the Fourier transform of the correlation function, noted as spectral density $A(\omega)$, has the form as

$$\begin{aligned}A(\omega) &= \int_{-\infty}^{\infty} dt\langle\varphi(t)\varphi(0)\rangle e^{i\omega t} \\ &= \frac{\hbar}{\omega}[\coth(\frac{\beta\hbar\omega}{2})+1]Re[Z(\omega)] \neq A(-\omega), \end{aligned} \tag{1.41}$$

which is also called the quantum fluctuation dissipation theorem [28] and shows the difference from a classical spectral density of fluctuaions.

In the later section, we'll see that it is directly related to the emission and absorption processes, referring to the phase-phase correlation function $J(t)$ [29]

$$J(t) = \frac{2e^2}{h}\int_0^{\infty}\frac{d\omega}{\omega}Re[Z(\omega)]\{\coth(\frac{1}{2}\beta\hbar\omega)[\cos(\omega t)-1] - i\sin(\omega t)\}. \tag{1.42}$$

And at zero temperature, it shows the obvious relation with the environment impedance $Z(\omega)$

$$J(t) \sim \int \frac{d\omega}{\omega} Re[Z(\omega)](e^{-i\omega t} - 1). \tag{1.43}$$

1.4 Quantum current noise

Principally, in a quantum system, due to its quantum discrete nature, the current has to be replaced by current operators $I(t)$ in the Heisenberg picture and the current-current correlator reads:

$$C(t) = \langle I(t')I(t'+t)\rangle \equiv \sum_i P_i \langle i|I(0)I(t)|i\rangle, \tag{1.44}$$

and the corresponding noise spectrum of the quantum system is:

$$S(\omega) \;=\; \int_{-\infty}^{\infty} dt e^{i\omega t} \langle I(0)I(t)\rangle \,. \tag{1.45}$$

Here, $|i\rangle$ is the eigenstate of the system's Hamiltonian H and P_i is the probability of the system initially at the state $|i\rangle$ with energy E_i. Since in a quantum case, the operators $I(t)$ for different times do not commute any more $[I(t), I(t')] \neq 0$. Therefore,

$$\begin{aligned} C(-t) = \langle I(t')I(t'-t)\rangle \neq \quad & \langle I(t'-t)I(t')\rangle \\ \overset{t'-t=t"}{\Longleftrightarrow} \quad & \langle I(t")I(t"+t)\rangle = C(t), \end{aligned} \tag{1.46}$$

$$\longrightarrow S(\omega) \neq S(-\omega). \tag{1.47}$$

To see this explicitly, one could insert the identity operator $\sum_f |f\rangle\langle f|$ in Eq. 1.45 [30] and get the current noise expressed in terms of transitions between the many-body states $|i\rangle$ and $|f\rangle$ [31]

$$S(\omega) = 2\pi\hbar \sum_{i,f} P_i \left|\langle i|I|f\rangle\right|^2 \delta(E_i - E_f - \hbar\omega). \tag{1.48}$$

which confirms that the noise spectrum $S(\omega)$ is real, but nonsymmetric.

1.4.1 Transition probability

In order to understand the current noise $S(\omega)$ (Eq. 1.48) physically, we can consider the whole system has the total Hamiltonian $H_{tot} = H + H_{ext} + \alpha I(t)q$, where q is an operator of the external system, maybe the current operator through the inductor in the LC circuit for instance [32, 33] and α describes the small coupling between H and H_{ext}. By using the Fermi golden rule, the probability of the total system from the initial state $|i\rangle \otimes |\phi\rangle$ transiting into the final state $|f\rangle \otimes |\phi'\rangle$ involving the energy transfer $\hbar\omega > 0$, is given by

$$\Gamma^{emiss}_{i,\phi\to f,\phi'}(\omega > 0) = \frac{2\pi}{\hbar}\alpha^2 |\langle i|I|f\rangle|^2 |\langle \phi|q|\phi'\rangle|^2 \delta(E_i - E_f - \hbar\omega), \quad E_{\phi'} - E_\phi = \hbar\omega \tag{1.49}$$

and then summing over all the initial and final states, we get the total rate

$$\Gamma^{emiss}_{tot}(\omega) = \frac{2\pi}{\hbar}\alpha^2 \sum_{i,f} \sum_{\substack{\phi,\phi' \\ E_{\phi'} - E_\phi = \hbar\omega}} P_i P_\phi |\langle i|I|f\rangle|^2 |\langle \phi|q|\phi'\rangle|^2 \delta(E_i - E_f - \hbar\omega). \tag{1.50}$$

Comparing Eq. 1.50 with the noise spectrum $S(\omega)$ (Eq. 1.48), the total transition rate can be rewritten as

$$\Gamma^{emiss}_{tot}(\omega) = \alpha^2 S(\omega) \times S^{abs}_{ext}(\omega) \tag{1.51}$$

with $S^{abs}_{ext}(\omega)$ including all the other factors that belong to the external system.

Similarly, the total probability rate for a transition into a state, in which the energy of the external system is lower by $\hbar\omega$ is

$$\Gamma^{abs}_{tot}(\omega) = \alpha^2 S(-\omega) \times S^{emiss}_{ext}(\omega). \tag{1.52}$$

Now we can see here that $S(\omega)$ and $S(-\omega)$ for $\omega > 0$ are the corresponding emission and absorption spectra due to the coupling with the current. It just indicates in quantum picture, the current fluctuations should be treated as the emission or absorption ability.

1.4.2 Non-interacting systems

In the case where the interaction between the charge carrieres can be neglected, the states become the single-particle states $\phi_n(x)$ with the corresponding single-particle energies ϵ_n. By using the second quantization form, the field operators are

$$\psi(x) = \sum_n c_n \phi_n(x), \quad \psi^\dagger(x) = \sum_n c_n^\dagger \phi_n^*(x), \tag{1.53}$$

where c_n and $c_n^\dagger$ are the annihilation and creation operators, obeying the fermonic anti-commutation relations $\{c_n, c_{n'}^\dagger\} = \delta_{nn'}$.

From Eq. 1.48, one can obtain

$$S(\omega) = 2\pi\hbar \sum_{n,n'} |I_{nn'}|^2 n(\epsilon_n)[1 - n(\epsilon_{n\prime})]\delta(\epsilon_n - \epsilon_{n'} - \hbar\omega) \tag{1.54}$$

where

$$I_{nn'} = \frac{1}{L}\int_L \frac{-ie\hbar}{2m}[\phi_n^*(x)\nabla_x\phi_{n'}(x) - \nabla_x\phi_n^*(x)\phi_{n'}(x)]dx \tag{1.55}$$

is the matrix element for the single-particle current operator I with L the size of the area in which current in the system interacts with the measurement and $n(\epsilon_n) = \sum_i P_i\langle i|c_n^\dagger c_n|i\rangle$ denoting the occupation at the energy ϵ_n.

We can see that $S(\omega)$ is a sum over all possible single-particle transitions between the states with the occupancy permission $n(\epsilon_n)[1 - n(\epsilon_{n\prime})] \neq 0$ and the energy differences satisfying $\epsilon_{n'} = \epsilon_n - \hbar\omega$, transferring $\hbar\omega$ to the external system. For $\omega > 0$, it gives the "go-down" transitions to the energy lower by $\hbar\omega$ than the original state while $S(-\omega)$ means the transitions by absorbing the energy from the external system. Eq. 1.54 shows that for the calculations of the noise, we need to pick out all possible transitions and evaluate the matrix elements $I_{nn'}$ for the relevant transitions.

Simply speaking, the more possible transitions just denotes the more noise. Basically, higher temperatures and voltages which both imply the more particles above the fermi sea can cause more noise.

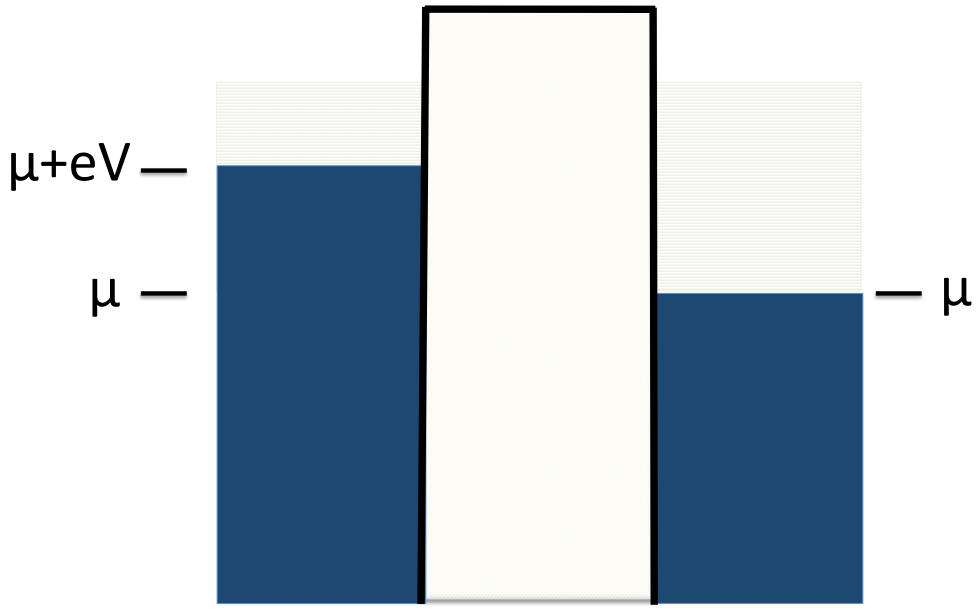

FIGURE 1.5: Occupation at zero temperature of one dimensional Landauer conductor with a single potential barrier.

1.4.2.1 One dimensional Landauer-type ballistic conductor at zero temperature

To learn more about the noise spectrum $S(\omega)$, let's consider a the conductor connected to two ballistic leads with the applied bias voltage V (Fig. 1.5) [34], assume that $eV, \hbar\omega \ll \mu$ and neglect the interaction and spin. The single-particle energy can then be taken as $\epsilon = \hbar^2 k^2/2m$ and the calculations can follow the scattering theory.

At zero temperature, the occupation number $n(\epsilon_n)$ becomes the unit step function, being 1 or 0 that depends on the energy ϵ_n above the chemical potential $\mu + eV, \mu$ or below them. According to the factor $n(\epsilon_n)[1 - n(\epsilon_{n'})]$(Eq. 1.54), the only possible transition will be the particle with energy $\mu < \epsilon_n < \mu + eV$ goes from one occupied left state into one empty right state with energy lower by $\hbar\omega$.

Thus, with the matrix element of the current operator

$$|I_{n\in\text{left},n'\in\text{left}}|^2 = (\frac{e\hbar k_F}{mV_0})^2\mathcal{T}^2 \tag{1.56}$$

$$|I_{n\in\text{left},n'\in\text{right}}|^2 = (\frac{e\hbar k_F}{mV_0})^2\mathcal{T}(1-\mathcal{T}) \tag{1.57}$$

$$|I_{n\in\text{right},n'\in\text{left}}|^2 = (\frac{e\hbar k_F}{mV_0})^2\mathcal{T}(1-\mathcal{T}) \tag{1.58}$$

$$|I_{n\in\text{right},n'\in\text{right}}|^2 = (\frac{e\hbar k_F}{mV_0})^2\mathcal{T}^2 \tag{1.59}$$

and replacing $\sum_k \to V_0(2\pi)^{-1}\int dk$, the emission spectrum can be derived as

$$\begin{aligned} S(\omega) &= 2\pi\hbar \sum_{\substack{n\in\text{left}\\ n'\in\text{right}}} |I_{nn'}|^2\delta(\epsilon_n - \epsilon_{n'} - \hbar\omega) \\ &= \frac{e^2}{2\pi\hbar}\mathcal{T}(1-\mathcal{T})[eV - \min(eV,\hbar\omega)] \qquad (\omega > 0) \end{aligned} \tag{1.60}$$

with $\mathcal{T}$ is the transmission coefficient between the left and right sides. From this we learn that the lowest transition is $\mu+\hbar\omega \to \mu$ while the highest occupied energy for the left side is $\mu + eV$, so if $\hbar\omega > eV$, there are no possible down transitions. Thus, no noise can be emitted beyond the cutoff at eV (see Fig. 1.6).

1.4.2.2 One dimensional Landauer-type ballistic conductor at finite temperature

Furthermore, at finite temperature, the transitions have more possibilities and the occupation number now obeys the fermi distribution $\frac{1}{\exp\beta(\epsilon_n-\mu)+1}$. Following the similar calculations at zero temperature, we can gain

$$S(\omega) = \frac{e^2\mathcal{T}(1-\mathcal{T})}{2\pi\hbar}\Big(\frac{\hbar\omega - eV}{e^{\beta(\hbar\omega-eV)}-1} + \frac{\hbar\omega+eV}{e^{\beta(\hbar\omega+eV)}-1}\Big) + \frac{2e^2\mathcal{T}^2}{2\pi\hbar}\frac{\hbar\omega}{e^{\beta\hbar\omega}-1}. \tag{1.61}$$

Apparently, this is the general non-symmetrized power spectrum at finite frequency, temperature and bias voltage, giving $\omega > 0$ means the emission while $\omega < 0$ represents the absorption.

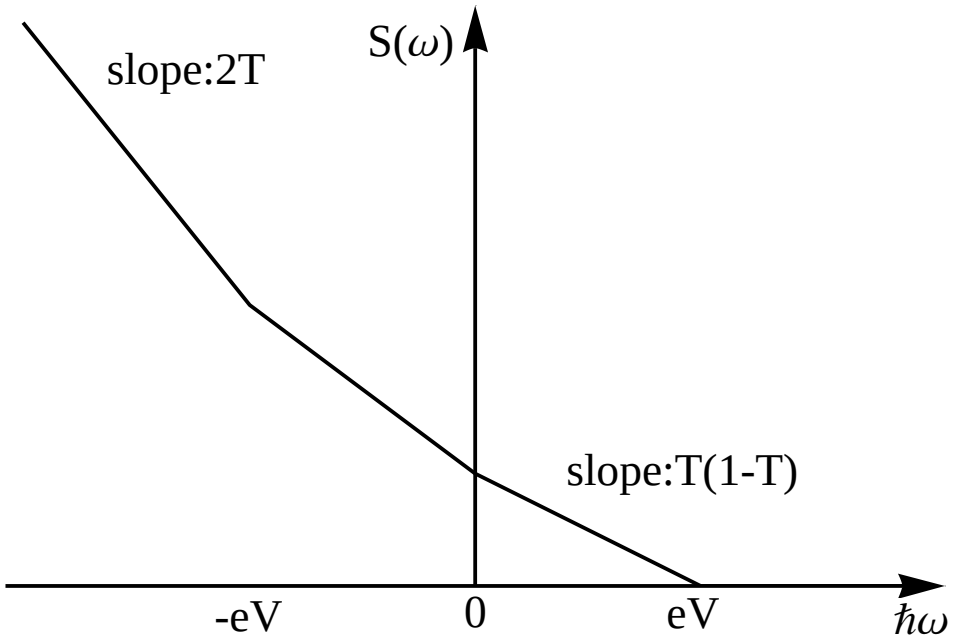

FIGURE 1.6: Sketch of Eq. 1.62. It shows the noise spectrum has a clear cutoff at the bias voltage eV at zero temperature.

From the Eq. 1.61, we can easily get the zero temperature result (Eq. 1.60)

$$\begin{aligned} S(\omega > 0) &= \frac{e^2}{2\pi\hbar}\mathcal{T}(1-\mathcal{T})[eV - \min(eV, \hbar\omega)], \\ S(\omega < 0) &= \frac{e^2}{2\pi\hbar}\mathcal{T}(1-\mathcal{T})[eV - \min(eV, \hbar|\omega|)] + \frac{e^2 2\mathcal{T}}{2\pi\hbar}\hbar|\omega|, \end{aligned} \tag{1.62}$$

and Fig. 1.6 shows the property of the noise spectrum $S(\omega)$ with the cutoff at eV for the emission and the infinite absorption.

At $eV = 0$, the equilibrium noise $S(\omega)$ from Eq. 1.61 satisfies

$$S(\omega) = \frac{e^2\mathcal{T}}{\pi}\frac{\omega}{e^{\beta\hbar\omega} - 1} = S(-\omega)e^{-\hbar\omega/k_BT} \quad eV = 0, \tag{1.63}$$

which just is the known detailed-balance relation.

And when $\hbar\omega \ll k_BT$, it becomes

$$S(\omega) = \frac{e^2\mathcal{T}}{\pi}\frac{1}{\beta\hbar} = 2\frac{e^2\mathcal{T}}{2\pi\hbar}k_BT \stackrel{!}{=} 2G_lk_BT \tag{1.64}$$

with $G_l = \frac{I}{V} = \mathcal{T}e^2/2\pi\hbar$ corresponding to the linear conductance. Eq. 1.64 just verifies the classical Nyquist theorem [35, 36].

1.5 Coulomb blockade in a tunnel junction

The term Coulomb blockade is used to describe phenomena which show a blockade of transport through a system due to electrostatic effects [29, 37, 38]. As is known, classically, there is no electrical transport through the barrier, i.e., the junction just acts like a capacitor characterized by a capacitance C. So, if connecting a single tunnel junction to an external circuit, it may be charged by $Q = CV$ and leave an additional charging energy $Q^2/2C$, where V is the voltage externally applied to the junction.

Considering the quantum effects of the single electron crossing the tunnel barrier, there is the charging energy $E_c = e^2/2C$ and the corresponding voltage $V_c = e/2C$. Therefore, the current through the junction is blocked with voltages below $V < V_c = e/2C$, which is just referred to as **Coulomb blockade**. Hereby, the $I - V$ curve is essentially $I = R^{-1}(V - V_c)\theta(V - V_c)$, giving a change at $V = V_c$, called the Coulomb gap, which can be smeared out by increasing temperature.

According to the description above, we can see that when the resistance R is not small, or much greater than the quantum of resistance $R \gg R_k = h/e^2$, the system can stay in the blockage regime. In another word, in this regime, the impedance can react quick enough to influence and prevent the dynamics of the transfer of a single electron [26, 29].

1.6 Tunneling rates for single tunnel junctions and P(E) theory

In previous sections, we've already learned separately about the tunneling junction and the electromagnetic environment, as well as the approach for further investigation. To establish a coupling between the tunneling electron and the electromagnetic environment, which also is our main system, we first consider the quasiparticle system in two normal metal leads which can be described by the

Hamiltonian

$$H_{sys} = \sum_{k_\alpha \sigma} \epsilon_{k_\alpha} c^\dagger_{k_\alpha \sigma} c_{k_\alpha \sigma} \tag{1.65}$$

with $\alpha = L, R$ denotes the left and right leads and σ describes the spin. ϵ_{k_α} is the energy of the quasiparticle with momentum k_L or k_R.

The tunneling Hamiltonian H_T is written as [26, 39, 40]

$$H_T = \sum_{k_L k_R \sigma} T_{k_L k_R} c^\dagger_{k_R \sigma} c_{k_L \sigma} e^{-i\varphi} + H.C., \tag{1.66}$$

with the phase φ describing the voltage fluctuation being defined as

$$\varphi(t) = \frac{e}{\hbar} \int_{-\infty}^{t} dt' U(t') \tag{1.67}$$

where $U = Q/C$ is the voltage across the junction.

With the commutation relation $[\varphi, Q] = ie$, the operator $e^{-i\varphi}$ corresponds to a momentum shift operator

$$e^{i\varphi} Q e^{-i\varphi} = Q - e \tag{1.68}$$

and acts as changing the charge on the junction by an elementary charge e.

It is evident that in the absence of the environment, the phase operator vanishes and the tunneling Hamiltonian H_T becomes to be the normal one in the common tunnel junction. Considering the H_T as a perturbation, under the Fermi golden rule, as in sec.1.3.1, the tunneling rates between the initial state $|i\rangle$ and the final state $|f\rangle$ is expressed as

$$\Gamma_{i \to f} = \frac{2\pi}{\hbar} |\langle f | H_T | i \rangle|^2 \delta(E_i - E_f) \tag{1.69}$$

By telling apart the quasiparticle and the reservoir both in the tunneling Hamiltonian H_T and the states $|i, f\rangle$, the rate expression Eq. 1.69 then turns into

$$\begin{aligned} \Gamma(V) = & \frac{1}{e^2 R_T} \int_{-\infty}^{\infty} dE dE' f(E)(1 - f(E')) \\ & \times \sum_{R, R'} |\langle R' | e^{-i\varphi} | R \rangle|^2 P_\beta(R) \delta(E + eV + E_R - E' - E_{R'}) \end{aligned} \tag{1.70}$$

with R_T as the tunneling resistance containing all constant terms.

After tracing out all the environmental states, we can get the general form

$$\Gamma(V) = \frac{1}{e^2 R_T}\int_{-\infty}^{\infty} dE dE' f(E)(1-f(E')) \times \int_{-\infty}^{\infty} \frac{dt}{2\pi\hbar} \exp(\frac{i}{\hbar}(E-E'+eV)t)\langle e^{i\varphi(t)}e^{-i\varphi(0)}\rangle. \tag{1.71}$$

Now, all problems are focused on the evaluation of the correlation function $\langle e^{i\varphi(t)}e^{-i\varphi(0)}\rangle$. When thinking the electromagnetic environment viewed as a LC-circuit, the related Hamiltonian is harmonic with quadratic form of φ. Through the Wick theorem [41], the correlation function is converted to

$$\langle e^{i\varphi(t)}e^{-i\varphi(0)}\rangle = e^{\langle[\varphi(t)-\varphi(0)]\varphi(0)\rangle} \equiv e^{J(t)}, \tag{1.72}$$

in which the phase-phase correlation function $J(t)$ is defined as $J(t) = \langle[\varphi(t) - \varphi(0)]\varphi(0)\rangle$.

Replacing Eq. 1.72 back to Eq. 1.71, with the introduction of $P(E)$ from the Fourier transform of the correlation function $\langle e^{i\varphi(t)}e^{-i\varphi(0)}\rangle$ [24]

$$P(E) = \frac{1}{2\pi\hbar}\int_{-\infty}^{\infty} dt \exp[J(t) + \frac{i}{\hbar}Et], \tag{1.73}$$

thus, the tunneling rates Eq. 1.71 converts into

$$\begin{aligned}\Gamma(V) &= \frac{1}{e^2 R_T}\int_{-\infty}^{\infty} dE dE'[f(E)(1-f(E'))]P(E-E'+eV) \\ &\Rightarrow \frac{1}{e^2 R_T}\int_{-\infty}^{\infty} dE dE'[f(E)(1-f(E'+eV))]P(E-E') \\ &\Rightarrow \frac{1}{e^2 R_T}\int_{-\infty}^{\infty} dE \frac{E}{1-\exp(-\beta E)}P(eV-E),\end{aligned} \tag{1.74}$$

where the last step is derived from making use of the integral over Fermi function

$$\int_{-\infty}^{\infty} dE[f(E)(1-f(E+x))] = \frac{x}{1-e^{-\beta x}}. \tag{1.75}$$

From the Eq. 1.74, the physical meaning of $P(E)$ becomes clear, which can be explained as the probability of the energy exchange between the tunneling electron

and the electromagnetic environment.

According to the definition of $P(E)$ (Eq. 1.73), one can quickly notice that

$$\int_{-\infty}^{+\infty} P(E)dE = e^{J(0)} \equiv 1, \tag{1.76}$$

$$P(-E) = e^{-\beta E}P(E), \tag{1.77}$$

in which the first equation confirms again that $P(E)$ represents the probability while the second equation is just the so-called detailed balance symmetry, from which one can conclude that at zero temperature $\beta \to \infty$, for negative energies, $P(E) \to 0$, meaning no energy can be absorbed from the environment but only energies emitted into the environment. In one word, at zero temperature $T = 0$, the energy exchange is unidirectional.

1.7 Overview of over-bias Light emission from tunnel junctions in STM-Experiment

Light, as we've learned, is a natural way to transfer energy through space, and it can be generated by matter in an excited state, which can come from a variety of sources. The light emission has been studied with scanning tunneling microscope (STM) for many years [21, 42–56] despite using different materials and different mechanism involved. Among all those researches, the investigations of photon emission from the interaction of tunneling electrons with SPPs mode have become more and more interesting since it offers us to probe the electrons interactions more directly and does reveal many attractive phenomena, waiting for explanations.

Based on the above sections, we've already known that in a simple picture, the emitted light spectrum is limited by the bias voltage, $\hbar\omega < eV$, which is resulted from the Pauli principle, prohibiting inelastic tunneling with higher energy exchange (see Fig. 1.5).

In order to get more information and differences, in the experiment [54], they perform the study with a ultrahigh vacuum STM at low temperature. As for

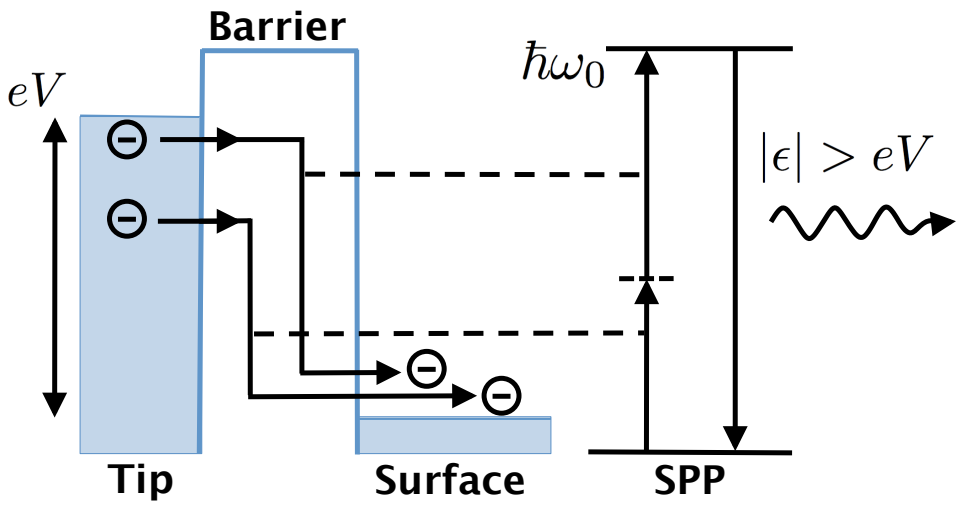

FIGURE 1.7: The electron tunneling process in energy space shows how two electrons excite a SPP via a virtual state.

enhancing the plasmon excitations, they take the Au-coated W tips with flat Au(111) surfaces. Then, sure enough, they obtain the different and special light spectrum Fig.1(a) in the paper (Ref.[54]).

Clearly, there appear an extra peak which breaks the one-electron threshold $< eV = 1.3$ eV and enters the two-electron region $h\nu \approx 1.75$ eV. Although this "additional" peak is small comparing with the normal one-electron peak nearby under the detector response, it is still in existence and must carry some useful information about the electron-electron interactions.

To evaluate this new over-bias peak and figure out its inside mechanism, they compare the two peaks Fig.2(a) in the experiment. From the comparison, it evidently show that the "two-electron" peak also exhibits the same electromagnetic mechanism with the known one-electron peak. This can be speculated as two electrons tunnel and each of them contributes to excite a SPP together up to an over-bias region. Then the SPP decays due to its own property, leading to an over-bias emitted photon showing up, shown in Fig. 1.7 [57–59]. And this proposal is also verified by the power laws $\approx I^{\beta}$, where for 2e light, $\beta \approx 1.7 \pm 8\%$ (see Fig.2(c) in [54]).

Furthermore, they continue to look into this over-bias photon emission from the tunnel junction, such as going beyond the tunneling limit to study the Fano

factor [55] and checking the nonequilibrium distribution of electrons [60].

Similarly, there are also some other findings reported in photon emission with energy above the threshold from molecular films and Josephson junctions [61–71], in which the source of the over-bias light emission can be various, e.g. plasmon-mediated, hot-electron injection, some special transitions and so on.

1.8 This Thesis

In this thesis, motivated by the interesting observations from the recent experiments [54, 55], we develop a theoretical framework and establish a suitable model circuit to study the enhanced light emission through a tunnel junction within the presence of the surface plasmon-polariton (SPP) by mimicking it as the damped LC-oscillator. Our theoretical calculations verify that the non-Gaussian current fluctuations contribute to the observed overbias light emission and give the rather good agreement with the experiment results.

In Chapter. 2, we introduce the path integral method that we mainly use to derive and calculate the transition rate in the detector, thus studying the interactions between the tunneling electrons and the electromagnetic environment. The non-Gaussian part of the action from the tunneling conductor although makes problems complex, we sort out the dominant formulations under the reasonable approximations to treat and fix things step by step, and arrange a proper systematic structure to do further research.

The next Chapter describes the main work of our research. By means of an experimental setup, the detection of the photons emitted through the tunnel junction can be set as the signal of electron-electron interaction. Based on the standard $P(E)$ theory which confirms that the Gaussian fluctuations do not generate overbias light emission, we go beyond the Gaussian range, expand into the high order cumulants, analyse the unusual light emission and make comparisons with the experiments. It turns out that what we've done really explains and reproduces well the experimental observations. We additionally look into the temperature effect on the tunneling processes and the expansion to the six-order contributing the three-electron tunneling processes.

Last, we make a summary of our total work. We find that our work shows a good agreement with the experimental measurement and offers a theoretical way to well explain the electron-electron interactions happening during the electron tunneling, which can be applied to more systems in the future.

Chapter 2

Formulas of the tunnel junction coupled to the electromagnetic environment

What we consider in this whole work is the light emission due to the electrons tunneling from a scanning tunnelling microscope (STM) to a metallic surface, which has been focused and studied for many years both experimentally and theoretically. In the experiments, the emitted photons can be detected and measured by a photon detector, thus providing the useful and interesting information that happens during the tunneling processes and also bringing about the investigation into the variant electron-electron interactions. In this Chapter, we sort out the main method and steps we'll use in the specific system in the next chapter.

2.1 Transition rate

In this thesis, we set the detector as a simple two-level system, in which the two localised charge states separated by ϵ are connected by a transition amplitude $\mathcal{T}$ (see Fig. 2.1). And considering the weak coupling α between the detector and the STM junction and the voltage fluctuation due to the electromagnetic environment described by phase operator $\varphi(t) = \frac{e}{\hbar}\int_{-\infty}^{t} V(t')dt'$ [23, 24], the amplitude

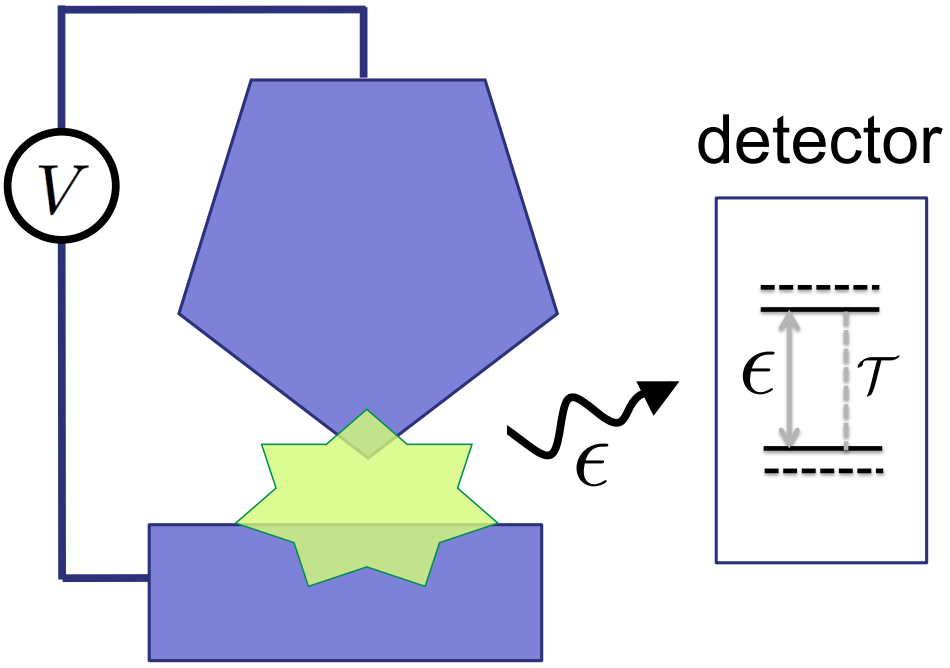

FIGURE 2.1: The sketch of the light emission through the STM with energy ϵ absorbed by the detector, which can be modelled by a simple two-level system. $\mathcal{T}$ gives the transition amplitude between the two states. The yellow part depicts the possible interactions, which are surface plasmon polariton (SPP) in this thesis.

$\mathcal{T}$ becomes $\mathcal{T}e^{i\alpha\varphi}$. Thus, according to the fermi golden rule, the transition rate between the two states can be written down as [24, 31]:

$$\Gamma(\epsilon) = \frac{2\pi}{\hbar}|\mathcal{T}|^2 \sum_{R,R'} P(R)|\langle R'|e^{-i\alpha\varphi}|R\rangle|^2 \delta(\epsilon + E_R - E_{R'}), \tag{2.1}$$

where $|R\rangle$ and $|R'\rangle$ are the reservoir states with energies E_R and $E_{R'}$ and $P(R) = \langle R|\rho|R\rangle$ gives the probability of finding the initial reservoir state $|R\rangle$ with the density ρ.

To go ahead, it is helpful to rewrite the delta function above as

$$\delta(\epsilon + E_R - E_{R'}) = \frac{1}{2\pi\hbar}\int dt \exp(\frac{i}{\hbar}t(\epsilon + E_R - E_{R'})), \tag{2.2}$$

and in the Heisenberg picture, we have

$$e^{\frac{i}{\hbar}(E_R - E_{R'})t}\langle R|e^{i\alpha\varphi}|R'\rangle = \langle R|e^{i\alpha\varphi(t)}|R'\rangle. \tag{2.3}$$

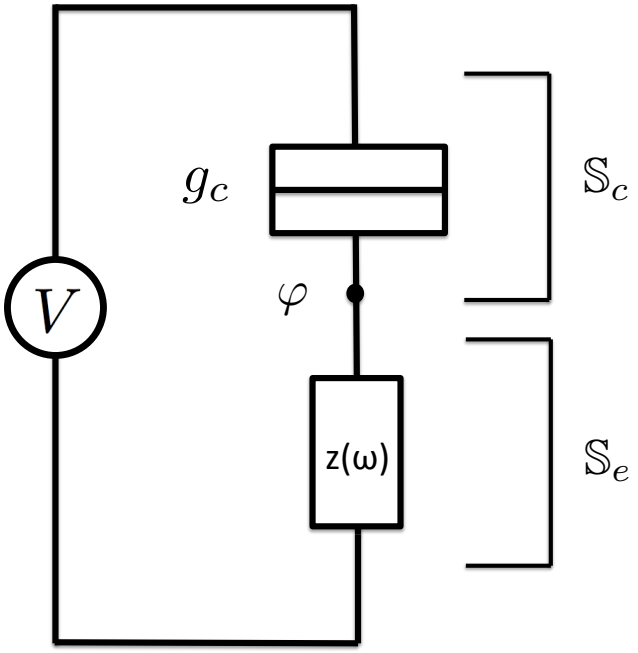

FIGURE 2.2: The STM junction can be described by the tunnel conductor with the tunneling conductance g_c and the corresponding action $\mathbb{S}_c$ while the surface plasmon polariton (SPP) is depicted as the environment impedance $z(\omega)$ with the action $\mathbb{S}_e$.

Together with the definition of $P(R)$, we find out the form of the tunneling rate [24, 26, 72]:

$$\begin{aligned}\Gamma(\epsilon) &= \frac{1}{\hbar^2}|\mathcal{T}|^2 \int dt e^{\frac{i}{\hbar}\epsilon t} \sum_{R,R'} P(R)\langle R|e^{i\alpha\varphi(t)}|R'\rangle\langle R'|e^{-i\alpha\varphi(0)}|R\rangle \\ &= \frac{1}{\hbar^2}|\mathcal{T}|^2 \int dt e^{\frac{i}{\hbar}\epsilon t}\langle e^{i\alpha\varphi(t)}e^{-i\alpha\varphi(0)}\rangle. \end{aligned} \tag{2.4}$$

2.2 Calculations of transition rate

From the above equation, by setting $\hbar = 1$, the detection rate at energy ϵ due to the fluctuations of $\alpha\varphi(t)$ is expressed as [57, 58]

$$\Gamma(\epsilon) = |\mathcal{T}|^2 \int dt \langle e^{i\alpha\varphi(t)}e^{-i\alpha\varphi(0)}\rangle e^{i\epsilon t}. \tag{2.5}$$

We employ the path integral method described in Chapter 1.1 to evaluate the correlator $\langle e^{i\alpha\varphi(t)}e^{-i\alpha\varphi(0)}\rangle$. As the STM system can be described in Fig. 2.2,

together with the Keldysh actions of the tunnel conductor, $\mathbb{S}_c$, and the linear electromagnetic environment, $\mathbb{S}_e$, the correlator can then be represented as

$$\langle e^{i\alpha\varphi(t)}e^{-i\alpha\varphi(0)}\rangle = \int \mathcal{D}[\Phi]\exp\{-i\mathbb{S}_e[\Phi] - i\mathbb{S}_c[\Phi] + i\alpha[-\varphi^+(0) + \varphi^-(t)]\}, \quad (2.6)$$

where the two-component $\Phi = ((\varphi^+ + \varphi^-)/2, \varphi^+ - \varphi^-)^T$ with the real fields $\varphi^{\pm}(t)$ are defined on the forward and backward Keldysh contours (Fig. 1.1) respectively.

2.2.1 Actions

The action of the electromagnetic environment, which can be treated as a set of harmonic oscillators, is quadratic in the fields [13, 73] (Eq. 1.13) and characterised by its impedance $z_\omega = \frac{-i\omega}{\omega-\omega_0+i\eta}/R_Q$,

$$\mathbb{S}_e = \int d\omega \Phi^T_{-\omega} A_\omega \Phi_\omega, \quad (2.7)$$

with

$$A_\omega = -\frac{i}{2}\begin{pmatrix} 0 & -\frac{\omega}{z_{-\omega}} \\ \frac{\omega}{z_\omega} & W(\omega)\Re\{\frac{1}{z_\omega}\} \end{pmatrix} \quad (2.8)$$

where $W(\omega) = \omega\coth(\frac{1}{2}\beta\omega)$ and the temperature $k_BT = 1/\beta$.

For a general two terminal contact which can be presented by a set of transmission matrix eigenvalues T_n, we can write the Hamiltonian as

$$H = H_L + H_R + H_T \quad (2.9)$$

where H_T describes the coupling between the current and the environment. By doing the perturbation expansion in H_T to the second order, we can get the result for the current with the the Keldysh Green's functions $\check{G}_{L,R}$ for the free electrons on the left (L) and right (R) sides of the tunneling barrier as [74]

$$\check{I} = -\frac{e^2}{\pi}\sum_n \frac{T_n[\check{G}_L, \check{G}_R]}{4 + T_n(\{\check{G}_L, \check{G}_R\}) - 2} \quad (2.10)$$

with $\check{\tau}_K$ denoting the current matrix operator.

From the Full Counting Statistics, it gives

$$\mathbb{S}(\chi) = \int_0^{\chi} d\chi' I(\chi'), \tag{2.11}$$

$$I(\chi) = \frac{1}{4e} \int dE tr[\check{\tau}_K \check{I}] \tag{2.12}$$

with tr = trace in Keldysh-Nambu-... space, then the corresponding action $\mathbb{S}_c$ can be yield [73, 75]:

$$\mathbb{S}_c = \frac{i}{2} \sum_n Tr \ln[1 + \frac{T_n}{4}(\{\check{G}_L(\varphi), \check{G}_R\} - 2)]. \tag{2.13}$$

With the help of the equilibrium Keldysh Green's function

$$\check{G}_{eq}(\omega) = \begin{pmatrix} 1 - 2f(\omega) & 2f(\omega) \\ 2[1 - f(\omega)] & 2f(\omega) - 1 \end{pmatrix}, \tag{2.14}$$

containing the Fermi function $f(\omega) = [\exp(\beta\omega) + 1]^{-1}$, we can write $\check{G}_R(\omega) = \check{G}_{eq}(\omega - eV)$ and hence $\check{G}(t) = \int d\omega \exp(-i\omega t)\check{G}(\omega)/2\pi$. Again through the Fourier representation, $\check{G}_L(t, t') = \check{U}^{\dagger}(t)\check{G}_{eq}(t - t')\check{U}(t')$ with the counting fields introduced as a gauge transform in one of the reservoirs,

$$\check{U}(t) = \begin{pmatrix} e^{-i\varphi^+(t)} & 0 \\ 0 & e^{-i\varphi^-(t)} \end{pmatrix}. \tag{2.15}$$

2.2.2 Expansion

According to Eq. 2.13, we can see that if considering the transmission T_n is quite small, by letting $\ln(1 + x) = x$ and expanding the exponential $e^{-i\varphi}$ into

higher order of the phase φ, the action of the coherent conductor just becomes

$$\begin{aligned}
\mathbb{S}_c \sim \frac{i}{2}\sum_n \frac{T_n}{4}\int dtdt'\{&[1+i\varphi^+(t)-\frac{1}{2}\varphi^+(t)^2-\frac{i}{6}\varphi^+(t)^3+\frac{1}{24}\varphi^+(t)^4+\dots]F_1(t-t')\\
&\times[1-i\varphi^+(t')-\frac{1}{2}\varphi^+(t')^2+\frac{i}{6}\varphi^+(t')^3+\frac{1}{24}\varphi^+(t')^4+\dots]\\
&+[1+i\varphi^+(t)-\frac{1}{2}\varphi^+(t)^2-\frac{i}{6}\varphi^+(t)^3+\frac{1}{24}\varphi^+(t)^4+\dots]F_2(t-t')\\
&\times[1-i\varphi^-(t')-\frac{1}{2}\varphi^-(t')^2+\frac{i}{6}\varphi^-(t')^3+\frac{1}{24}\varphi^-(t')^4+\dots]\\
&+[1+i\varphi^-(t)-\frac{1}{2}\varphi^-(t)^2-\frac{i}{6}\varphi^-(t)^3+\frac{1}{24}\varphi^-(t)^4+\dots]F_3(t-t')\\
&\times[1-i\varphi^+(t')-\frac{1}{2}\varphi^+(t')^2+\frac{i}{6}\varphi^+(t')^3+\frac{1}{24}\varphi^+(t')^4+\dots]\\
&+[1+i\varphi^-(t)-\frac{1}{2}\varphi^-(t)^2-\frac{i}{6}\varphi^-(t)^3+\frac{1}{24}\varphi^-(t)^4+\dots]F_1(t-t')\\
&\times[1-i\varphi^-(t')-\frac{1}{2}\varphi^-(t')^2+\frac{i}{6}\varphi^-(t')^3+\frac{1}{24}\varphi^-(t')^4+\dots]-2\},
\end{aligned} \tag{2.16}$$

with the defined F-functions containing the left-lead and right-lead Fermi function f_L and f_R

$$F_1(\omega)=\textstyle\int\frac{d\epsilon}{2\pi}[1-2f_L(\epsilon)][1-2f_R(\epsilon-\omega)], \tag{2.17}$$

$$F_2(\omega)=\textstyle\int\frac{d\epsilon}{2\pi}4f_L(\epsilon)[1-f_R(\epsilon-\omega)]=\frac{2}{\pi}\frac{-\omega-eV}{1-e^{-\beta(-\omega-eV)}}, \tag{2.18}$$

$$F_3(\omega)=\textstyle\int\frac{d\epsilon}{2\pi}4f_R(\epsilon-\omega)[1-f_L(\epsilon)]=\frac{2}{\pi}\frac{\omega+eV}{1-e^{-\beta(\omega+eV)}}. \tag{2.19}$$

Consequently, the action of the tunneling conductor $\mathbb{S}_c$ can be simply written down as the sum of the terms that showing its relation with different power of field φ,

$$\mathbb{S}_c=\mathbb{S}_c^{(1)}+\mathbb{S}_c^{(2)}+\mathbb{S}_c^{(3)}+\mathbb{S}_c^{(4)}+\dots. \tag{2.20}$$

It is known that if we consider the system which can be performed in terms of independent harmonic oscillators, there is only quadratic contribution to the actions, i.e. $\mathbb{S}_e$ and $\mathbb{S}_c^{(2)}$, and the correlator $\langle e^{i\alpha\varphi(t)}e^{-i\alpha\varphi(0)}\rangle$ (Eq. 2.6) can thus be solved by the fundamental Gaussian integral. Then we can get the tunnelling rate Γ (Eq. 2.5) that is consistent with the standard P(E) theory (see Chapter 1.5). At the same time, due to the non-quadratic contribution to the action of the conductor, i.e., the higher order terms of φ (Eq. 2.20), the correlator can not be

solved exactly any longer and we need the further approximation scheme, which we will introduce later in Chapter 3.

2.2.3 Method through the equation of motion

Moreover, from above, we learn that the rate is related to the correlator $\langle e^{i\varphi(t)}e^{-i\varphi(0)}\rangle$. If we only consider the simple linear coupling to the environment, then the rate will be associated with $\langle\varphi(t)\varphi(t')\rangle$. For such system that the tunnel junction coupled to the electromagnetic environment, we can directly apply the method of equation of motion for the voltage fluctuation φ to calculate this phase-phase correlation.

We again start from the Hamiltonian of the tunnel junction, which can be expressed as [24, 26, 39, 40]

$$\begin{aligned} H_L = \textstyle\sum_k \varepsilon_k c_k^\dagger c_k, \quad H_R = \textstyle\sum_{k'} \varepsilon_{k'} c_{k'}^\dagger c_{k'}, \\ H_t = t \textstyle\sum_{k,k'} c_{k'}^\dagger c_k e^{-i\varphi} + h.c., \end{aligned} \tag{2.21}$$

with the phase $\varphi(t) = \frac{e}{\hbar}\int_{-\infty}^{t} U(t')dt'$ [23, 24] describing the voltage fluctuation due to the coupling to the electromagnetic environment.

Then by performing a time-dependent unitary transformation with

$$U = \prod_k \exp(i\frac{e}{\hbar}Vtc_k^\dagger c_k), \tag{2.22}$$

and assuming the linear coupling with the phase $\tilde{\varphi}$, the Hamiltonian of the tunnel junction turns to be

$$\begin{aligned} H_L + H_R = \textstyle\sum_k (\varepsilon_k - eV) c_k^\dagger c_k + \textstyle\sum_{k'} \varepsilon_{k'} c_{k'}^\dagger c_{k'}, \\ \tilde{H}_t = t \textstyle\sum_{k,k'} c_{k'}^\dagger c_k (-i\tilde{\varphi}) + h.c., \end{aligned} \tag{2.23}$$

with $\tilde{\varphi}(t) = \varphi(t) - \frac{e}{\hbar}Vt$ introducing the variance. From this, we can see that in the absence of the electromagnetic environment, the factor $-i\tilde{\varphi}$ has vanished and the Eq. 2.23 becomes the same with the normal tunnel junction.

Besides, the electromagnetic environment can be represented by a set of harmonic oscillators viewed as LC-circuit and bilinearly coupled to φ, so we can write down the Hamiltonian of the environment with an external voltage source by using the phase $\tilde{\varphi}$ and the charge $\tilde{Q} = Q - CV$ [27, 76, 77]

$$H_e = \frac{\tilde{Q}^2}{2C_0} + \frac{(\hbar/e)^2}{2L_0}\tilde{\varphi}^2 + \sum_{n=1}^{N}[\frac{q_n^2}{2C_n} + (\frac{\hbar}{e})^2\frac{1}{2L_n}(\tilde{\varphi} - \varphi_n)^2], \tag{2.24}$$

where the number N describing the environmental degrees of freedom should be rather large to keep the dissipative environment effective. As a consequence, collecting the Hamiltonians Eq. 2.23 and Eq. 2.24, the total Hamiltonian of the whole system of the tunnel junction coupled to the electromagnetic environment is

$$H_{tot} = H_L + H_R + \tilde{H}_t + H_e. \tag{2.25}$$

To obtain the final phase-phase correlation $\langle\varphi(t)\varphi(t')\rangle$, we first derive the Heisenberg equations of motion for φ_n, $\tilde{Q}$, q_n and $\tilde{\varphi}$:

$$\frac{d\varphi_n}{dt} = \frac{e}{\hbar}\frac{q_n}{C_n}; \tag{2.26}$$

$$\frac{d\tilde{Q}}{dt} = -\frac{\hbar}{e}\sum_n \frac{1}{L_n}(\tilde{\varphi} - \varphi_n) - \frac{\hbar}{e}\frac{1}{L_0}\tilde{\varphi} - \frac{e}{\hbar}[t\sum_{kk'}(-i)c_{k'}^{\dagger}c_k + h.c.]; \tag{2.27}$$

$$\frac{dq_n}{dt} = \frac{\hbar}{e}\frac{1}{L_n}(\tilde{\varphi} - \varphi_n); \tag{2.28}$$

$$\frac{d\tilde{\varphi}}{dt} = \frac{e}{\hbar C_0}\tilde{Q}, \tag{2.29}$$

and then the corresponding second derivatives are:

$$\frac{d^2\varphi_n}{dt^2} = -\omega_n^2\varphi_n + \omega_n^2\tilde{\varphi}; \tag{2.30}$$

$$\frac{d^2\varphi}{dt^2} = -\omega_0^2\tilde{\varphi} - \frac{1}{C_0}\frac{e^2}{\hbar^2}[t\sum_{kk'}(-i)c_{k'}^{\dagger}c_k + h.c.] + \frac{1}{C_0}\frac{\varphi_n}{L_n} - \frac{1}{C_0}\frac{\tilde{\varphi}}{L_n}, \tag{2.31}$$

in which $\omega_0^2 = \frac{1}{L_0C_0}$ and $\omega_n^2 = \frac{1}{L_nC_n}$ give the frequencies of the harmonic oscillators.

By solving the partial equations, we can get the general solution of $\varphi_n(t)$

$$\varphi_n(t) = \varphi_n^{(0)}(t) + \omega_n\int_{t_0}^{t}\sin[\omega_n(t-t')]\tilde{\varphi}(t')dt', \tag{2.32}$$

and substituting it into Eq. 2.30, at last we obtain

$$\frac{d^2\varphi}{dt^2} = -\omega_0^2\tilde{\varphi} - \frac{1}{C_0}\frac{e^2}{\hbar^2}\tilde{I} + \frac{1}{C_0}\Phi(t) - \frac{1}{C_0}\int_{t_0}^{+\infty} dt' Y(t-t')\frac{d\tilde{\varphi}(t')}{dt'}, \tag{2.33}$$

in which

$$\tilde{I} = t\sum_{kk'}(-i)c_{k'}^{\dagger}c_k + h.c., \tag{2.34}$$

$$\Phi(t) = \sum_n \frac{1}{L_n}[\varphi_n^{(0)}(t) - \cos[\omega_n(t-t_0)]\tilde{\varphi}(t_0)], \tag{2.35}$$

$$Y(t-t') = \theta(t-t')\sum_n \frac{1}{L_n}\cos[\omega_n(t-t')] \tag{2.36}$$

relate to the current operator, the environment noise and the admittance of the electromagnetic environment, separately.

After applying the Fourier transform into the Eq. 2.33, we eventually yield the expression for the phase $\tilde{\varphi}$:

$$\tilde{\varphi}(\omega) = \frac{1}{C_0}\frac{(e^2/\hbar^2)\tilde{I}(\omega) - \Phi(\omega)}{\omega^2 - \omega_0^2 - i\omega Y(\omega)/C_0}. \tag{2.37}$$

From Eq. 2.37, we can see that the first term including $\tilde{I}$ is referring to the current of the tunnel junction without the phase coupling through its definition, and the second term is linked with the electromagnetic environment. Thereby, with Eq. 2.37, the evaluation of the phase-phase correlation $\langle\tilde{\varphi}(t)\tilde{\varphi}(t')\rangle$ can be transferred to the calculation the normal current-current fluctuation $\langle\tilde{I}(t)\tilde{I}(t')\rangle$ within which there is no phase coupling in the tunnel junction. For instance, if taking the lowest order perturbation during the calculation of $\langle\tilde{I}(t)\tilde{I}(t')\rangle$, we can come into (Eq. 1.61) [33, 78–80]

$$\langle\tilde{I}(\omega)\tilde{I}(\omega')\rangle \sim \delta(\omega+\omega')\Big[\frac{\hbar\omega + eV}{1-\exp[-\beta(\hbar\omega+eV)]} + \frac{\hbar\omega - eV}{1-\exp[-\beta(\hbar\omega-eV)]}, \tag{2.38}$$

and following Eq. 2.37, which gives

$$\langle\tilde{\varphi}\tilde{\varphi}\rangle_\omega \sim \langle\tilde{I}\tilde{I}\rangle_\omega, \tag{2.39}$$

we can get the same result with the Gaussian contribution (Eq. 3.13) in Chapter 3.

Chapter 3

Enhanced Light Emission from a Tunnel Junction via a localized Surface Plasmon Polariton

3.1 Introduction

In the investigation of electron transport through nano-systems, due to the quantum nature of the system, the current exhibits quantum noise with zero-point fluctuations [38, 81]. Obiviously, since it is a quantum property, the current needs to be replaced by current operators in the Heisenberg representation $\hat{I}(t)$. Hence, the noise spectral density $S(\omega) = \int dt e^{i\omega t}\langle\hat{I}(0)\hat{I}(t)\rangle$ shows a frequency-antisymmetric component $S(\omega) \neq S(-\omega)$ because of the no longer commuting current operators at different times. This asymmetry can actually be accessed by coupling the system to a detector [31, 33]. The result is that the positive and negative frequency branches are related to the emission and absorption spectrum respectively. Concerning the emission processes, if the source of noise is the system biased by a voltage V, intuitively one expects that the maximum energy available for the tunneling electron is eV, and, thus, the energy of an emitted photon is limited to eV as well, as shown by several experiments and theoretical investigations [42, 43, 46, 51, 56, 82–87]. Such inelastic effects in tunneling junctions are

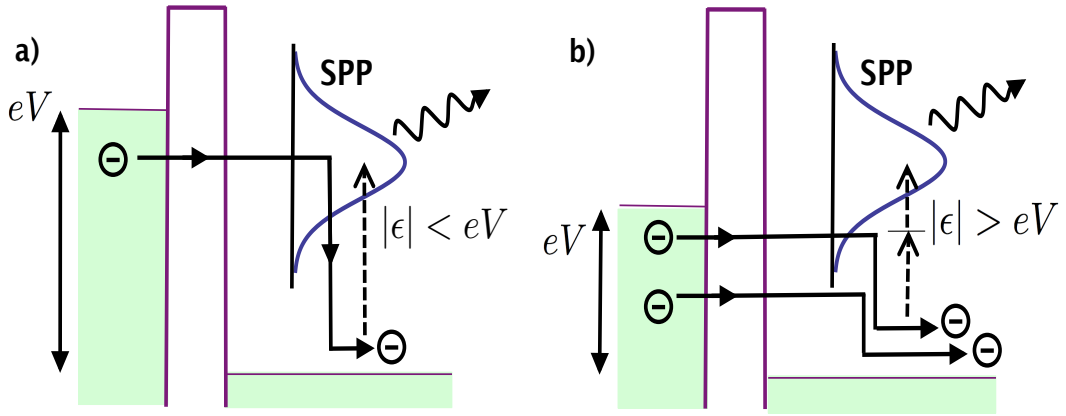

FIGURE 3.1: Sketch of electron tunneling processes. (a) One electron tunnels through the barrier and excites the surface plasmon-polariton (SPP), which eventually emits a photon with energy $|\epsilon| < eV$. (b) The two coherent electrons tunnel through the barrier, creating an overbias SPP excitation and leading to the overbias light emission with energy $|\epsilon| > eV$.

quite interesting because they can reveal unusual phenomena, helping to study the electron-electron effects.

In regard to experimental measurements and realizations of current noise detecting, one proposal is a quantum tunneling detector consisting of a double quantum dot (DQD) coupled to the leads of a nearby mesoscopic conductor [78], in which the inelastical current through the DQD measures the equilibrium and nonequilibrium fluctuations in the conductor [88].

Additionally, the light emission of electrons tunneling from a scanning tunneling microscope (STM) to a metallic surface has already been studied and used as a probe of the shot noise at optical frequencies for many years[21, 44, 45, 89, 90]. The basic mechanism leading to light emission has been identified as the interaction of the tunneling electrons with a localized surface plasmon polariton (SPP) mode [45].

Consider this mechanism in a simple picture, which shows that the emitted light spectrum is limited within the frequency up to the bias voltage $\hbar\omega \leq eV$. This is a consequence of the presence of the Pauli principle in the electronic leads, which prohibits the inelastic tunneling transitions with larger energy exchange than the energy difference between the two Fermi seas, consisting of noninteracting electrons in the leads. The SPP resonance, which is finally responsible for the

photon emission, acts as a frequency filter and hence the measured spectrum is essentially the SPP resonance cut off at a frequency $eV/\hbar$, see Fig. 3.1(a). This picture has been confirmed in numerous experimental [42] and theoretical [85] studies.

However, a closer look at some experiments [54, 55, 60, 91–94] reveals the unexpected feature of light emitted at energy exceeding the bias voltage $\hbar\omega > eV$. Such an overbias spectrum appears as reminiscent of the surface plasmon-polariton (SPP) modes which can be also observed via other methods. Using energy considerations, such a process can be attributed to two simultaneously tunneling electrons providing enough energy to explain the observation of over-bias emission. Then why the electrons tunnel in a correlated manner remains speculative. Using essentially energy considerations, such a process can be attributed to two simultaneously tunneling electrons providing enough energy to explain the overbias emission [57, 59].

Similar findings have also been reported in photon emission from Josephson junctions [61–67] and molecular films [68–71] with fluorescent emission of photons with energies above the threshold energy. In order to understand these diverse systems, a detailed understanding of the electron tunneling processes involved is necessary [95].

In this Chapter, we develop a theoretical approach based on the idea that on a short time scale multi-electron coherent processes appear at a tunnel junction, thus giving a theoretical framework for the description of the plasmon-mediated light emission by a tunnel contact based on the powerful method of dynamical Coulomb blockade. In qualitative terms, in an elemental tunneling event, an electron gains energy eV at bias voltage V but must pay a charging cost of $E_c \sim e^2/C$ with C the junction capacitance. Hence, after tunneling, a nonequilibrium situation occurs since the charge on the junction and the charge imposed by the voltage source are different. Now, when an impedance is connected in series to the tunnel junction, it allows us to discharge and dissipate energy, thus, reducing Coulomb charging effects. In other words, the electromagnetic environment of the junction crucially affects the charge tunneling events. The effect on the tunneling

is captured by the probability $P(E)$ of emitting an energy amount E to the electromagnetic environment. The so-called $P(E)$ function is related to the spectral density of voltage fluctuations, which in turn is determined by the impedance of the environment.[24, 26]

Going beyond the simple tunneling events, this framework captures the coherent two-electron tunneling process, where each electron contributes an energy $E_i \lesssim eV$ $(i = 1, 2)$ but the overall process creates an excitation in the broadened SPP spectrum with an energy exceeding the bias voltage $E_1 + E_2 > eV$, as shown in Fig. 3.1(b). Afterwards, the relaxation of the SPP's energy finally leads to the overbias light emission.

By modelling the SPP as a broadened, damped resonator, at zero temperature we have quantitatively reproduced the experimentally observed bias-voltage-dependent emission spectrum [54]. And we further extend our model to include a finite temperature in the general expression for the tunneling rate.

First, we confirm that the non-Gaussian voltage fluctuations in the tunnel junction explain the light emission with energy above the bias voltage, $\hbar\omega > eV$, in the limit of low temperature. Second, we provide a quantitative estimation for the typical temperature above which overbias emission is masked by thermal effects.

Indeed, finite temperature affects either the rate associated to the Gaussian voltage fluctuations or the rate associated to the non-Gaussian voltage fluctuations. For the Gaussian rate, we find that increasing the temperature gradually smears out the sharp boundary at emission energy $E = eV$ which occurs in the limit of vanishing temperature. For the non-Gaussian rate, finite temperature smooths the characteristic cusp of the overbias emission which is obtained at zero temperature. Such effects are prominent even in the relatively low temperature regime, namely $k_B T \sim 10^{-2}\hbar\Omega$ with $\Omega \sim \omega_0$, the average position of the SPP spectrum, or $\Omega \sim \eta$, its broadening. These results point out that the overbias emission spectrum is sensitive to finite temperature effects. However, remarkably, the non-Gaussian rate can still represent the leading term in the overbias range $E > eV$ for sufficiently low temperatures.

Hence, by analyzing the temperature dependence, the bias voltage dependence and their interplay for the individual rates, i.e. the Gaussian and the non-Gaussian one, we discuss how to distinguish finite temperature effects from the expected "zero-temperature" overbias emission.

In the end, we even go further to study the three-electron tunneling processes resulting into the light emission between the two-electron energy cutoff $2eV$ and three-electron energy cutoff $3eV$ and find out the similar expression with the one-electron and two-electron cases when the temperature $k_BT \ll eV$.

The main content of this Chapter can be found in the paper Ref. [57] and Ref. [58].

3.2 Model

We start by showing how we intend to model the interaction between the tunneling current and the SPP using methods of environmental Coulomb blockade theory [24, 26, 33].

According to the standard theory [24, 26, 33], we model the tunneling from the STM tip to the surface in an electromagnetic environment as the circuit diagram depicted in Fig. 3.2. We consider a tunnel conductor with a dimensionless conductance $g_c = R_Q/R_c$ with $R_Q = h/2e^2$ and R_c being the quantum and tunneling resistances, respectively. The junction is coupled to a damped LC circuit, which we model by an impedance $z_\omega = iz_0\omega\omega_0/(\omega_0^2 - \omega^2 + i\omega\eta)$, where $\omega_0 = 1/\sqrt{LC}$ is the resonance frequency of the SPP mode, $\eta = 1/RC$ models the damping and $z_0 = \sqrt{L/C}/R_Q$ is the scaled characteristic impedance. And we later determine these parameters from the experiment [54].

The interaction between the tunnel junction and the SPP occurs in this model via the dynamical voltage fluctuations on the node between the tunnel junction and the LRC circuit, which can be expressed by the phase variable $\varphi(t) = \frac{e}{\hbar}\int_{-\infty}^{t} dtV(t')$ that later in the Keldysh action technique can be written down as $\varphi_\omega^{\pm} = \phi_\omega \pm \frac{1}{2}\chi_\omega$.

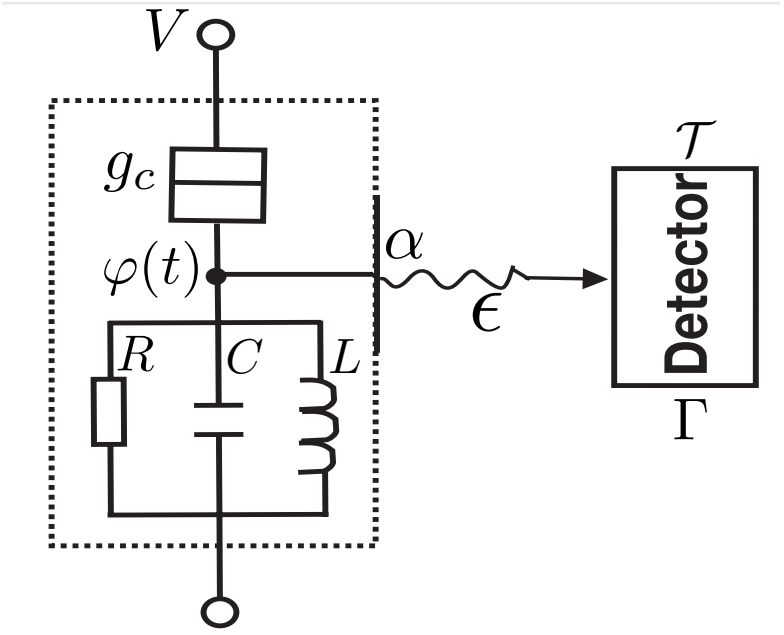

FIGURE 3.2: The electromagnetic model circuit: an LRC resonant circuit mimics the (damped) SPP and the photons emitted from the coupled tunnel junction are captured by the detector, which can be described as a two-level system for simplicity. See the text for further explanations of the parameters.

3.3 Approach—Path Integral formulations

As we have shown in the Chapter 2, to model the emission detection of the photons, we follow the standard path and model the detector as a simple two-level system, in which the emitted photons trigger transitions between states characterized by an energy difference ϵ and a transition probability $\mathcal{T}$. Formally the system can be described by a Hamiltonian $H_{detec} = (\epsilon + \alpha V)\sigma_z/2 + \mathcal{T}\sigma_x$ with the unperturbed eigenstates $|\pm\rangle$ with energies $\pm\epsilon/2$, respectively. The coupling constant α between the voltage fluctuations and the energy level of the detector, viz. $\epsilon \to \epsilon + \alpha e V(t)$ is set to be weak, since the photon detectors in a typical experiment are far away from the junction. We can calculate the transition rate from the transition probability $P_{-\to+}(t) = |\langle -(t)|+\rangle|^2$ to lowest order in the coupling $\mathcal{T}$.

Using Fermi's golden rule and setting $\hbar = 1$, the transition rate at energy ϵ in the detector due to the fluctuations of $\varphi(t)$ [24, 26, 72] is (see Eq. 2.5)

$$\Gamma(\epsilon) = |\mathcal{T}|^2 \int dt \langle e^{i\alpha\varphi(t)} e^{-i\alpha\varphi(0)} \rangle e^{i\epsilon t}. \tag{3.1}$$

This rate formula corresponds to emission or absorption for $\epsilon > 0$ and $\epsilon < 0$, respectively. In this work we study only the absorption rate and therefore we have to consider only negative energies $\epsilon < 0$. Our central theoretical task is the calculation of $\Gamma(\epsilon < 0)$ to the lowest order in the detector coupling constant, i.e., α.

In order to calculate $\langle e^{i\alpha\varphi(t)}e^{-i\alpha\varphi(0)}\rangle$, we employ the path integral method introduced in the Chapter 2, with the Keldysh actions of the conductor, $\mathbb{S}_c$, and the circuit, $\mathbb{S}_e$, the correlator can be represented as

$$\langle e^{i\alpha\varphi(t)}e^{-i\alpha\varphi(0)}\rangle = \int \mathcal{D}[\Phi]\exp\{-i\mathbb{S}_e[\Phi] - i\mathbb{S}_c[\Phi] + i\alpha[-\varphi^+(0) + \varphi^-(t)]\}, \quad (3.2)$$

where where the two-component phase $\Phi = (\phi, \chi)^T$ with $\phi = (\varphi^+ + \varphi^-)/2$ and $\chi = \varphi^+ - \varphi^-$, and the real fields $\varphi^{\pm}(t)$ are defined on the forward and backward Keldysh contours, respectively. Later in the Keldysh action, the real fields can be written as $\varphi^{\pm}_{\omega} = \phi_\omega \pm \frac{1}{2}\chi_\omega$ in frequency space.

The action of the damped LC oscillator acting as the environment on the tunnel conductor, is quadratic in the fields [13, 73] (see Eq. 2.7)

$$\mathbb{S}_e = \int \frac{d\omega}{2\pi}\,\Phi^T_{-\omega}A_\omega\Phi_\omega \quad (3.3)$$

$$A_\omega = -\frac{i}{2}\begin{pmatrix} 0 & -\frac{\omega}{z_{-\omega}} \\ \frac{\omega}{z_\omega} & W(\omega)\Re\{\frac{1}{z_\omega}\} \end{pmatrix}, \quad (3.4)$$

with $W(\omega) = \omega\coth(\omega/2T)$. Here T denotes the temperature and we have set $k_B = 1$.

And according to Eq. 2.13, by introducing the small transmission T_n, the action $\mathbb{S}_c$ can be expressed in terms of Keldysh Green's functions $\check{G}_{L,R}$ for the free electrons on the left (L) and right (R) sides of the tunneling barrier [75] as

$$\mathbb{S}_c = \frac{i}{8}g_c\int dtdt'\mathrm{Tr}\{\check{G}_L(t,t'),\check{G}_R(t'-t)\} \quad (3.5)$$

in the tunneling limit $g_c \ll 1$ [1]. With the help of the equilibrium Keldysh Green's function $\check{G}(\omega)$ (Eq. 2.14) and the counting fields $\check{U}(t)$ (Eq. 2.15).

Due to the nonquadratic contribution to the action of the conductor $\mathbb{S}_c$ in Eq. (3.5), the correlator cannot be calculated exactly and we need an approximation scheme. Here, we use the cumulant expansion for the action $\mathbb{S}_c$ by which we obtain the result

$$\Gamma(\epsilon) = \Gamma_{\mathrm{G}}(\epsilon) + \Gamma_{\mathrm{nG}}(\epsilon) + \mathcal{O}(\lambda^2)\,. \tag{3.6}$$

The first Gaussian term scales as $\Gamma_{\mathrm{G}}(\epsilon) \sim \Gamma_0 = (2\pi)^2\alpha^2|\mathcal{T}|^2 g_c z_0^2/\omega_0$ whereas the second non-Gaussian terms scales as $\Gamma_{\mathrm{nG}} \sim g_c z_0^2 \Gamma_0$ pointing out that the validity of our expansion is based on the smallness of the expansion parameter $\lambda = g_c z_0^2$.

3.4 Gaussian Contribution

A first approximation is obtained by considering only the quadratic part of the conductor action, in which the whole path integral becomes Gaussian and, in the limit of vanishing voltage $V = 0$, corresponds to the well-known results from P(E) theory. The quadratic part of the conductor action reads

$$\mathbb{S}_c^{\mathrm{G}} = \int \frac{d\omega}{2\pi}\, \Phi_{-\omega}^T B_\omega \Phi_\omega, \tag{3.7}$$

$$B_\omega = -\frac{i}{2}\begin{pmatrix} 0 & -\omega g_c \\ \omega g_c & S_c(\omega) \end{pmatrix}, \tag{3.8}$$

with the symmetrized quantum noise of a tunnel contact $S_c(\omega) = \frac{1}{2}g_c(W(\omega+eV)+W(\omega-eV)) \equiv g_c\widehat{W}(\omega)$. At zero temperature $T = 0$, the symmetrized quantum noise vanishes for $|\omega| > eV$ thus we can already conclude that, even if just the Gaussian part of the conductor action is included, Eq. (3.1) can only describe photon emission with energies limited by the bias voltage.

[1] Notice that, in the small tunneling limit $g_c \ll 1$ here considered, we have the Fano factor F=1 for the current noise.

Combining all the quadratic parts from both the LRC circuit and the conductor in a single matrix

$$D_\omega \equiv \frac{1}{2\pi}(A_\omega + B_\omega) = -\frac{i}{4\pi}\begin{pmatrix} 0 & -\frac{\omega}{\tilde{z}_{-\omega}} \\ \frac{\omega}{\tilde{z}_\omega} & S(\omega) \end{pmatrix}, \tag{3.9}$$

with $S(\omega) = S_c(\omega) + W(\omega)\Re\{\frac{1}{z_\omega}\}$. Then the correlation function $\langle e^{i\alpha\varphi(t)}e^{-i\alpha\varphi(0)}\rangle \equiv e^{\alpha^2 J(t)}$ can be evaluated. As a result, one finds

$$J(t) = \int d\omega \frac{|\tilde{z}_\omega|^2}{\omega^2} S_t(\omega)(e^{-i\omega t} - 1), \tag{3.10}$$

where

$$\begin{aligned} S_t(\omega) &= 2\pi(S(\omega) + \omega\Re\{1/\tilde{z}_\omega\}) \\ &= 2\pi g_c[\widehat{W}(\omega) + \omega] + 2\pi[W(\omega) + \omega]\Re\{1/z_\omega\} \end{aligned} \tag{3.11}$$

is the total noise spectral density. The impedance $\tilde{z}_\omega = z_\omega/(1 + z_\omega g_c)$ is the parallel connection of the tunnel junction and the environmental impedance playing as the "effective environment" to the detector. This means the factor g_c leads to an increased damping of the resonator, which can be absorbed in a renormalized $\eta \to \eta + 1/R_c C$ and will be ignored henceforth.

From Eq. (3.1), in the lowest order in α^2, we obtain the rate in scaled units,

$$\Gamma_{\rm G}(\epsilon) = 2\pi\alpha^2|\mathcal{T}|^2 \frac{|\tilde{z}_\epsilon|^2}{\epsilon^2} S_t(\epsilon)\,, \tag{3.12}$$

which is consistent with the known emission rate at finite temperature.

3.4.1 Zero Temperature Case

In the limit case $T \to 0$, i.e. at zero temperature, $W(\omega) = \omega\coth(\frac{\omega}{2T}) \to |\omega|$, and the result (3.12) reduces to the one obtained result [57], namely

$$\Gamma_{\rm G}(\epsilon) = \Gamma_0\, R_\eta\,(\epsilon)\;\theta\,(eV + \epsilon)\left(\frac{eV + \epsilon}{\omega_0}\right) \quad (T = 0)\;, \tag{3.13}$$

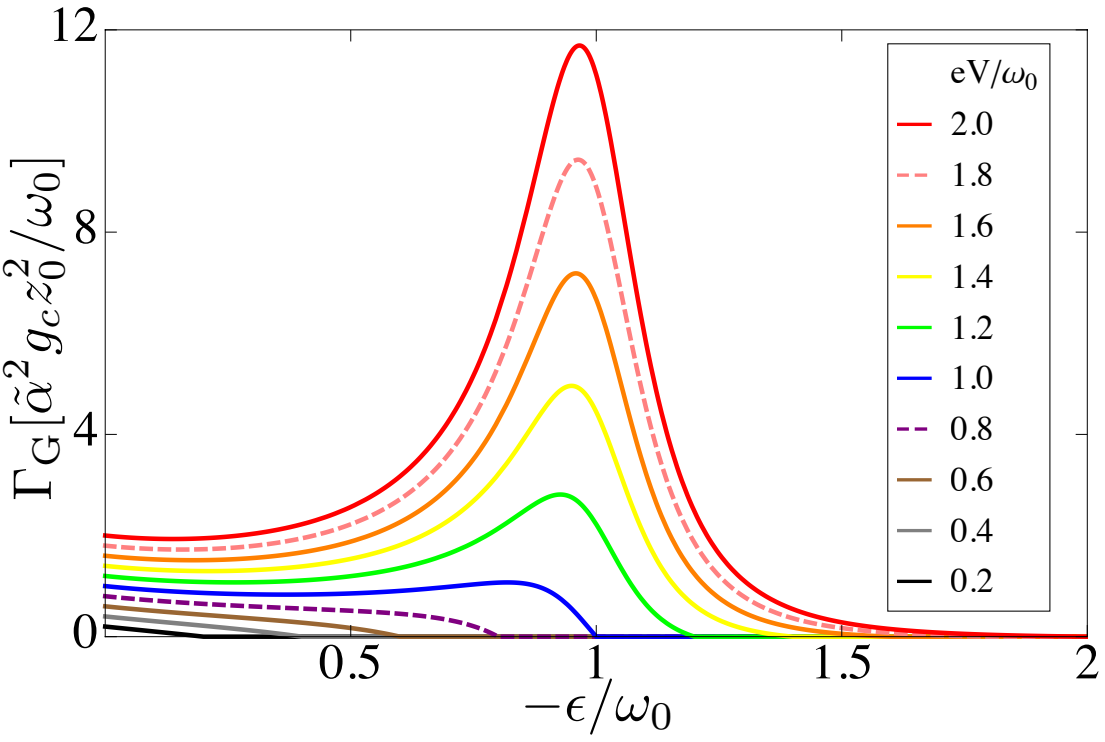

FIGURE 3.3: The Gaussian contribution to the emission spectrum for different bias voltages. The SPP peak becomes clearly visible as the bias voltage exceeds the resonance energy, ω_0. In all cases, the spectrum sharply drops to zero for $-\epsilon > eV$. This behaviour ascertains that the responsible processes are limited by single-electron tunneling events. The broadening parameter is chosen as $\eta = 0.3\omega_0$ and $\tilde{\alpha} = \alpha\mathcal{T}$.

in which we set the dimensionless resonance shape function $R_\eta(\epsilon) = 1/[(\epsilon^2/\omega_0^2 - 1)^2 + \epsilon^2\eta^2/\omega_0^2]$. Here, we have introduced a prefactor $\tilde{\alpha}^2 = |\mathcal{T}|^2\alpha^2$. In this limit the maximum energy eV for a photon emission due to inelastic transitions is eV as a consequence of the sharp Fermi surfaces on both sides of the tunnel junction and the emission spectrum has indeed a cutoff at $|\epsilon| = eV$, which matches the simple expectation from the golden rule [31].

The photon emission, that is described by energies $\epsilon < 0$, is only caused by the non-equilibrium electrons of the tunnel junction and is therefore limited by the maximum energy eV available for inelastic transitions. As the emission requires interaction with the environmental resonator, the electronic inelastic emission spectrum is filtered by the SPP resonance. This is demonstrated in Fig. 3.3 and Fig. 3.4, which show the emission rate for different bias voltages eV and

broadening parameters η, respectively.

In Fig. 3.3, there is always a sharp threshold for $-\epsilon = eV$ and the SPP resonance becomes visible if the threshold is larger than the resonance energy, ω_0. At a voltage below the resonance $eV < \omega_0$ in Fig. 3.4(a), the broadening has only a small influence on the emission spectrum and no peak occurs in the spectrum. The SPP resonance is visible only when the bias voltage becomes comparable or larger than the resonance ω_0, as shown in Fig. 3.4(b,c). For instance, in Fig. 3.4(b), close to the threshold eV the emission is enhanced, but the threshold remains clearly visible. In the limit of large bias voltage $eV > \omega_0$ (Fig. 3.4c), the full resonance is reflected in the emission spectrum and its shape is essentially determined by the resonance function appearing as a prefactor to the noise in Eq. (3.13). Hence, the maximum is $\sim 1/\eta^2$ and can be strongly increased in high-quality resonators or well-defined plasmonic modes.

3.4.2 Finite Temperature Case

At finite temperature, from Eq. (3.1), we can cast the Gaussian rate as

$$\Gamma_{\mathrm{G}}(\epsilon) = \Gamma_0 R_\eta(\epsilon) \left[\frac{\widehat{W}(\epsilon) + \epsilon}{\omega_0} + \left(\frac{1}{g_c z_0} \right) \frac{W(\epsilon) + \epsilon}{\omega_0} \right], \tag{3.14}$$

and the clear cutoff at $T = 0$ due to the Fermi distribution is smoothed out.

Figure 3.5(a) shows the emission rate for different temperatures at a voltage below the resonance $eV = 0.8\omega_0$ and for $g_c z_0 = 1$. Different values of the ratio $g_c z_0$ do not change the result significantly provided that $eV \gg T$ because the noise of the intrinsic thermal contribution of the plasmon - corresponding to the second term in Eq. (3.14) - scales as $\exp[-eV/T]$ around the cutoff $|\epsilon| = eV$ and it is hence exponentially small. Since a finite temperature softens the sharp cutoff at $|\epsilon| = eV$ that exists at zero temperature, the SPP resonance can come into play even at an energy lower than the bias voltage, thus contributing an overbias emission as well. The resonance strongly enhances the thermally excited overbias emission.

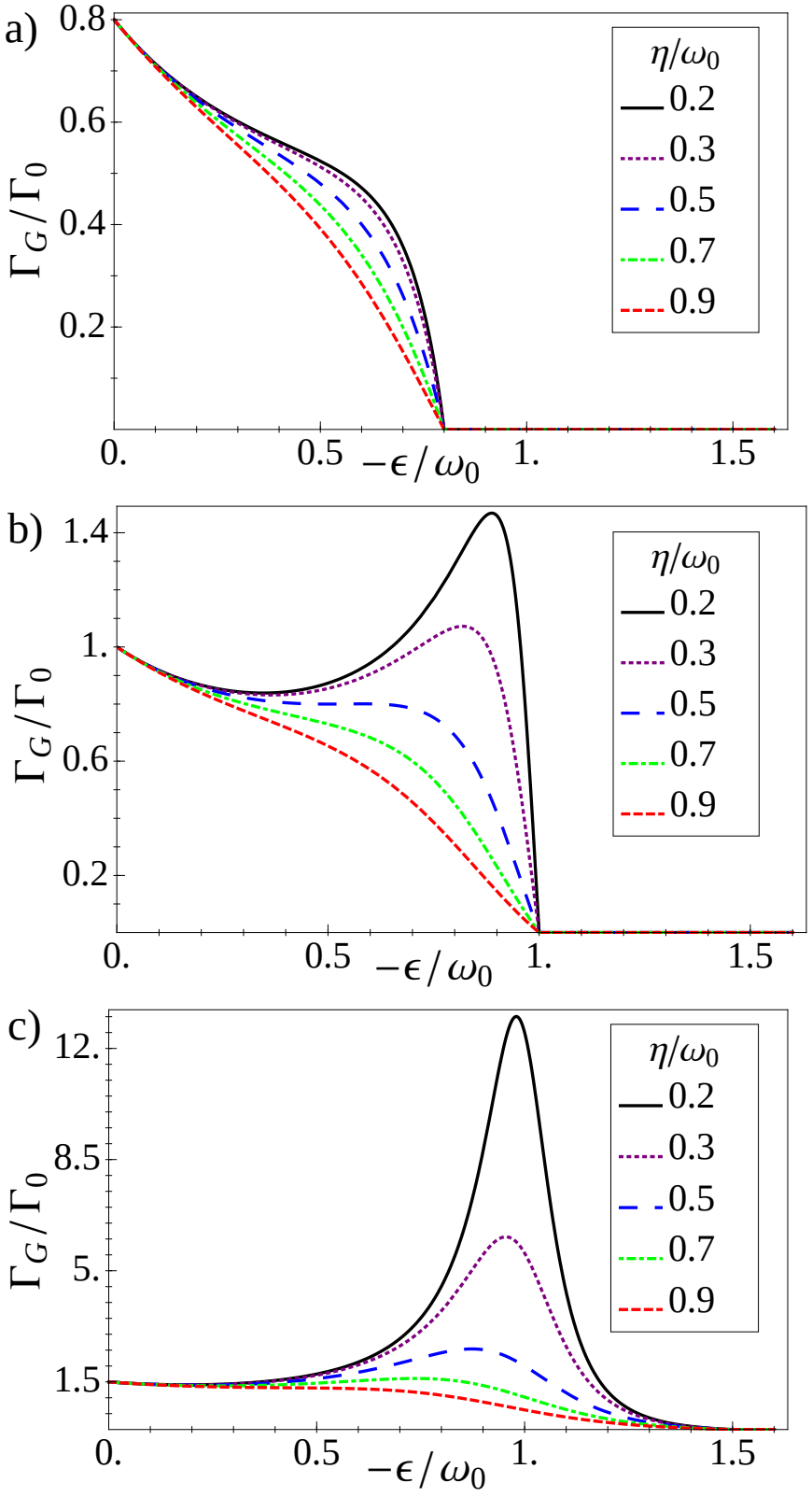

FIGURE 3.4: The Gaussian contribution to the emission spectrum for different broadenings, at zero temperature for three different values of the bias voltage: (a) voltage below the resonance $eV = 0.8\omega_0$, (b) voltage at the resonance $eV = \omega_0$, (c) voltage above the resonance $eV = 1.5\omega_0$. In all cases, the threshold occurs at $|\epsilon| = eV$. The SPP resonance becomes visible once that the threshold is larger than ω_0. The smaller the broadening η is, the sharper the SPP peak becomes.

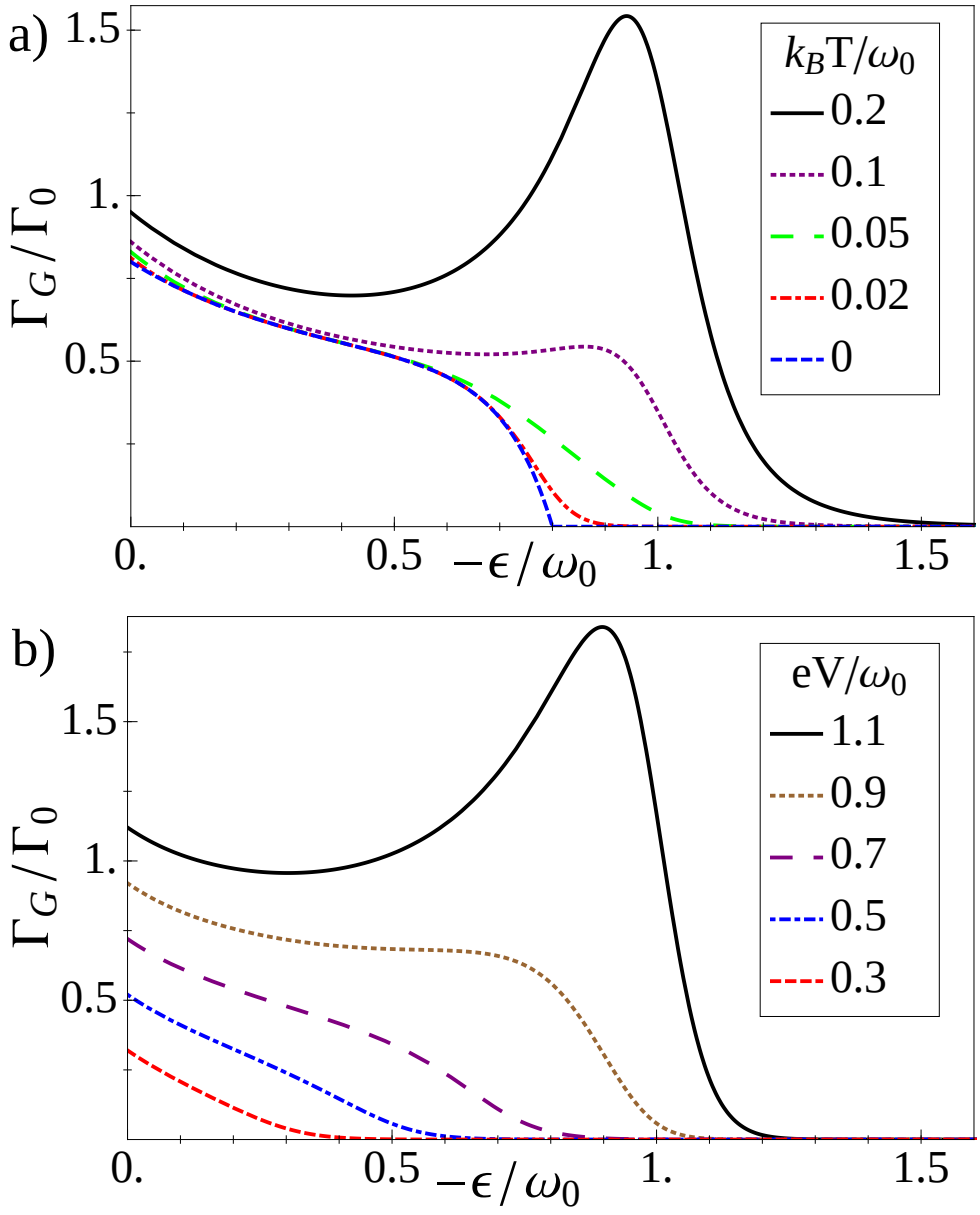

FIGURE 3.5: (a) The Gaussian contribution to the emission spectrum for different temperatures with the bias voltage $eV/\omega_0 = 0.8$. As the temperature is increased, the cutoff at the bias eV is washed out. In addition, more electrons are involved in the tunneling processes, leading to an increased rate. (b) The Gaussian contribution to the emission spectrum for different bias voltages. The SPP peak is more pronounced when the bias voltage exceeds the resonance energy ω_0. In all cases, the sharp threshold for $-\epsilon > eV$ that exists at zero temperature is smoothened at finite temperature, which is already achieved at the surprisingly small but finite temperature $T = \omega_0/30$. The broadening parameter in both figures is chosen as $\eta = 0.3\omega_0$ whereas the product of the tunneling conductance and the characteristic impedance of the resonator is set to $g_c z_0 = 1$.

It is remarkable that the step at eV is already almost invisible at a small temperature of just a few % of ω_0. This can be traced back to the thermally excited quasiparticles in the lead with the higher chemical potential - corresponding to the first term in Eq. (3.14) - so that the thermal tail at the resonance is $\sim \exp[-(\omega_0 - eV)/T]$ with $\omega_0 \sim eV$ and therefore exponentially larger than the intrinsic thermal contribution of the plasmon.

Figure 3.5(b) shows the emission rate for different bias voltages at low temperature $T = \omega_0/30$. In all cases, from bias voltages below the resonance $eV < \omega_0$ to bias voltages above the resonance $eV > \omega_0$, we have the disappearance of the zero temperature cutoff at $|\epsilon| = eV$. As long as the voltage becomes larger than $eV > \omega_0$, the SPP resonance becomes visible in the emission spectrum in a similar way to the case of vanishing temperature $T = 0$. In other words, at finite and small temperatures $T \ll \omega_0$, we have substantial corrections to the zero-temperature result for the Gaussian rate around the cutoff at $|\epsilon| = eV$.

3.5 High order cumulants and Non-Gaussian contribution

Although single-electron tunneling events produce signatures of the overbias SPP peak at finite temperature, we now turn to the nonquadratic part of the action $\mathbb{S}_c$ describing the electron-electron correlation that gives contributions to the overbias emission.

As pointed out [57], comparing the absolute orders of magnitude, the non-Gaussian phase fluctuations are smaller than the dominating Gaussian fluctuations due to the small environmental impedance $g_c z_\omega^2 \ll 1$. However, the non-Gaussian rate represents the only one contribution to the total rate in the overbias region $|\epsilon| \gg eV$ at $T = 0$. We aim to understand in which range of parameters, for sufficiently low temperature and well inside the overbias region $|\epsilon| > eV$, the non-Gaussian rate can continue to dominate over the thermal Gaussian rate.

Before discussing the results for the non-Gaussian rates, we report the main steps for calculating such a rate. Further details are given in Appendix.

Therefore, first, from Eq. (3.5),Eq. 2.14 and Eq. (2.15), we expand the action of the coherent conductor to the fourth order of φ while the higher-order terms can be neglected due to the factor $g_c z_\omega^2 \ll 1$, yielding $\mathbb{S}_c = \mathbb{S}_c^G + \mathbb{S}_c^{(3)} + \mathbb{S}_c^{(4)} + O(\Phi^5)$. The Gaussian part of the action can be combined with the environmental action, i.e., $\mathbb{S}_c^G + \mathbb{S}_e \rightarrow \mathbb{S}_c^G$. Due to the above assumptions, the remaining terms are small and we can make the expansion $\exp[-i\mathbb{S}_c^{(3)} - i\mathbb{S}_c^{(4)}] \approx 1 - i\mathbb{S}_c^{(3)} - i\mathbb{S}_c^{(4)}$. This approximation is possible since the Gaussian part of the action is dominated by the fluctuations of the small impedance of the environment, viz. $\Phi^2 < z_\omega/\omega^2$, and therefore the higher order terms are small by the factor $g_c z_\omega^2 \ll 1$. We can write the path integral as

$$\langle e^{i\alpha\varphi(t)} e^{-i\alpha\varphi(0)} \rangle \simeq e^{\alpha^2 J(t)} - i\langle\langle \mathbb{S}_c^{(3)} \rangle\rangle - i\langle\langle \mathbb{S}_c^{(4)} \rangle\rangle, \tag{3.15}$$

in which we used the Gaussian average

$$\langle\langle \cdots \rangle\rangle \equiv \int \mathcal{D}[\Phi](\cdots) e^{\int d\omega \{-i\Phi_{-\omega}^T D_\omega \Phi_\omega + i\alpha b_\omega^T(t)\Phi_\omega\}} \tag{3.16}$$

and

$$b_\omega(t) = (e^{-i\omega t} - 1, -(e^{-i\omega t} + 1)/2)^T. \tag{3.17}$$

After expanding for small α, the first term in Eq. (3.15) yields the Gaussian rate discussed in the previous section. Concerning $\mathbb{S}_c^{(3)}$, it is an odd term which gives a nonvanishing result only to the order α^3 and we neglect it for $\alpha \ll 1$.

Thus, we focus on the fourth term which is given in frequency space by

$$\begin{aligned}
\mathbb{S}_c^{(4)} = {} & \frac{1}{12}\frac{1}{(2\pi)^4}\frac{i}{8} g_c \int d\omega d\omega' d\omega'' \\
& \{\Big(2[F(\omega) + F(-\omega)] - 3[F_1(-\omega-\omega') + F_2(-\omega-\omega')]\Big) \\
& [\varphi^+(\omega')\varphi^+(\omega)\varphi^+(\omega'')\varphi^+(-\omega-\omega'-\omega'') \\
& + \varphi^-(\omega')\varphi^-(\omega)\varphi^-(\omega'')\varphi^-(-\omega-\omega'-\omega'')] \\
& - 4F(-\omega)\varphi^+(\omega)\varphi^-(\omega')\varphi^-(\omega'')\varphi^-(-\omega-\omega'-\omega'') \\
& - 4F(\omega)\varphi^-(\omega)\varphi^+(\omega')\varphi^+(\omega'')\varphi^+(-\omega-\omega'-\omega'') \\
& + 6F_1(-\omega-\omega')\varphi^+(\omega)\varphi^+(\omega')\varphi^-(\omega'')\varphi^-(-\omega-\omega'-\omega'') \\
& + 6F_2(-\omega-\omega')\varphi^-(\omega)\varphi^-(\omega')\varphi^+(\omega'')\varphi^+(-\omega-\omega'-\omega'')\}\,,
\end{aligned} \tag{3.18}$$

with

$$F_1(\omega) = (-\omega - eV) + W(-\omega - eV), \tag{3.19}$$

$$F_2(\omega) = (\omega + eV) + W(\omega + eV), \tag{3.20}$$

$$F(\omega) = F_1(\omega) + F_2(-\omega)\,. \tag{3.21}$$

For the field $\varphi^{\pm}_{\omega}$, the basic averages in frequency space can preferably be expressed in terms of the building blocks D_ω and $b_\omega(t)$:

$$\langle\langle \Phi_\omega \rangle\rangle = \langle\langle \begin{array}{c} \phi_\omega \\ \chi_\omega \end{array} \rangle\rangle = \frac{1}{2} D_\omega^{-1} b_{-\omega}(1 + \mathcal{O}[\alpha^2 z^2]), \tag{3.22}$$

$$\langle\langle \Phi_\omega \Phi^T_{-\omega} \rangle\rangle = \langle\langle \begin{array}{cc} \phi_\omega\phi_{-\omega} & \phi_\omega\chi_{-\omega} \\ \chi_\omega\phi_{-\omega} & \chi_\omega\chi_{-\omega} \end{array} \rangle\rangle = -\frac{i}{2} D_\omega^{-1}\,. \tag{3.23}$$

Replacing the expression of D_ω

$$\langle\langle \Phi_\omega \rangle\rangle = 2\pi i\alpha \begin{pmatrix} \left[S(\omega)\frac{|\tilde{z}_\omega|^2}{\omega^2} - \frac{1}{2}\frac{\tilde{z}_\omega}{\omega}\right] e^{i\omega t} - \left[S(\omega)\frac{|\tilde{z}_\omega|^2}{\omega^2} + \frac{1}{2}\frac{\tilde{z}_\omega}{\omega}\right] \\ -\frac{\tilde{z}_{-\omega}}{\omega} e^{i\omega t} + \frac{\tilde{z}_{-\omega}}{\omega} \end{pmatrix}, \tag{3.24}$$

$$\langle\langle \Phi_\omega \Phi^T_{-\omega} \rangle\rangle = 2\pi \begin{pmatrix} S(\omega)\frac{|\tilde{z}_\omega|^2}{\omega^2} & \frac{\tilde{z}_\omega}{\omega} \\ -\frac{\tilde{z}_{-\omega}}{\omega} & 0 \end{pmatrix}. \tag{3.25}$$

In the weak coupling limit, $\alpha \ll 1$, corresponding to weak detection that is the experimentally relevant regime, the main order pairings of averages appearing in $\mathbb{S}_c^{(4)}$ are of the type $\langle\langle\varphi_\omega\rangle\rangle\langle\langle\varphi_{-\omega}\rangle\rangle\langle\langle\varphi_{\omega'}\varphi_{-\omega'}\rangle\rangle$ and they are proportional to $\sim \alpha^2$. Such terms can be calculated using Wick's theorem to find all possible pairings of single and double averages. Contributions of zeroth order in α are time independent and therefore only play a part in the elastic rate characterized by $\epsilon = 0$, which is not of interest here.

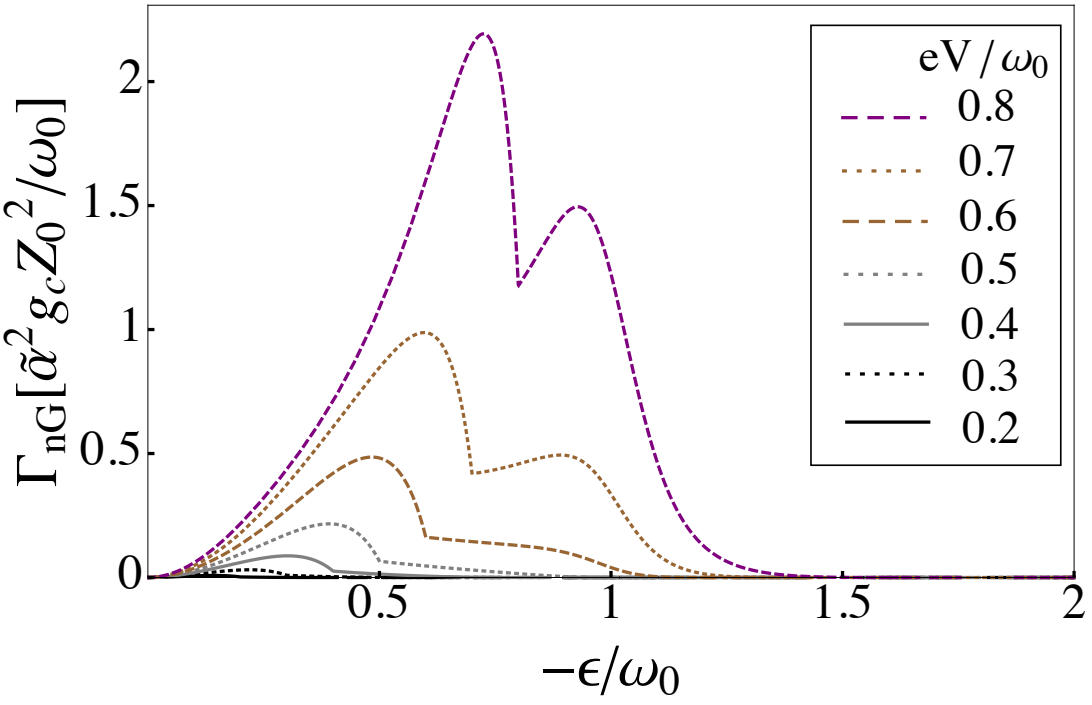

FIGURE 3.6: The non-Gaussian emission spectrum for different bias voltages at zero temperature. The spectrum is clearly induced by the SPP resonance and shows a kink at the bias voltage. The over-bias emission rate is distinctly visible and the scaling with g_c^2 shows that this effect is due to two-electron tunneling processes. The broadening of the resonance is $\eta = 0.3\omega_0$.

Finally, we consider only the lowest order terms in $\sim g_c^2$ in order to obtain the following expression for the non-Gaussian contribution:

$$\begin{aligned}
\Gamma^{(4)}_{\mathrm{nG}} = &\frac{\pi g_c^2 \alpha^2 |\mathcal{T}|^2}{2} \frac{|\tilde{z}_\epsilon|^2}{\epsilon^2} \int_0^\infty d\omega \\
&\left\{ \frac{|\tilde{z}_\omega|^2}{\omega^2} \left(\widehat{W}(\omega) - W(\omega) \right) \left[-2\widehat{W}(\epsilon) + \left(\widehat{W}(\omega+\epsilon) + \widehat{W}(\omega-\epsilon) \right) \right] \right. \\
&+2 \left(\widehat{W}(\epsilon) - W(\epsilon) \right) \frac{Re\{\tilde{z}_\epsilon\}}{\epsilon} \frac{Re\{\tilde{z}_\omega\}}{\omega} \left[\widehat{W}(\omega+\epsilon) - \widehat{W}(\omega-\epsilon) \right] \\
&+2 \left(\widehat{W}(\epsilon) - W(\epsilon) \right) \frac{Im\{\tilde{z}_\epsilon\}}{\epsilon} \frac{Im\{\tilde{z}_\omega\}}{\omega} \\
&\left. \times \left[2W(eV) - 2\widehat{W}(\omega) - 2\widehat{W}(\epsilon) + \widehat{W}(\omega+\epsilon) + \widehat{W}(\omega-\epsilon) \right] \right\}. \quad (3.26)
\end{aligned}$$

More details on the deriviation of this expression can be found in the Appendix.

3.5.1 Zero Temperature Case

Samely, considering the temperature limit $T = 0$, and limiting ourselves to the light emission, i.e. $\epsilon < 0$, we find the rate

$$\begin{aligned}\Gamma_{\mathrm{nG}}(\epsilon<0) = \frac{\pi\alpha^2|\mathcal{T}|^2 g_c^2}{2}\frac{|\tilde{z}_\epsilon|^2}{\epsilon^2}\int_0^\infty d\omega \\ \Bigg\{\frac{|\tilde{z}_\omega|^2}{\omega^2}\Big[\frac{1}{2}\xi(\omega)-|\omega|\Big]\Big[\frac{1}{2}\xi(\omega+\epsilon)+\frac{1}{2}\xi(\omega-\epsilon)-\xi(\epsilon)\Big] \\ +2\Big[\frac{1}{2}\xi(\epsilon)-|\epsilon|\Big]\frac{\Re\{\tilde{z}_\epsilon\}}{\epsilon}\frac{\Re\{\tilde{z}_\omega\}}{\omega}\Big[\frac{1}{2}\xi(\omega+\epsilon)-\frac{1}{2}\xi(\omega-\epsilon)\Big] \\ +2\Big[\frac{1}{2}\xi(\epsilon)-|\epsilon|\Big]\frac{\Im\{\tilde{z}_\epsilon\}}{\epsilon}\frac{\Im\{\tilde{z}_\omega\}}{\omega} \\ \times\Big[2|eV|+\frac{1}{2}\xi(\omega+\epsilon)+\frac{1}{2}\xi(\omega-\epsilon)-\xi(\omega)-\xi(\epsilon)\Big]\Bigg\}\end{aligned} \tag{3.27}$$

with $\xi(\omega) = |\omega + eV| + |\omega - eV|$. This result describes the influence of the non-Gaussian contribution to the light emission in the whole energy range, which means it also gives contributions in the under-bias as well as in the overbias regime. Note that it can be further simplified in the over-bias regime for $eV < -\epsilon < 2eV$ and takes the same form as in Ref. [72] to order α^2. We also see that the over-bias emission rate is $\sim g_c^2$, which signals the fact that a correlated two-electron tunneling process is responsible.

The non-Gaussian rate (3.27) at zero temperature explains the emission of photons with energies $-\epsilon > eV$. The detailed behavior of this rate as a function of energy is shown in Fig. 3.6 for different values of eV and Fig. 3.7 for different broadenings η. We observe that the rate has a distinct kink for $-\epsilon = eV$, which can be seen as a signature of the sharp Fermi edge. This leads, for $eV < \omega_0$, to a two-peak structure with peaks of comparable heights above and below the threshold voltage. For higher voltages, only a single peak at the resonance frequency remains.

Examples of the non-Gaussian rate at zero temperature are given in Fig. 3.7 scaled with $\lambda\Gamma_0$ and with $\lambda = g_c z_0^2$, our expansion parameter. Moreover, the non-Gaussian rate here calculated to lowest order in α and g_c has also a high-energy cutoff at $|\epsilon| = 2eV$ above which $\Gamma_{\mathrm{nG}} = 0$. The latter result is in agreement with the picture of two correlated electrons involved in a single photon emission

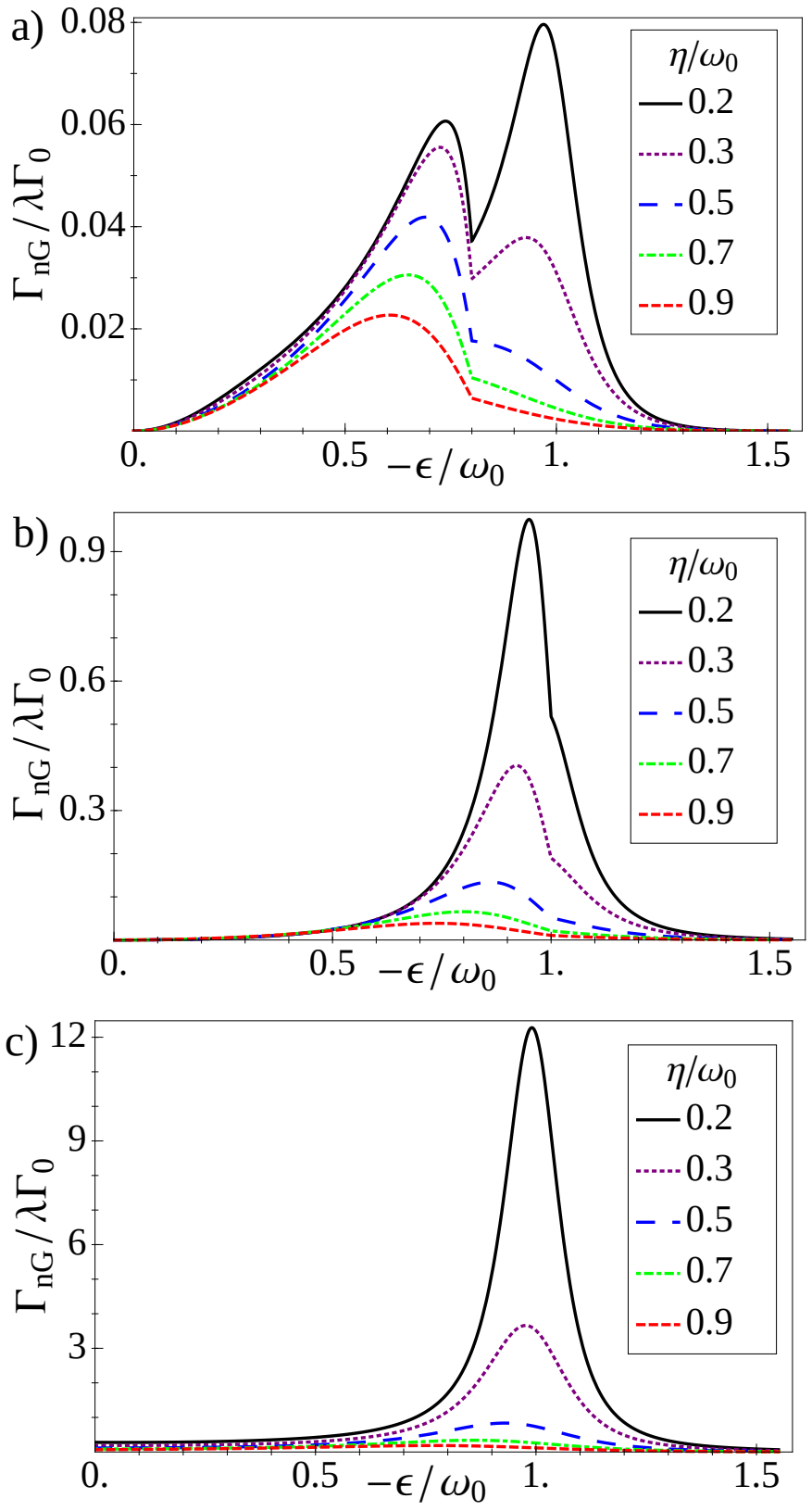

FIGURE 3.7: The non-Gaussian contribution at zero temperature to the emission spectrum for different broadenings. There is a kink for $|\epsilon| = eV$ whereas the resonance peak appears always at $|\epsilon| = \omega_0$. Parameters are the same as in Fig. 3.4, i.e. the bias voltage eV is set to be $0.8\omega_0, \omega_0$ and $1.5\omega_0$ referring for (a),(b),(c).

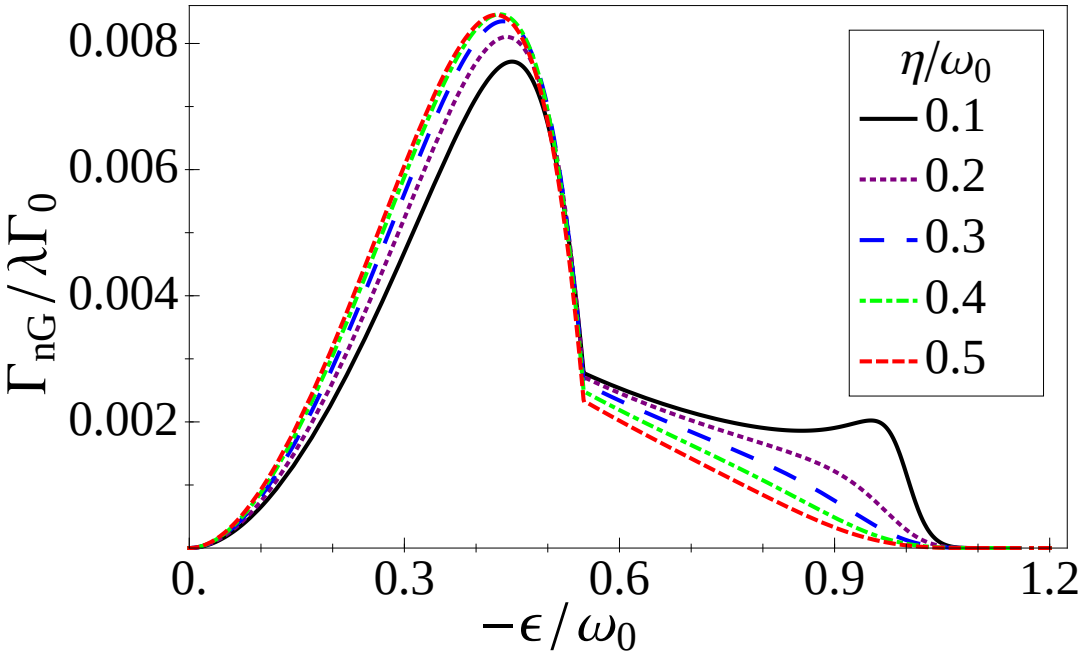

FIGURE 3.8: The non-Gaussian contribution at zero temperature to the emission spectrum for different broadenings. The bias voltage is $eV = 0.55\omega_0$ such that the two-electron energy cutoff is at $2eV = 1.1\omega_0$.

whose energy is now limited by $\hbar\omega < 2eV$. Such a cutoff is less pronounced than the sharp cutoff of the Gaussian rate at $|\epsilon| = eV$ although it is evident in the experimental data (see next section and Fig. 3.14).

As for the Gaussian case in Fig. 3.4, we plot in Fig. 3.7 the three different cases corresponding to bias voltages below or above the resonance $eV < \omega_0$ or $eV > \omega_0$, and the resonant case $eV = \omega_0$.

In the first case $eV < \omega_0$, Fig. 3.7(a), the curve for the non-Gaussian rate shows a characteristic cusp at the threshold $|\epsilon| = eV$. Such a curve has also peaks in both the under-bias region $|\epsilon| < eV$ as well as in the overbias region $|\epsilon| > eV$ in correspondence with the resonance of the SPP mode at $|\epsilon| = \omega_0$. The overbias emission at $T = 0$ corresponds to the first line of Eq. 3.26. However, in the under-bias region $|\epsilon| < eV$, the non-Gaussian rate is dominated by the leading Gaussian contribution so that the first peak hardly can be distinguished and one expects that the overbias emission rate is distinctly resolved around the resonance $\omega_0 > eV$ only.

For bias voltages at the resonance $eV = \omega_0$, Fig. 3.7(b), the two peaks associated with the non-Gaussian rate merges into a single peak and the curve shows a kink at the threshold $|\epsilon| = eV$. In this case the non-Gaussian rate has still a noticeable contribution in the overbias regime $|\epsilon| > eV$ in terms of the tail of the resonance peak centred at the threshold.

Then, for the last case, $eV > \omega_0$, shown Fig. 3.7(c), the non-Gaussian rate behaves in a way similar to the Gaussian rate in Fig. 3.7(c) with a single peak at the resonance $|\epsilon| = \omega$. Such a peak is now located well inside the under-bias region in which the non-Gaussian rate is dominated by the Gaussian rate.

Finally, we consider the case that when the SPP resonance ω_0 is quite close to the two-electron energy cutoff $2eV$, which is shown in Fig. 3.8. Here we can see, unlike Fig. 3.7(a) where the SPP resonance ω_0 is far away from the $2eV$ cutoff, that the overbias peak can still be present although strongly weakened.

Thus we can conclude that overbias photon emission due to the non-Gaussian voltage fluctuations in mesoscopic tunnel junctions is, a prori, always a possible effect even far away from the resonance of the plasma-polariton modes, but the effect's magnitude can be smaller than the limit of a photon detector. On the contrary, the overbias photon emission becomes a substantial effect provided that the system has a resonant plasmonic mode at a frequency in the overbias range $eV \geq \omega_0$ and below the cutoff for the two electrons emission $\omega_0 < 2eV$.

3.5.2 Finite Temperature Case

We discuss now the effects of a finite temperature for the non-Gaussian rate for the case $eV < \omega_0$. Some examples are shown in Fig. 3.9 with a intrinsic broadening of the SPP mode $\eta = 0.3\omega_0$.

In order to distinguish between the low and high temperature regimes, a priori we can compare the broadening η with the thermal smearing expected at finite temperature $\sim k_B T$. Then one expects that the non-Gaussian rate continues to exhibit sharp features in the low temperature range, defined by $k_B T < \eta$ and that it becomes a smooth, smeared function as the temperature approaches the

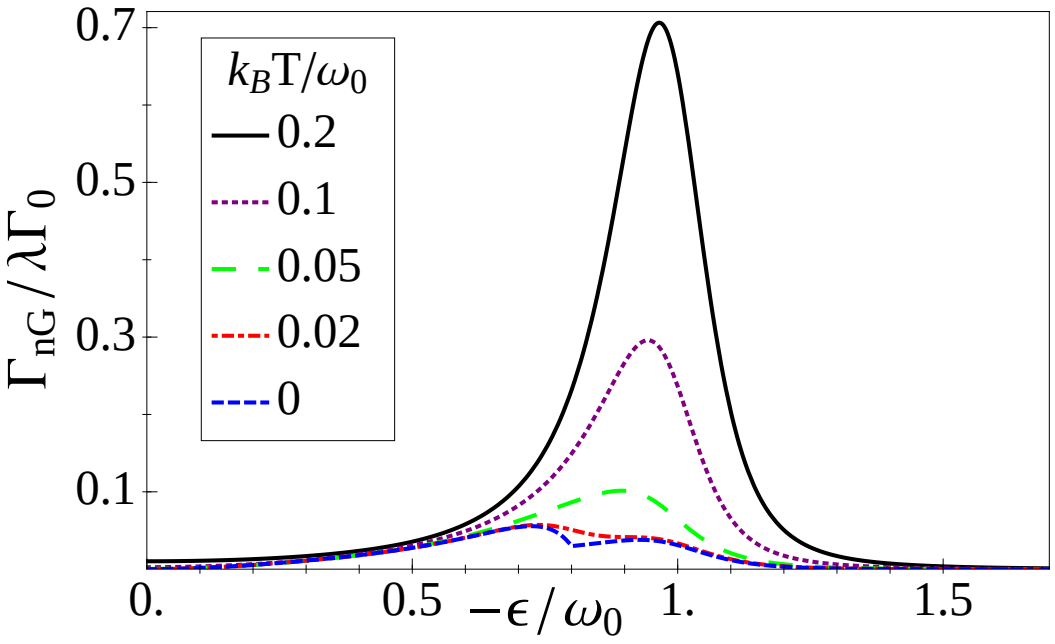

FIGURE 3.9: The non-Gaussian contribution to the emission spectrum for different temperatures at the bias voltage $eV/\omega_0 = 0.8$ and $\eta = 0.3\omega_0$. Due to the increased temperature, the kink at the bias disappears and the two peaks are merged into a single peak.

broadening $k_BT \lesssim \eta$. In Fig. 3.9, we can see that, increasing the temperature, the two distinct peaks merge into a single peak and the kink at the bias voltage $|\epsilon| = eV$ is weakened concealing any overbias signatures. Remarkably, this merging occurs even at relatively low temperature $T \sim 10^{-2}\omega_0$ compared to the broadening of the mode $\eta \sim 10^{-1}\omega_0$ pointing out that the overbias is highly sensitive to finite temperature.

On the other hand, increasing the temperature enhances the height of the peak in a similar way as the Gaussian rate, as discussed in the previous section. In other words, above the threshold $|\varepsilon| > eV$ and at finite temperature, one can not discriminate the overbias emission due to the Gaussian fluctuations - associated to single electron processes - from the overbias emission due to the non-Gaussian fluctuations - associated to two-electron processes. In order to resolve such processes, we have to consider the low temperature range.

In Fig. 3.10, we discuss the behavior of the non-Gaussian rate at low temperature, $T = \omega_0/30$, as varying the damping η when the resonance is close to the two-electron cutoff $2eV = 1.1\omega_0$. By comparing with the Gaussian part under the same condition - the inset of Fig. 3.10 - we notice that at finite temperature, since

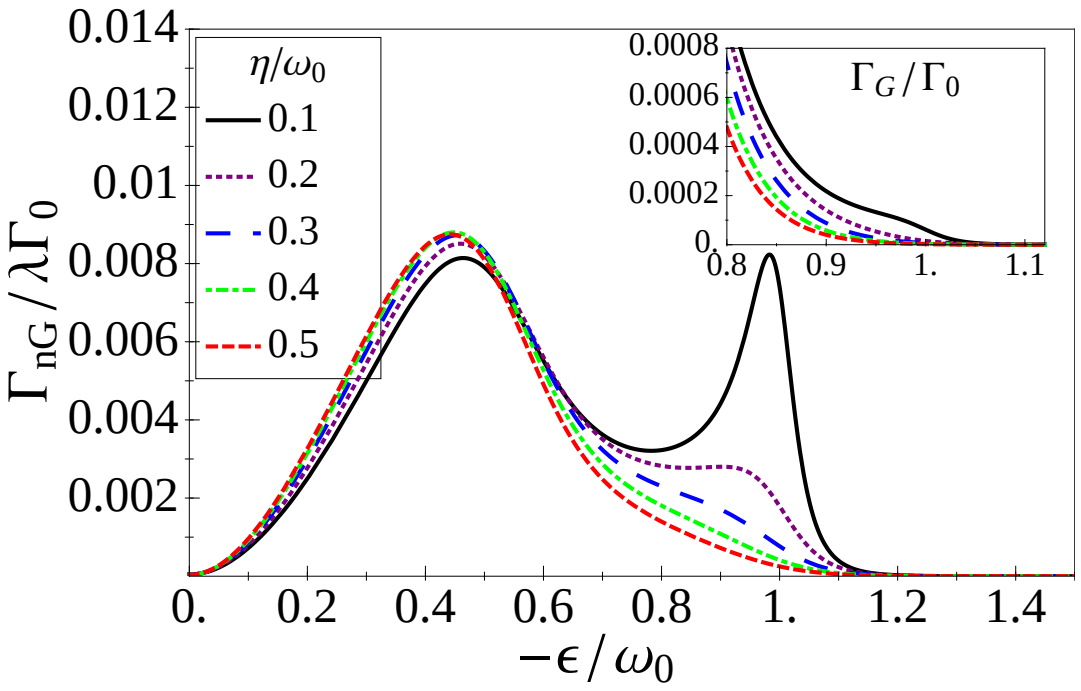

FIGURE 3.10: The non-Gaussian contribution at finite temperature $T = \omega_0/30$ to the emission spectrum for different broadenings, at $2eV = 1.1\omega_0$, viz. the SPP resonance dominates near the $2eV$ cutoff. The inset shows the Gaussian contribution around the SPP resonance. Thus, in this case, with proper λ, even at finite temperature, the overbias due to the two-electron emission (non-Gaussian part) can dominate the Gaussian one.

the bias voltage eV, that is important for the single electron emission, is far away from the resonance, the Gaussian part around the resonance is small as it is due to the temperature smearing of the Fermi distribution. Meanwhile, the non-Gaussian part can represent the larger contribution in the case of a sharp resonance.

3.6 Total Rate and comparison with the experiments

For the total tunneling rate, we have to take the Gaussian as well as the non-Gaussian rates into account. In order to compare the theoretical results with the experimental data of G. Schull and co-workers [54], in this section we plot the rate explicitly as a function of energy (eV) for a SPP mode centered at $\omega_0 = 1.8$ eV and broadening $\eta = 0.2$ eV.

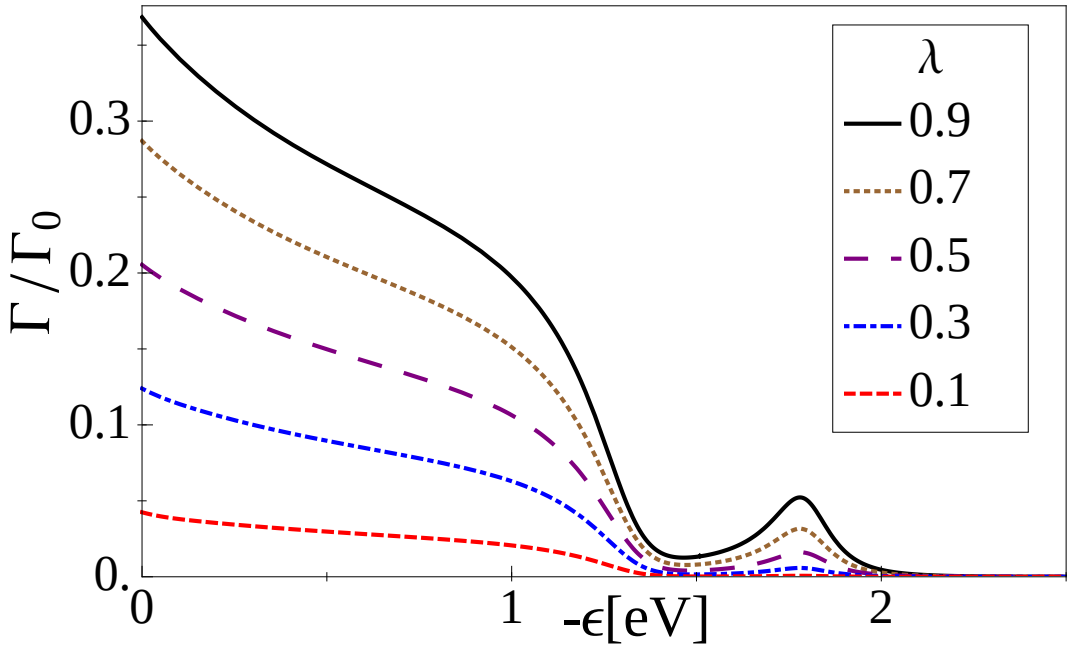

FIGURE 3.11: The total rate for different dimensionless factors $\lambda = g_c z_0^2$ at the bias voltage $V = 1.32$ V. The overbias peak increases with increasing λ, which determines the weight of the non-Gaussian part to the total rate. The temperature is chosen to be the room temperature $\beta\omega_0 = \omega_0/k_BT = 72$ and the SPP resonance energy is taken to be $\omega_0 = 1.8$ eV with the broadening $\eta = 0.2$ eV.

As is known from above, these two rates are normalized by a dimensionless factor of $\lambda = g_c z_0^2$. Then as λ increases, the non-Gaussian rate gradually gives the dominant contribution to the total emission rate in the overbias energy regime, leading to the overbias emission peak becoming more visible (see Fig. 3.11). However, for small λ, within the validity of our expansion, the non-Gaussian features are weak and smeared out by the Gaussian properties due to the finite temperature.

In fact, we can determine this parameter by comparison with the experimental results. In the inset of Fig. 3.12, we show the total rate $\Gamma = \Gamma_{\mathrm{G}} + \Gamma_{\mathrm{nG}}$ at zero temperature for two different bias voltages. These rates have to be compared to the results prestented in Fig. 2a of Ref. [54]. From the relative scaling of the two curves by a factor of 300 and the width of the resonance, we determine the parameters $g_c z_0^2 \approx 0.1$ and $\eta \approx 0.2\omega_0$, respectively. Note that the experimental results depend on the detailed surroundings of the STM tip's position. Using these parameters, we show the full bias-voltage and energy-dependent emission rate at zero temperature on a logarithmic scale in the main panel of Fig. 3.12. The

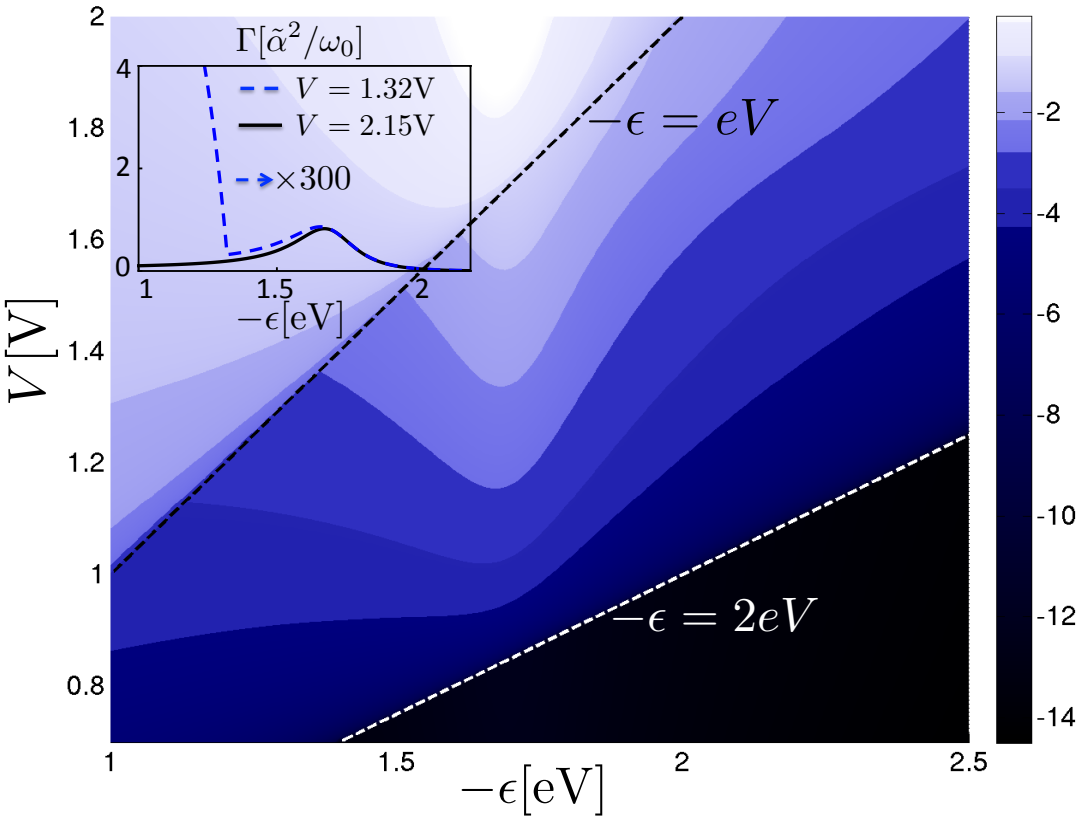

FIGURE 3.12: Main: Light emission spectrum on a logarithmic scale as a function of bias voltage at zero temperature. The SPP resonance energy is taken to be on the order of the experimental value $\omega_0 = 1.7$ eV, $g_c z_0^2 = 0.1$ and the broadening is taken to be $\eta = 0.2\omega_0$. The one- and two-electron thresholds at $-\epsilon = eV$ and $= 2eV$ are indicated by dashed lines. Inset: To extract the coupling parameter $g_c z_0^2 = 0.1$, we compare the peak values at $-\epsilon = \omega_0$ for two different bias voltages: V=2.15 V (solid line); V=1.32 V (dashed line). By scaling the low-bias curve by a factor 300, we find curves similar to those of Fig. 2a in Ref. [54]. Note that we have taken $\eta = 0.3\omega_0$ to achieve a better agreement of the resonance shape with the experiment.

comparison to Fig. 1b of Ref. [54] is striking although the resonance parameters in the experiment are different. We clearly observe the threshold behaviors at $-\epsilon = eV$ and $-\epsilon = 2eV$.

In addition, We investigate the temperature dependence of the total rate in Fig. 3.13 in logarithmic scale, in which the black line shows the zero temperature case, giving the clear kink at the bias voltage eV, described in Ref. [57]. Fig. 3.13 shows how the rate sensitively depends on the temperature; the clear kink at the bias voltage is quickly softened even at small finite temperatures, and the strong effect of the temperature appears when the temperature has the same order of the factor $eV - \omega_0$, leading to the single overbias peak as the temperature is increased.

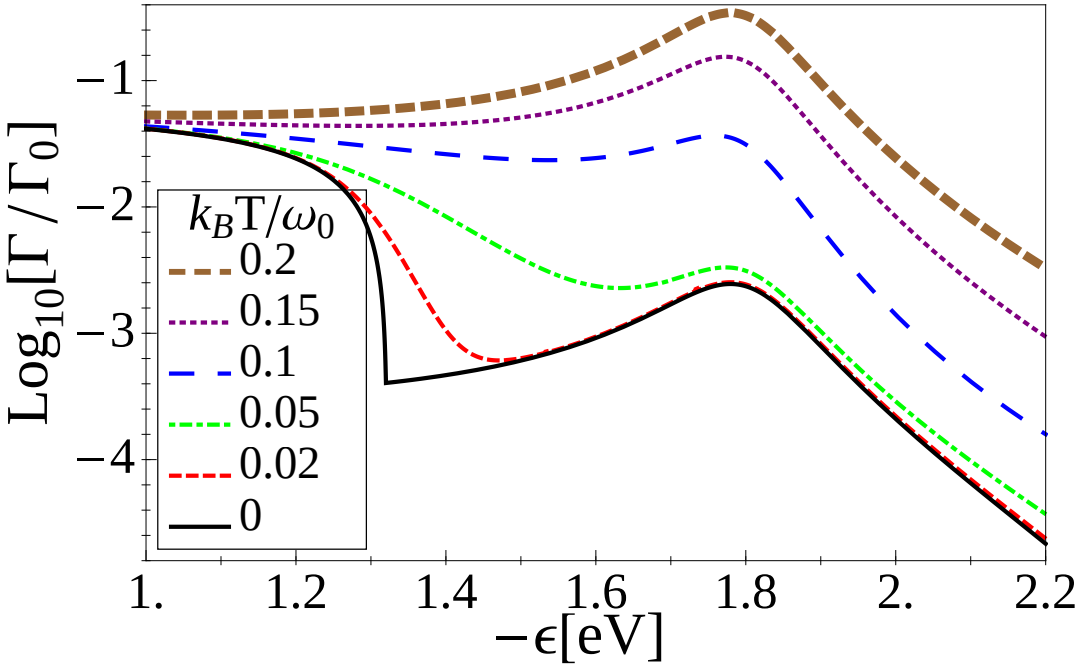

FIGURE 3.13: The logarithmic total emission rate at the bias voltage $V = 1.32$ V for different temperatures. The kink at the bias voltage becomes more distinct at lower temperature. The SPP resonance energy is taken to be $\omega_0 = 1.8$ eV, $\lambda = 0.2$, and the broadening is $\eta = 0.2$ eV.

And the coupling parameter is determined by scaling the peak value at $-\epsilon = \omega_0$ for the low bias $V = 1.32$ V by a factor of 300 versus the peak at the bias $V = 2.15$ V, and this yields $\lambda = 0.227$. The resulting voltage- and energy-dependent emission rate is shown in Fig. 3.14(a) at the experimental temperature $T \simeq 7$ K. For comparison, we also show the rate at room temperature $T \simeq 300$ K for $\lambda = 0.2$ in Fig. 3.14(b).

The resulting voltage- and energy-dependent emission rate is shown in Fig. 3.14 at the experimental temperature $T \simeq 7K$ [Fig. 3.14(a)] and at room temperature $T \simeq 300K$ [Fig. 3.14(b)], respectively. Since the experiment temperature $T \simeq 7K$, quite close to the zero temperature, we could see that Fig. 3.14(a) gives the distinct threshold at $-\epsilon = eV$ and shows good agreement with the experiment. By contrast, at room temperature Fig. 3.14(b), we find that the sharp threshold behavior at $-\epsilon = eV$ has been strongly weakened with the temperature effect and is relaxing into the over-bias SPP resonance. And this can also be displayed in the Fig. 3.13, where the turning point at the bias voltage appears only for the lower temperatures.

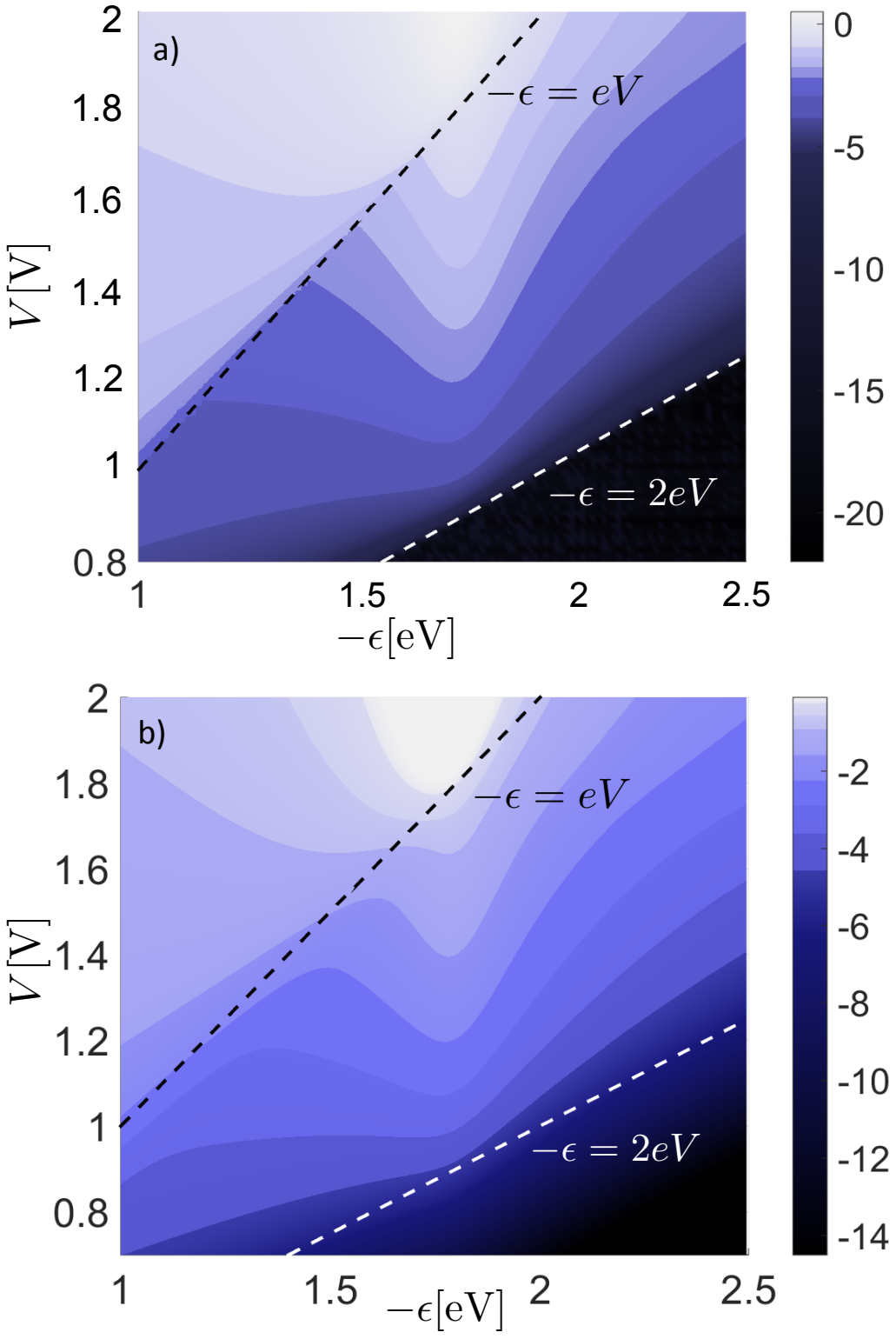

FIGURE 3.14: The light emission spectrum on a logarithmic scale as a function of bias voltage at (a) the low temperature $\beta\omega_0 = 3000$ and (b) room temperature $\beta\omega_0 = 72$. In panel (a), the clear threshold behavior reproduces the experimental findings [54] for the parameter $\lambda = 0.227$. In panel (b), the threshold at the bias voltage $-\epsilon = eV$ is less evident. This behavior depends sensitively on the temperature. Here, we use the parameter $\lambda = 0.2$. In both cases, the SPP resonance energy is taken to be $\omega_0 = 1.8$ eV, and the broadening is $\eta = 0.2$ eV.

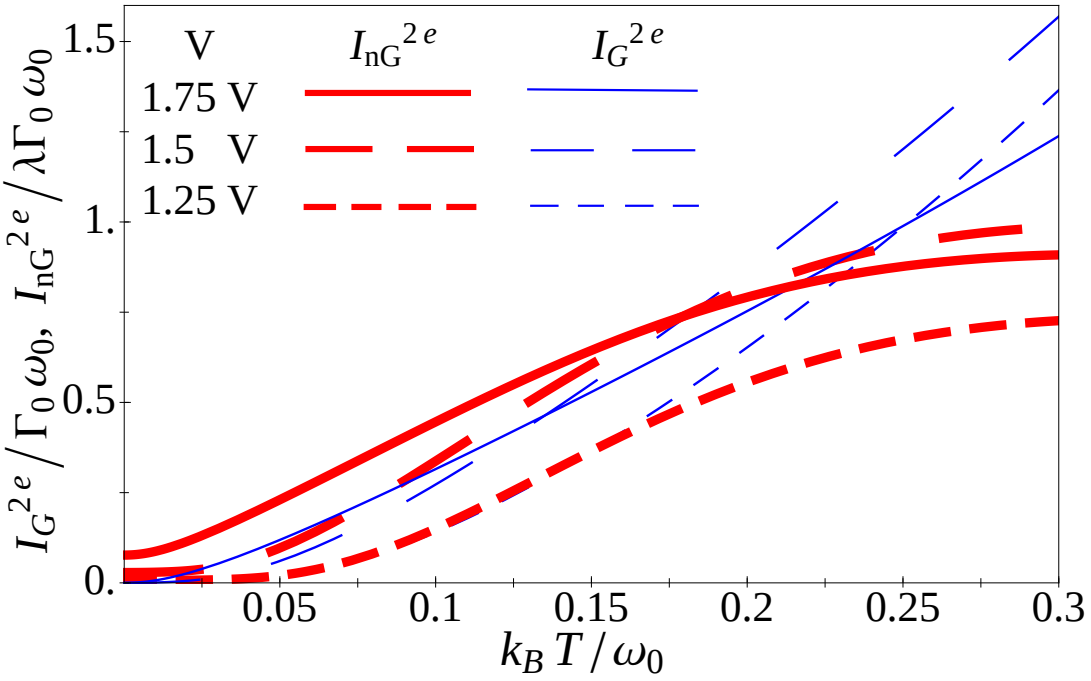

FIGURE 3.15: The temperature dependence of the scaled intensity for the Gaussian and non-Gaussian contribution. The SPP resonance energy is taken to be $\omega_0 = 1.8$ eV with the broadening $\eta = 0.2$ eV.

Since the experimental temperature is very low compared to the frequency scale of the SPP mode $\omega_0 \simeq 2 \cdot 10^4 K$, the rate in Fig. 3.14(a) exhibits a distinct threshold at $-\epsilon = eV$ and the clear overbias peaks at the SPP resonance due to the non-Gaussian contributions, which gives a good explanation and agreement with Ref. [54]. By contrast, at room temperature (Fig. 3.14(b)), we find that the sharp threshold behavior at $-\epsilon = eV$ has been weakened and is relaxing into the overbias SPP resonance due to the smoothed distribution function under the temperature effect. Meanwhile, the temperature effect has also sensitively hidden the two-electron energy cutoff line $-\epsilon = 2eV$, leading to the long and small tail into the energy larger than $2eV$.

Furthermore, we study the properties of the intensity of the overbias light emission as a function of the temperature. Since the non-Gaussian part has the prefactor $\lambda = g_c z_0^2$ compared to the Gaussian part, we consider the Gaussian and non-Gaussian emission separately and define their intensities as $I^{2e}_{\mathrm{G,nG}} = \int_{eV}^{2eV} \Gamma_{\mathrm{G,nG}} d\epsilon$, respectively. In Fig. 3.15, we observe that both the Gaussian and non-Gaussian intensities increase with temperature in the temperature range shown in the figure. It is interesting to note that for high enough temperature the heating effect

smears out the Fermi edge and leads to a saturation of the non-Gaussian emission. Furthermore, we find that the intensities do not increase monotonically with the bias voltages. Hence, it would be interesting to study the temperature dependence of the overbias light emission, in order to distinguish thermally induced emission from the pure quantum effect at low temperatures.

3.7 The three-electron tunneling processes

Moreover, we also consider about the three-electron tunneling case which is studied in the experiment. Following the above calculation method, we expand the conductor action to the sixth order of the phase φ, thus, getting the action of the tunnel conductor as

$$\begin{aligned}
\mathbb{S}^{(6)}_{cond} \sim \int dtdt' \{ & [\frac{1}{720}\varphi^+(t)^6 - \frac{1}{720}\varphi^+(t')^6 + \frac{1}{120}\varphi^+(t)\varphi^+(t')^5 + \frac{1}{120}\varphi^+(t)^5\varphi^+(t') \\
& -\frac{1}{48}\varphi^+(t)^2\varphi^+(t')^4 - \frac{1}{48}\varphi^+(t)^4\varphi^+(t')^2 + \frac{1}{36}\varphi^+(t)^3\varphi^+(t')^3]F_1(t-t') \\
& +[\frac{1}{720}\varphi^-(t)^6 - \frac{1}{720}\varphi^-(t')^6 + \frac{1}{120}\varphi^-(t)\varphi^-(t')^5 + \frac{1}{120}\varphi^-(t)^5\varphi^-(t') \\
& -\frac{1}{48}\varphi^-(t)^2\varphi^-(t')^4 - \frac{1}{48}\varphi^-(t)^4\varphi^-(t')^2 + \frac{1}{36}\varphi^-(t)^3\varphi^-(t')^3]F_1(t-t') \\
& +[\frac{1}{720}\varphi^+(t)^6 - \frac{1}{720}\varphi^-(t')^6 + \frac{1}{120}\varphi^+(t)\varphi^-(t')^5 + \frac{1}{120}\varphi^+(t)^5\varphi^-(t') \\
& -\frac{1}{48}\varphi^+(t)^2\varphi^-(t')^4 - \frac{1}{48}\varphi^+(t)^4\varphi^-(t')^2 + \frac{1}{36}\varphi^+(t)^3\varphi^-(t')^3]F_2(t-t') \\
& +[\frac{1}{720}\varphi^-(t)^6 - \frac{1}{720}\varphi^+(t')^6 + \frac{1}{120}\varphi^-(t)\varphi^+(t')^5 + \frac{1}{120}\varphi^-(t)^5\varphi^+(t') \\
& -\frac{1}{48}\varphi^-(t)^2\varphi^+(t')^4 - \frac{1}{48}\varphi^-(t)^4\varphi^+(t')^2 + \frac{1}{36}\varphi^-(t)^3\varphi^+(t')^3]F_3(t-t') \}. \qquad (3.28)
\end{aligned}$$

with

$$F_1(t-t') = [\delta(t-t') - 2f_L(t-t')][\delta(t-t') - 2f_R(t'-t)] \qquad (3.29)$$

$$F_2(t-t') = 2f_L(t-t') \cdot 2[\delta(t-t') - f_R(t'-t)] \qquad (3.30)$$

$$F_3(t-t') = 2[\delta(t-t') - f_L(t-t')] \cdot 2f_R(t'-t) \qquad (3.31)$$

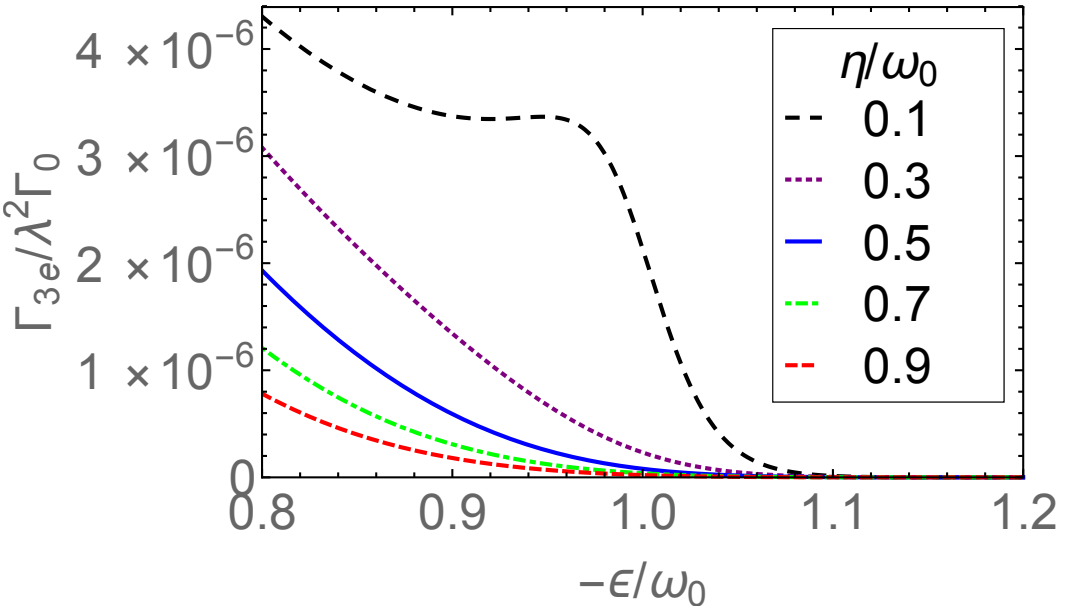

FIGURE 3.16: The three-electron contributions with different broadenings η. The bias voltage is set to be $eV/\omega_0 = 0.4$, which is corresponding to $2eV < \omega_0 < 3eV$. The SPP peak becomes clearer when the broadening is getting smaller.

By doing the Fourier transform, we can rewrite the sixth-order action of the conductor in frequency space

$$
\begin{aligned}
\mathbb{S}^{(6)}_{cond} = -\frac{1}{180}\frac{1}{(2\pi)^6}\frac{i}{8}g_c \int d\omega_1 \cdots d\omega_5 \Big\{ & \\
&\big(6\widehat{W}(\omega_1) - 15\widehat{W}(\omega_1+\omega_2) + 10\widehat{W}(-\omega_1-\omega_2-\omega_3)\big) \\
&\times[\varphi^+(\omega_1)\varphi^+(\omega_2)\varphi^+(\omega_3)\varphi^+(\omega_4)\varphi^+(\omega_5)\varphi^+(-\omega_1-\omega_2-\omega_3-\omega_4-\omega_5) \\
&\quad +\varphi^-(\omega_1)\varphi^-(\omega_2)\varphi^-(\omega_3)\varphi^-(\omega_4)\varphi^-(\omega_5)\varphi^-(-\omega_1-\omega_2-\omega_3-\omega_4-\omega_5)] \\
&-12\widehat{W}(-\omega_1)\varphi^+(\omega_1)\varphi^-(\omega_2)\varphi^-(\omega_3)\varphi^-(\omega_4)\varphi^-(\omega_5)\varphi^-(-\omega_1-\omega_2-\omega_3-\omega_4-\omega_5) \\
&-12\widehat{W}(\omega_1)\varphi^-(\omega_1)\varphi^+(\omega_2)\varphi^+(\omega_3)\varphi^+(\omega_4)\varphi^+(\omega_5)\varphi^+(-\omega_1-\omega_2-\omega_3-\omega_4-\omega_5) \\
&+30\widehat{W}(-\omega_1-\omega_2)\varphi^+(\omega_1)\varphi^+(\omega_2)\varphi^-(\omega_3)\varphi^-(\omega_4)\varphi^-(\omega_5)\varphi^-(-\omega_1-\omega_2-\omega_3-\omega_4-\omega_5) \\
&+30\widehat{W}(\omega_1+\omega_2)\varphi^-(\omega_1)\varphi^-(\omega_2)\varphi^+(\omega_3)\varphi^+(\omega_4)\varphi^+(\omega_5)\varphi^+(-\omega_1-\omega_2-\omega_3-\omega_4-\omega_5) \\
&-40\widehat{W}(-\omega_1-\omega_2-\omega_3)\varphi^+(\omega_1)\varphi^+(\omega_2)\varphi^+(\omega_3)\varphi^-(\omega_4)\varphi^-(\omega_5)\varphi^-(-\omega_1-\omega_2-\omega_3-\omega_4-\omega_5)\Big\}.
\end{aligned}
\tag{3.32}
$$

After we do the symmetrization over all ω and take the Gaussian average $\langle\langle\varphi\varphi\varphi\varphi\varphi\varphi\rangle\rangle \sim \langle\langle\varphi\rangle\rangle\langle\langle\varphi\rangle\rangle\langle\langle\varphi\varphi\rangle\rangle\langle\langle\varphi\varphi\rangle\rangle \sim \alpha^2$, at zero temperature $T = 0$, within the energy range $-3eV < \epsilon < -2eV$, only the terms like including $\langle\langle\varphi^{\pm}\rangle\rangle\langle\langle\varphi^{\mp}\rangle\rangle$

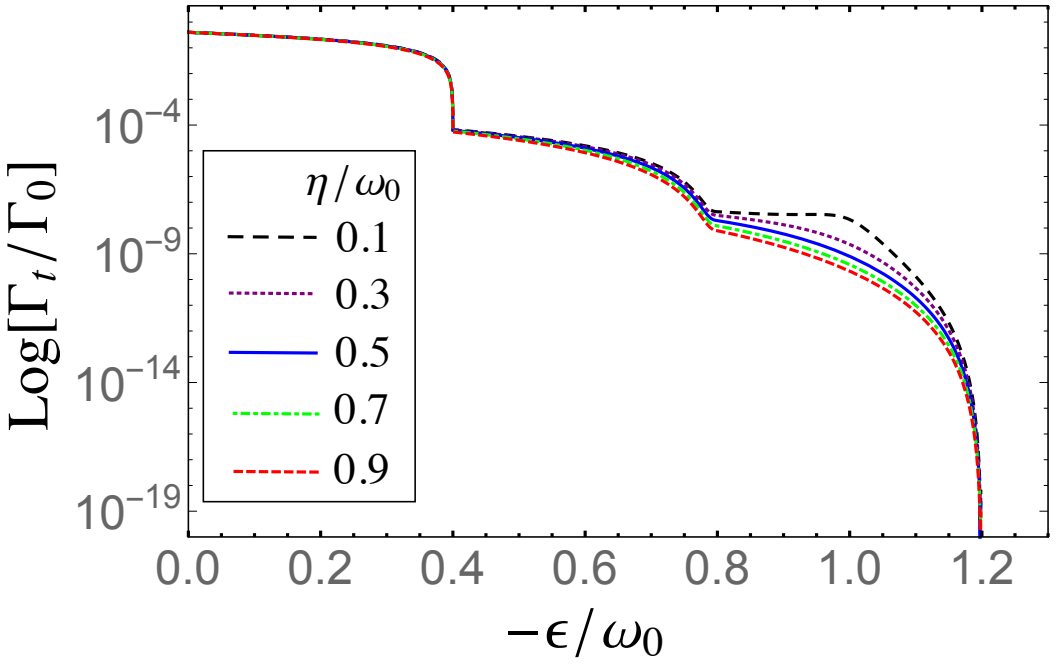

FIGURE 3.17: The total rate in Log-scale at zero temperature with different broadenings η at the bias voltage $eV/\omega_0 = 0.4$. The parameter $\lambda = g_c z_0^2 = 0.1$. The step-like stages apparently exhibit the three energy threshold at $eV, 2eV, 3eV$ and the SPP peak appears with narrow broadening.

are nonzero, thus, we can get the 3e-contribution to the lowest order in $\sim g_c^2\alpha^2$

$$\Gamma_{\rm nG}^{3e} = \frac{2\pi}{64}\alpha^2|\mathcal{T}|^2 g_c^3 \frac{|\tilde{z}_\epsilon|^2}{\epsilon^2}\iint_0^{eV} d\omega_1 d\omega_2 \frac{|\tilde{z}_{\omega_1}|^2}{\omega_1^2}\frac{|\tilde{z}_{\omega_2}|^2}{\omega_2^2}(V-\omega_1)(V-\omega_2) \times\Big(|\omega_1+\omega_2+\epsilon+V|+\omega_1+\omega_2+\epsilon+V\Big) \tag{3.33}$$

with setting the prefactor $\Gamma_0 = 4\pi^2\alpha^2|\mathcal{T}|^2 g_c z_0^2$, then the rate $\Gamma_{\rm nG}^{3e} \sim \lambda^2\Gamma_0$. The Fig. 3.16 clearly shows the dependence of the three-electron contribution on the damping parameter η in the energy range $-3eV < \epsilon < -2eV$, where you can see the SPP peak once the broadening is sharp.

Together with the other two 1e- and 2e- results above (Eq. 3.12 and Eq. 3.26), we can look into the total rate further to the three electrons tunneling processes.

In the low temperature limit $k_BT \ll eV$, it is obvious that the total emission rate can display the three thresholds at $-\epsilon = eV$, $-\epsilon = 2eV$ and $-\epsilon = 3eV$ from the separate three parts of the contributions. This has been shown in Fig. 3.17 and the SPP resonance is also shown with sharp resonance.

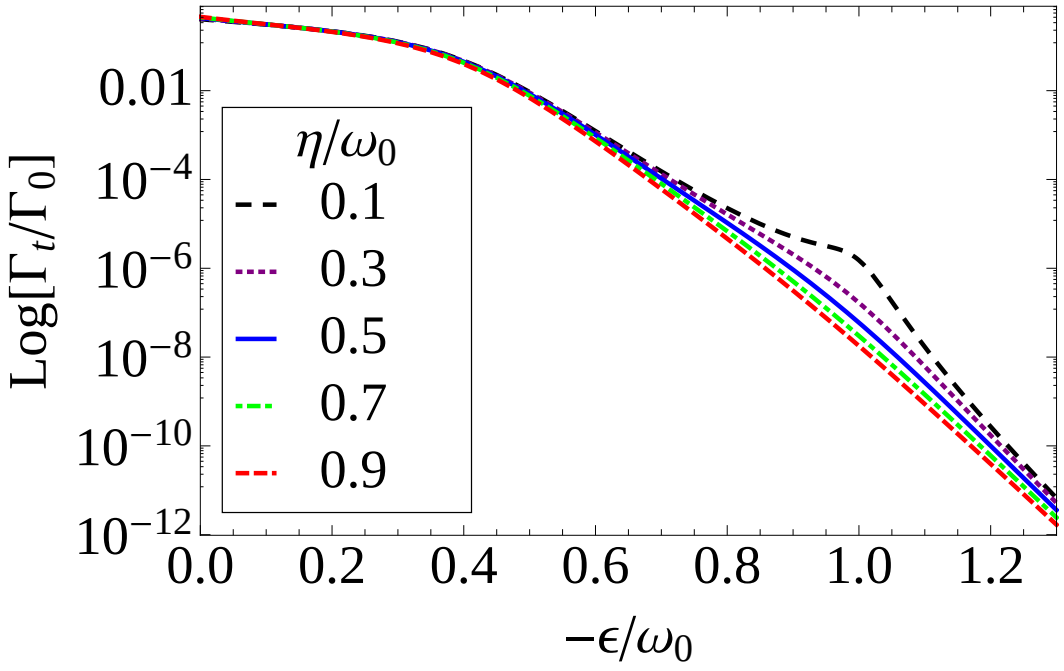

FIGURE 3.18: The total rate in Log-scale with different broadenings η at the bias voltage $eV/\omega_0 = 0.4$. The parameter $\lambda = g_c z_0^2 = 0.1$ and the temperature is set to be $k_B T/\omega_0 = 1/30$. Temperature effect smooths all the energy threshold that can be clearly seen at zero temperature.

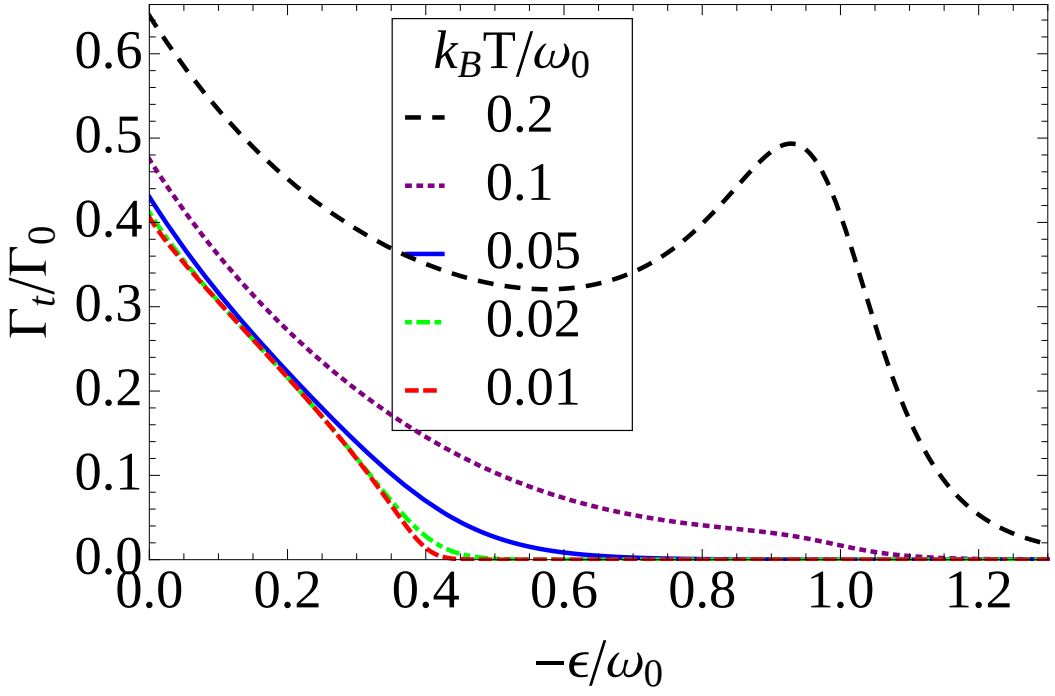

FIGURE 3.19: The total rate in Log-scale at different temperatures $k_B T$ at the bias voltage $eV/\omega_0 = 0.4$. The parameter $\lambda = g_c z_0^2 = 0.1$ and the broadening $\eta/\omega_0 = 0.3$. As the temperature increases, the cutoff edges are soften and the SPP peak shows up obviously.

And we can list the three parts as

$$\Gamma_{1e}(\epsilon) = 2\pi\alpha^2|\mathcal{T}|^2\frac{|\tilde{z}_\epsilon|^2}{\epsilon^2}S(\epsilon), \tag{3.34}$$

$$\Gamma_{2e}(\epsilon) = \frac{\pi g_c^2\alpha^2|\mathcal{T}|^2}{2}\frac{|\tilde{z}_\epsilon|^2}{\epsilon^2}\int_{-(\epsilon+eV)}^{eV} d\omega\frac{|\tilde{z}_\omega|^2}{\omega^2}S(-\omega)S(\epsilon+\omega), \tag{3.35}$$

$$\Gamma_{3e}(\epsilon) = \frac{4\pi}{64}\alpha^2|\mathcal{T}|^2 g_c^3\frac{|\tilde{z}_\epsilon|^2}{\epsilon^2}\int_{-2eV-\epsilon}^{eV} d\omega_1\int_{-eV-\epsilon-\omega_1}^{eV} d\omega_2\frac{|\tilde{z}_{\omega_1}|^2}{\omega_1^2}\frac{|\tilde{z}_{\omega_2}|^2}{\omega_2^2} S(-\omega_1)S(-\omega_2)S(\epsilon+\omega_1+\omega_2)\Theta(\omega_1+\omega_2+\epsilon+eV), \tag{3.36}$$

so, the total contribution for one photon emission can be described by

$$\Gamma_{1p}(\epsilon) = \Gamma_{1e}(\epsilon) + \Gamma_{2e}(\epsilon) + \Gamma_{3e}(\epsilon), \tag{3.37}$$

where each term just depicts the electron tunneling in the corresponding energy range.

Towards for the finite temperature case, as we know that the 3e-contribution is proportional to $g_c^3 z_0^6$, which makes the 3e-rate really small, thus, we can check how the temperature smearing the 1e and 2e cutoff at 1eV and 2eV affects the 3e rate. Fig. 3.18 and Fig. 3.19 demonstrate the dependence of the total rate at finite temperature on the broadening η and the temperature k_BT, respectively. Comparing with Fig. 3.17, in Fig. 3.18, the three energy threshold have already been smeared out since the temperature is relatively large enough and the SPP peak is still be seen with sharp enough resonance. From Fig. 3.19, it is easily seen that with the increase of the temperature, the clear cutoff becomes smoothed and the SPP resonance turns into more apparent. These properties are, as we expect, similar with previous one-electron and two-electron cases.

By assuming a featureless plasmon resonance, i.e., $|\tilde{z}_\epsilon|^2/\epsilon^2 = const$, the overall spectra consists of n=1, 2 and 3 electrons processes is shown in Fig. 3.20. The total emission clearly exhibits the characteristic kinks at the photon energies $= neV$ at low temperature, while the thresholds are broadened and shifted at $500K$ due to the smoothed Fermi distributions of electrodes.

Furthermore, currently, when we do the collaboration with the experiment

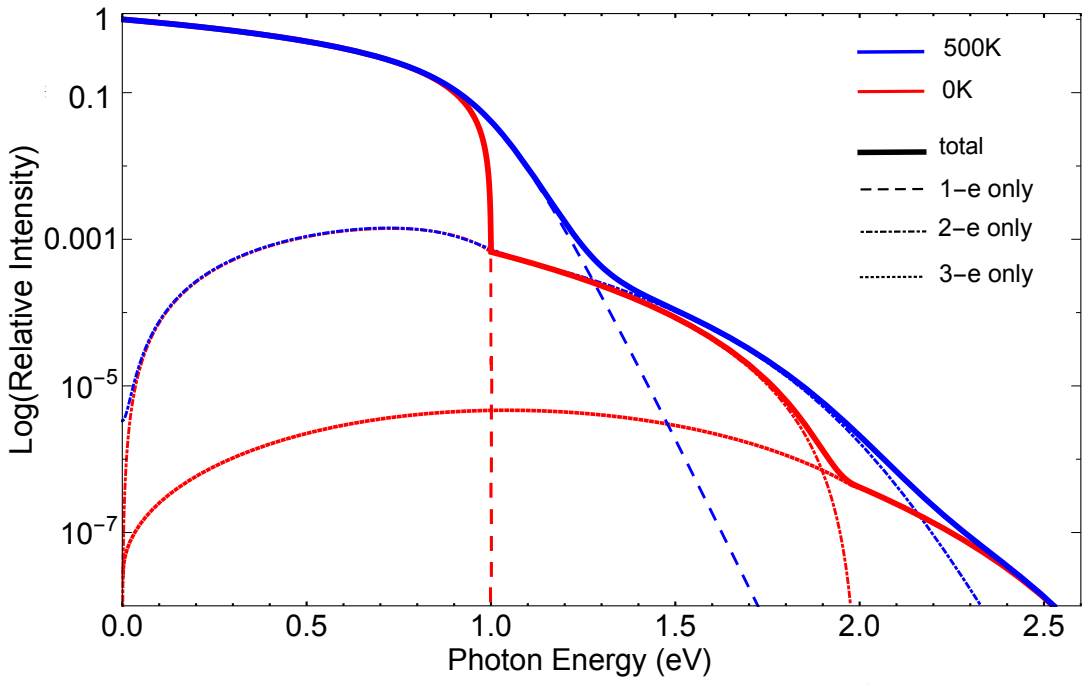

FIGURE 3.20: Emission spectra of the multi-electron processes, normalized to 1 at zero photon energy. A featureless plasmon spectrum is assumed. The respective contributions of 1e, 2e, and 3e processes are indicated by dashed, dash-dotted, and dotted lines. Solid lines show the total emission. Kinks are clearly discernible around the $n-e$ thresholds at T = 0. Temperature broadens and shifts the threshold. The coupling parameter $\tilde{g} = GG_0L/C = 0.006$ and temperatures T=0 and 500 K were separated by blue and red.

group about the three-electron tunneling processes [96], we find out that our theoretical results can reproduce the experimental observations well. Fig. 3.21 (see Fig.3a in [96]) shows a comparison of the experimental data (symbols) and our corresponding calculations (lines), in which the experiment measures the spectra at three low bias voltage V=0.9, 1 and 1.1 V, revealing the $2e-3e$ threshold. The difference in the comparison mostly occurs at photon energy $> 2eV$, where the normalization of the experimental data is less accurate.

Besides, together with the complete expressions of the $1e$ and $2e$ emissions, we can more well fit the $1e-2e$ threshold with the experimental spectra, displayed in Fig. 3.22 (see Fig.3b in [96]). The change of slope is clearly observed at the transition between the $1e$ and $2e$ spectral ranges. We find that the temperature around 50 K is giving the acceptable fit since the heating would lead to a shift of the kink the additional broadening.

Additionally, considering the unusual yield phenomena around the conductance

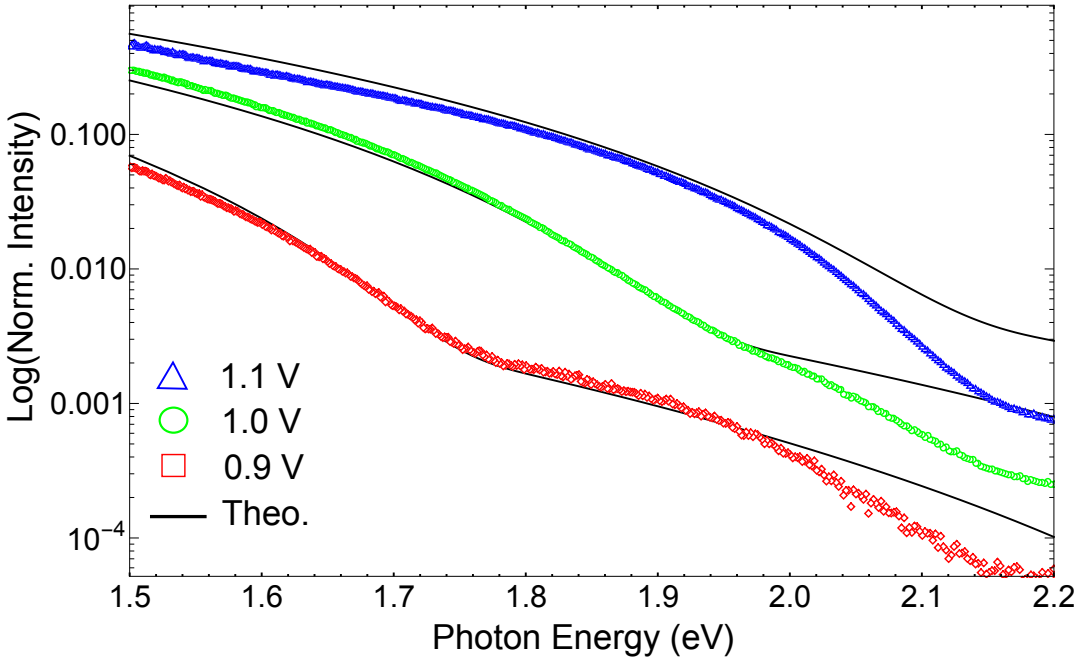

FIGURE 3.21: Spectra displayed on a logarithmic scale with three different bias voltages V=0.9V, 1V and 1.1V. Lines are fits from our calculations using the plasmon resonance ω_0=2.191eV with the broadening η=0.264eV at temperatures 20K, 21K and 22K. The coupling parameters $\tilde{g}$=0.053, 0.047, and 0.043, respectively. The broadening of the detector is taken as 0.0283eV.

close to G_0 (see the red and blue symbols in Fig. 3.23), we find out that it's a good way to extract the Fano-factor F from the experiments, not only for fitting the experiments, but also for extending our theoretical calculations since our former work principally limits in the tunneling limit, i.e., $F = 1$. So, from the Eq. 3.36, we've got the three-electron contribution in the tunnelling limit and at zero temperature, which can be expressed with the noise spectral density $S(\epsilon)$. Thus, we can generalise the noise spectrum$S(\epsilon)$ into the two-channel transmission case and rewrite the noise $S(\epsilon)$ with the Fano factor F as $S(\epsilon) \sim gF\tilde{S}(\epsilon)$, with $g = G/G_0$ and $\tilde{S}(\epsilon)$ scaled function. After doing the integral of ϵ to get the yield, which is observed in the experiments, the three-electron yield function is then proportional to g^2F^3.

We extract the behaviour of $F(g)$ from the red triangles and blue dots, which represent different tips using in the experiments, i.e., the FIG.4 in Ref. [96] (see the green dots and stars in Fig. 3.23). Then we do the numerical fitting and find the best fitting functions of $F(g)$, which has been depicted in the Fig. 3.23 with green lines.

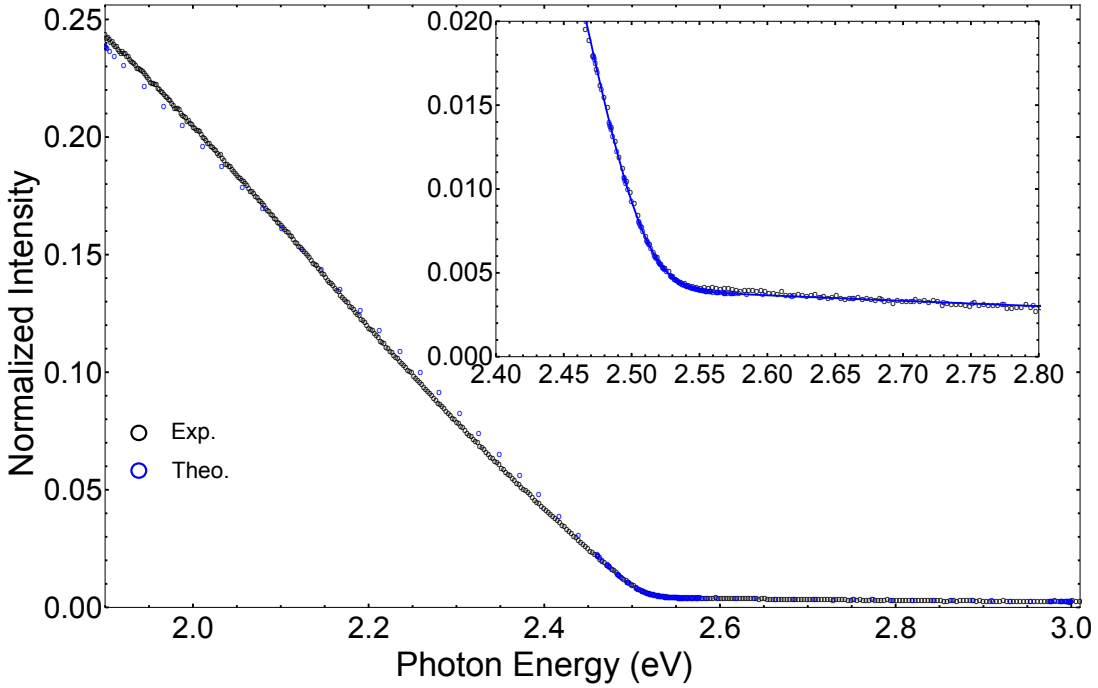

FIGURE 3.22: Spectrum of the threshold for 2e light measured at 2.5 V normalized with 3.5 V data. The line is the fit from our calculation at the bias V=2.5 V and the temperature T=55K, which reproduces the position of the kink as well as its rounding. The other parameters are ω_0= 2eV with the damping η=1eV and the coupling parameter $\tilde{g}$=0.011. The broadening of the detector is taken as =0.044eV. Zoomed data has been vertically shifted by 0.1 for clarity.

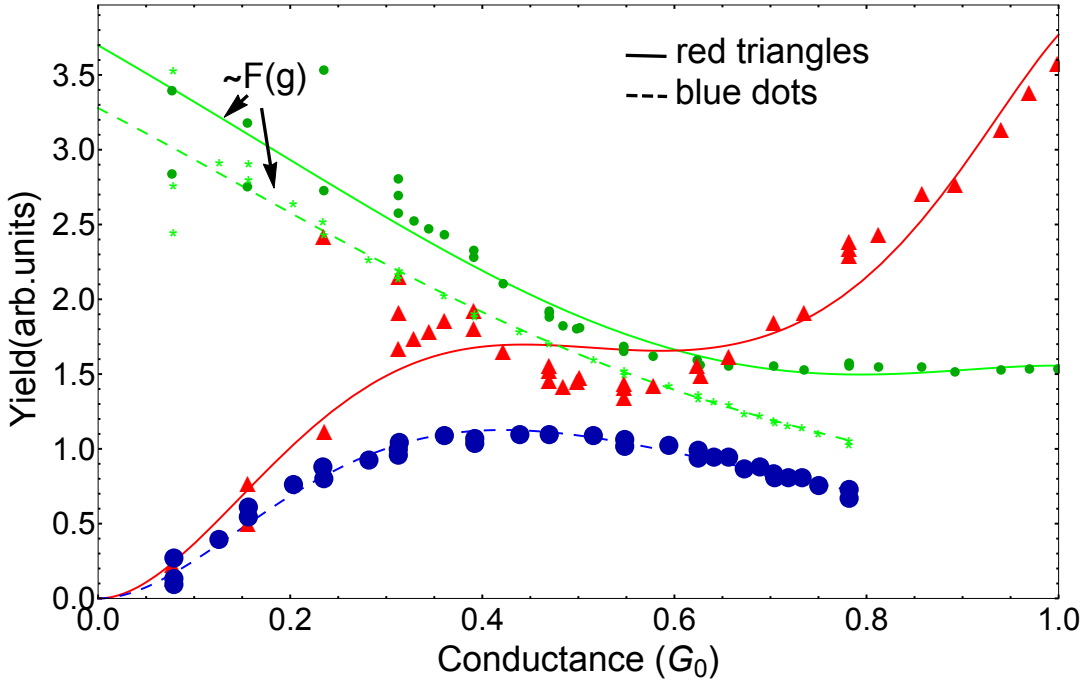

FIGURE 3.23: Solid lines describe the fitting three-electron yield with the red triangles tip and dashed lines for the blue dots tip. Green dots and stars give $\sim F(g)$ extracted from the red triangles and blue dots separately.

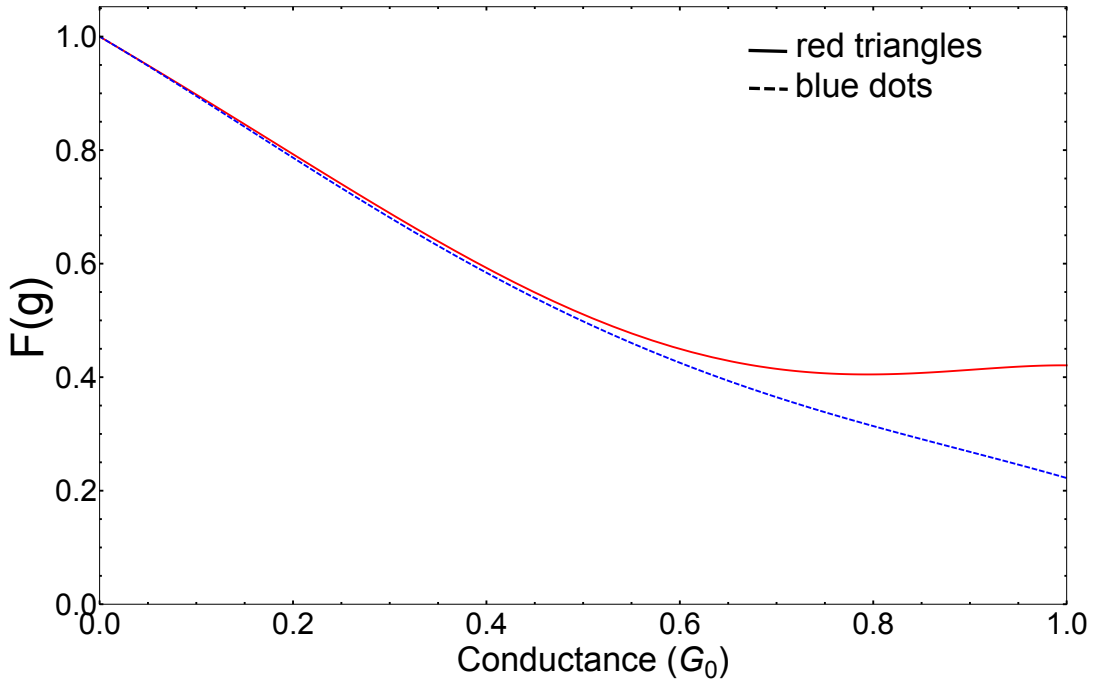

FIGURE 3.24: Red solid line and blue dashed line are the $F(g)$ after doing the scaling to the original Fano-factor $\sim F(g)$ extracted directly from the experiments, i.e., green lines in Fig. 3.23.

By the simple scaling with the known property of Fano-factor $F(0) = 1$, we can get the numerical fitting of the $F(g)$ as shown in Fig. 3.24.

For the general two-channel case, we know that the Fano factor F and the conductance g can be written as

$$g = T_1 + T_2, \tag{3.38}$$

$$F = \frac{T_1(1-T_1) + T_2(1-T_2)}{T_1 + T_2}. \tag{3.39}$$

Then, from the numerical fitting $F(g)$ we use above, we can obtain the corresponding conductance-dependent transmission functions $T_1(g)$ and $T_2(g)$ for the two channels. And the evolutions of these transmission functions can be seen in Fig. 3.25.

Finally, by introducing the conductance-dependent Fano-factor $F(g)$ and the corresponding transmission functions $T(g)$, we've found a possibility to well explain the unusual behaviour of the yield when closing to the quantum conductance

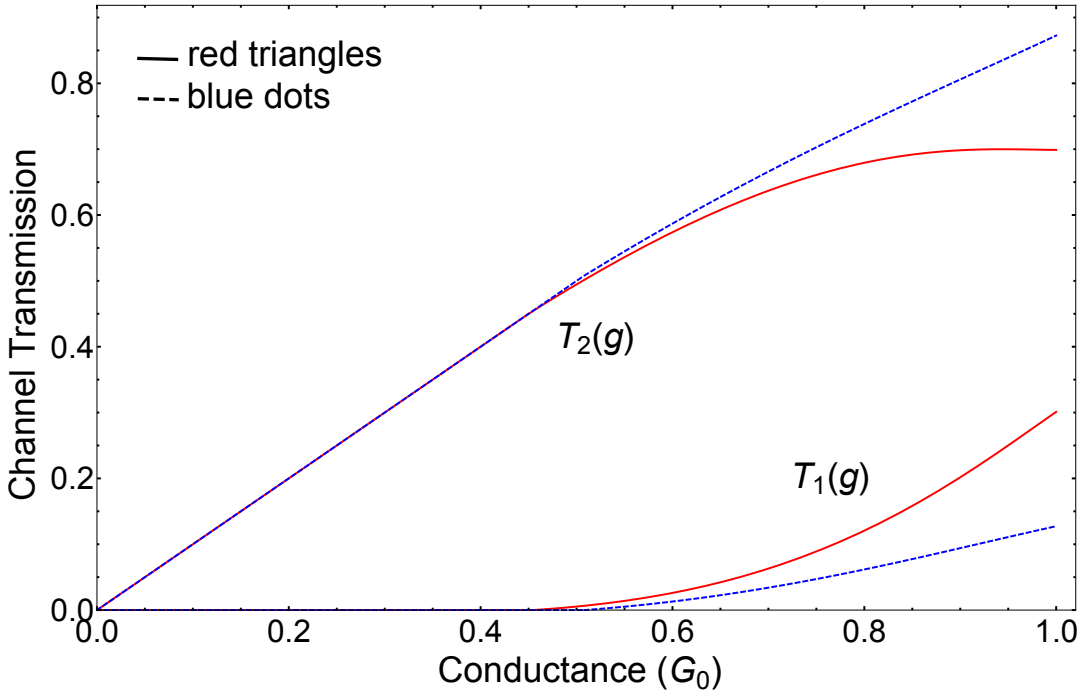

FIGURE 3.25: Red and blue lines show the $T_1(g)$ and $T_2(g)$ for the red triangles tip and blue dots tip, respectively.

G_0. We think that this can also help us solve the problem beyond the tunneling limit and we hope that we will have more interesting results in the future.

3.8 Conclusion

To summarize, motivated by the experimental observation of photons emitted by tunnel junctions carrying the energy larger than the bias voltage $|\epsilon| > eV$, we have developed a theoretical model to describe the electron-SPP mode interaction based on the dynamical Coulomb blockade theory.

In combination with the Keldysh path integral formalism, by treating the Gaussian and non-Gaussian contributions separately, our theory has shown that the non-Gaussian fluctuations give rise to the overbias photon emission, which can explain and reproduce the experimentally observed photon emission with energies larger than the single-particle energy limit eV. Furthermore, due to the smeared edge of the Fermi distribution function at finite temperature, our result also shows

that the electron tunneling is sensitively affected by the temperature, thus influencing the overbias emission. The critical point at the bias voltage $-\epsilon = eV$ is strongly weakened, and the overbias peak becomes a mixture of the Gaussian and non-Gaussian noise.

In addition, we also consider the interesting case when the bias voltage is far from the SPP resonance; here we set the resonance close to the two-electron energy limit, and we argue that this regime is suitable to distinguish the Gaussian and non-Gaussian contributions even at finite temperature and in the case of sharp resonance.

Besides, we even do the expansion of the calculation for the three-electron tunneling processes, rewrite the expressions of the one-photon emission from the one-electron, two-electron and three electron tunneling cases and check their relative properties. Finally, comparing with the experimental observations, we show a good agreement of the $1e - 2e$ and $2e - 3e$ threshold and present a strategy through the conductance-dependent Fano-factor $F(g)$ and transmission functions $T(g)$ to figure out the problem beyond the tunneling limit and numerically fit the experimental results nicely. Our work enables to model the electron-SPP mode interaction in nanosize contacts and we believe that it can be applied to more complex junctions in the future.

Chapter 4

Conclusions and outlook

In this work, we start from the current noise, which can be characterised as photon emission/absorption probability during electron tunneling processes through a mesoscopic tunnel junction. By introducing a phase operator φ, describing the voltage fluctuation due to the electron tunneling, we show how to treat the coupling between the electrical current and the electromagnetic environment through the P(E) theory or Keldysh path integral method. These approaches hence provide a way to investigate the electronic properties under the electromagnetic environment which will in addition influence the voltage fluctuations.

Motivated by the interesting phenomena of the experimental observation of photons with overbias energies emitted from a STM junction, we develop and establish a model circuit, coupled to the photon detector which is mimiced by a simple two-level system, to study the electron-surface plasmon polariton (SPP) interaction and explain this nontrivial overbias photon emission. By considering the transition rate occurring in the detector, we first consider the quadratic-case, i.e., a Gaussian form of the action, and verify our calculations through the P(E) theory, confirming that it can not give rise to the overbias photon emission. Thus, we go beyond the Gaussian regime, expand the action of the tunnel junction into the higher-order non-Gaussian terms and combine it with the Keldysh path integral method. We find the expression for the transition rate in a detector under the influence of non-Gaussian fluctuations. With the numerical simulation, we analyse the rate separately and figure out that the non-Gaussian contribution is

the one which should be responsible to the overbias light emission appearing in the experiments. And our results gives a good explanation and well reproduces the experimentally detected bias-dependent emission spectrum.

Furthermore, we proceed and derive the more general expression at finite temperature. Since the temperature smears out the Fermi edge, unlike at zero temperate, with a sharp cutoff at the bias voltage eV, the threshold is also smoothed out. Meanwhile, we find out that the transition rate exhibits a very sensitive dependence on the temperature. In combination with the clear energy threshold at low temperature, we propose a feasible technique to tell apart the Gaussian and non-Gaussian rates, by setting the SPP resonance far from the bias voltage. Finally, we also look into the properties of the intensity of the overbias light emission as a function of the temperature, from which we find that for the high enough temperature, the heating effect smears out the Fermi edge and leads to a saturation of the non-Gaussian emission. Thus, one can study the temperature dependence of the overbias light emission in order to distinguish thermally induced emission from the pure quantum effect at low temperatures.

Additionally, we explore the sixth-order contribution with the same methods and it gives the three-electron tunneling processes, which is also of great interest for the experiments. In fact, three-electron light emission has been observed and is fully consistent with our model of a multichannel atomic contact. In particular, we show that heating effects can be disregarded and the light emission is a quantum emission process.

Finally, our research enables a new level of modeling electron-SPP interaction in nano-size contacts. Considering the present limit and approximations we have used, there will be open questions concerning going beyond the tunnelling limit, the weak coupling regime, even higher-order contributions or considering the effect of molecules in the junction.

Appendix A

Derivation of non-Gaussian rate

Here, we describe some useful intermediate results for the derivation of the non-Gaussian rate, Eq. (3.26) and the expansion of the action of tunnel conductor $\mathbb{S}_c$ to the fourth order in the fluctuating fields.

According to the Gaussian average list $\langle\langle\Phi_\omega\rangle\rangle$ and $\langle\langle\Phi_\omega\Phi^T_{-\omega}\rangle\rangle$, we obtain

$$\begin{aligned}
\langle\langle\varphi^+(\omega)\rangle\rangle &= i\alpha[Y(\omega)e^{i\omega t} - X(\omega)], && \text{(A.1)}\\
\langle\langle\varphi^-(\omega)\rangle\rangle &= i\alpha[Q(\omega)e^{i\omega t} - P(\omega)], && \text{(A.2)}\\
\langle\langle\varphi^+_\omega\varphi^+_{\omega'}\rangle\rangle &= 2\pi X(\omega)\delta(\omega+\omega'), && \text{(A.3)}\\
\langle\langle\varphi^+_\omega\varphi^-_{\omega'}\rangle\rangle &= 2\pi Y(\omega)\delta(\omega+\omega'), && \text{(A.4)}\\
\langle\langle\varphi^-_\omega\varphi^+_{\omega'}\rangle\rangle &= 2\pi P(\omega)\delta(\omega+\omega'), && \text{(A.5)}\\
\langle\langle\varphi^-_\omega\varphi^-_{\omega'}\rangle\rangle &= 2\pi Q(\omega)\delta(\omega+\omega'), && \text{(A.6)}
\end{aligned}$$

with

$$\begin{aligned}
X(\omega) &= S_{nc}(\omega)\frac{|\tilde{z}_\omega|^2}{\omega^2} + \frac{1}{\omega^2}[W(\omega)Re\{\tilde{z}_\omega\} + i\omega Im\{\tilde{z}_\omega\}], && \text{(A.7)}\\
Y(\omega) &= S_{nc}(\omega)\frac{|\tilde{z}_\omega|^2}{\omega^2} + \frac{1}{\omega^2}[W(\omega)-\omega]Re\{\tilde{z}_\omega\}, && \text{(A.8)}\\
P(\omega) &= S_{nc}(\omega)\frac{|\tilde{z}_\omega|^2}{\omega^2} + \frac{1}{\omega^2}[W(\omega)+\omega]Re\{\tilde{z}_\omega\}, && \text{(A.9)}\\
Q(\omega) &= S_{nc}(\omega)\frac{|\tilde{z}_\omega|^2}{\omega^2} + \frac{1}{\omega^2}[W(\omega)Re\{\tilde{z}_\omega\} - i\omega Im\{\tilde{z}_\omega\}], && \text{(A.10)}
\end{aligned}$$

with $S_{nc}(\omega) = g_c[\frac{1}{2}W(\omega+eV) + \frac{1}{2}W(\omega-eV) - W(\omega)]$.

After performing the symmetrization over ω, we yield

$$\begin{aligned}\langle\langle \mathbb{S}_c^{(4)}\rangle\rangle = -\frac{i\pi\alpha^2 g_c}{16}\iint d\omega d\omega' \Big\{ & [Y(\omega')e^{i\omega' t} - X(\omega')][Y(-\omega')e^{-i\omega' t} - X(-\omega')] \\ & \Big[X(\omega)[-F(0)+2F^s(\omega)+2F^s(\omega')-2F^{ss}(-\omega-\omega')] \\ & \quad +Q(\omega)F(0) - P(\omega)F(\omega) - Y(\omega)F(-\omega)\Big] \\ & +[Q(\omega')e^{i\omega' t} - P(\omega')][Q(-\omega')e^{-i\omega' t} - P(-\omega')]\Big[Q(\omega)[-F(0)+2F^s(\omega)+2F^s(\omega') \\ & -2F^{ss}(-\omega-\omega')] - P(\omega)F(\omega) - Y(\omega)F(-\omega) + X(\omega)F(0)\Big] \\ & +[Y(\omega')e^{i\omega' t} - X(\omega')][Q(-\omega')e^{-i\omega' t} - P(-\omega')]\Big[- [Q(\omega) + X(\omega)]F(-\omega') \\ & \quad +Y(\omega)F(-\omega-\omega') + P(\omega)F(\omega-\omega')\Big] \\ & +[Q(\omega')e^{i\omega' t} - P(\omega')][Y(-\omega')e^{-i\omega' t} - X(-\omega')]\Big[- [Q(\omega) + X(\omega)]F(\omega') \\ & \quad +Y(\omega)F(-\omega+\omega') + P(\omega)F(\omega+\omega')\Big]\Big\} \end{aligned} \tag{A.11}$$

with the defined functions $F^s(\omega) = [F(\omega)+F(-\omega)]/2$ and $F^{ss}(-\omega-\omega') = [F(-\omega-\omega') + F(-\omega+\omega') + F(\omega-\omega') + F(\omega+\omega')]/4$, in which $F(\omega) = F_1(\omega) + F_2(-\omega) = (-\omega - eV) + W(-\omega - eV) + (-\omega + eV) + W(-\omega + eV)$ as given in the text.

One can show that the terms proportional to $e^{i\omega' t}$ and the ones proportional to $e^{-i\omega' t}$, are interchanged under the operation $\omega' \to -\omega'$. Using $\int e^{i\omega t}e^{i\epsilon t}dt = 2\pi\delta(\omega+\epsilon)$ and keeping the terms in the lowest order of $g_c Z_0^2$, the non-Gaussian rate Eq. (3.26) can be expressed as

$$\begin{aligned}\Gamma_{\rm nG}^{(4)} = \frac{\pi^2\alpha^2|\mathcal{T}|^2 g_c}{4}\int d\omega \Big\{ & Y(-\epsilon)X(\epsilon)\Big[X(\omega)[-F(0)+2F^s(\omega)+2F^s(\epsilon) \\ & -2F^{ss}(-\omega+\epsilon)] - P(\omega)F(\omega) - Y(\omega)F(-\omega) + Q(\omega)F(0)\Big] \\ & +Q(-\epsilon)P(\epsilon)\Big[Q(\omega)[-F(0)+2F^s(\omega)+2F^s(\epsilon)-2F^{ss}(-\omega+\epsilon)] \\ & \quad -P(\omega)F(\omega) - Y(\omega)F(-\omega) + X(\omega)F(0)\Big] \\ & +Y(-\epsilon)P(\epsilon)\Big(- [Q(\omega) + X(\omega)]F(\epsilon) + Y(\omega)F(-\omega+\epsilon) + P(\omega)F(\omega+\epsilon)\Big) \\ & +Q(-\epsilon)X(\epsilon)\Big(- [Q(\omega)+X(\omega)]F(-\epsilon) + Y(\omega)F(-\omega-\epsilon) + P(\omega)F(\omega-\epsilon)\Big)\Big\} \end{aligned} \tag{A.12}$$

This expression can be cast as Eq. (3.26) in the main text after replacing all the functions, i.e., X, Y, P, Q and F, by their definitions.

Bibliography

[1] R. P. Feynman. Space-time approach to non-relativistic quantum mechanics. *Rev. Mod. Phys.*, 20:367–387, 1948.

[2] L. H. Ryder. *Quantum Field Theory*. Cambridge University Press, 1985.

[3] P. Ramond. *Field Theory: A Modern Primer*. Westview Press, 1997.

[4] E. Fradkin. *Field Theories of Condensed Matter Systems*. Cambridge University Press, 1991.

[5] A. M. Tsvelik. *Quantum Field Theory in Condensed Matter Physics*. Cambridge University Press, 1995.

[6] R.P. Feynman and A.R. Hibbs. *Quantum Mechanics and Path Integrals*. McGraw-Hill Companies, 1965.

[7] G. Baym. *Lectures on Quantum Mechanics*. Westview Press, 1974.

[8] G. D. Mahan. *Many - particle physics*. Plenum Press, 1990.

[9] R. P. Feynman. *Statistical Mechanics: A Set of Lectures*. Westview Press, 1998.

[10] E. M. Lifshitz. *Statistical Physics, Part 2: Theory of Condensed state*. Pergamon Press, 1980.

[11] A. A. Abrikosov, L. P. Gorkov, and I. E. DzyaloshinskiI. *Methods of Quantum Field Theory in Statistical Physics*. Pergamon Press, 1965.

[12] J. W. Negele and H. Orland. *Quantum Many-Particle Systems*. Westview Press, 1988.

[13] A. Kamenev. Keldysh and doi-peliti techniques for out-of-equilibrium systems. *cond-mat/0109316*, 2001.

[14] A. Kamenev. Many-body theory of non-equilibrium systems. *cond-mat/0412296v2*, 2001.

[15] A. I. Larkin and Yu. N. Ovchinnikov. *Vortex motion in Superconductors, in Nonequilibrium Superconductivity.* eds. D. N. Langenberg, A. I. Larkin, Elsevier, 1986.

[16] H. Raether. *Surface Plasmons on Smooth and Rough Surfaces and on Gratings.* Springer, Berlin, Heidelberg, 1988.

[17] Anatoly V. Zayats, Igor I. Smolyaninov, and Alexei A. Maradudin. Nano-optics of surface plasmon polaritons. *Physics Reports*, 408:131–314, 2005.

[18] H. Raether. *Physics of Thin Films.* eds. Hass, G. and Francombe, M. H. and Hoffman, R. W., Academic Press, New York, 1977.

[19] S. Maier. *Plasmonics: Fundamentals and Applications.* Springer, New York, 2007.

[20] T. J. Davis and D. E. Gómez. Colloquium. *Rev. Mod. Phys.*, 89:011003, Jan 2017.

[21] William L. Barnes, A. Dereux, and Thomas W. Ebbesen. Surface plasmon subwavelength optics. *Nature*, 424:824–830, 2003.

[22] Anatoly V Zayats and Igor I Smolyaninov. Near-field photonics: surface plasmon polaritons and localized surface plasmons. *Journal of Optics A: Pure and Applied Optics*, 5(4):S16, 2003.

[23] Gerd Schön. Quantum shot noise in tunnel junctions. *Phys. Rev. B*, 32: 4469–4485, 1985.

[24] G. L. Ingold, Yu. V. Nazarov, H. Grabert, and M. H. Devoret. *Single Charge Tunneling: Coulomb Blockade Phenomena In Nanostructures*, volume 294. eds. NATO ASI Series B, 1992.

[25] Hyunwoo Lee and L. S. Levitov. Current fluctuations in a single tunnel junction. *Phys. Rev. B*, 53:7383–7391, 1996.

[26] M. H. Devoret, D. Esteve, H. Grabert, G.-L. Ingold, H. Pothier, and C. Urbina. Effect of the electromagnetic environment on the coulomb blockade in ultrasmall tunnel junctions. *Phys. Rev. Lett.*, 64:1824–1827, 1990.

[27] M. H. Devoret. *Quantum fluctuations in electrical circuits.* Les Houches, Session LXIII, 1995.

[28] R. Kubo. The fluctuation-dissipation theorem. *Rep. Prog. Phys*, 29:255–284, 1966.

[29] Yu. V. Nazarov and Ya. M. Blanter. *Quantum Transport.* Cambridge University Press, 2009.

[30] Leon Van Hove. Correlations in space and time and born approximation scattering in systems of interacting particles. *Phys. Rev.*, 95:249–262, 1954.

[31] U. Gavish, Y. Levinson, and Y. Imry. Detection of quantum noise. *Phys. Rev. B*, 62:R10637–R10640, 2000.

[32] U. Gavish, Y. Imry, Y. Levinson, and B. Yurke. *What quantity is measured in an excess noise experiment?* eds. Yu. V. Nazarov, Kluwer Academic Publisher, 2002.

[33] G. B. Lesovik and R. Loosen. On the detection of finite-frequency current fluctuations. *JETP Lett.*, 65:295–299, 1997.

[34] Y. Imry. *Introduction to Mesoscopic Physics.* Oxford University Press, 2002.

[35] H. Nyquist. Thermal agitation of electric charge in conductors. *Phys. Rev.*, 32:110–113, 1928.

[36] J. B. Johnson. Thermal agitation of electricity in conductors. *Phys. Rev.*, 32: 97–109, 1928.

[37] D. V. Averin and K. K. Likharev. *Mesoscopic Phenomena in Solids.* eds. B.L. Altshuler, P.A. Lee and R.A. Webb, Elsevier, 1991.

[38] Ya. M. Blanter and M. Büttiker. Shot noise in mesoscopic conductors. *Physics Reports*, 336:1–166, 2000.

[39] A. A. Odintsov. Effect of dissipation on the characteristics of small-area tunnel junctions: Application of the polaron model. *Zh. Eksp. Teor. Fiz.*, 94: 312, 1988.

[40] D. V. Averin and A. A. Odintsov. Macroscopic quantum tunneling of the electric charge in small tunnel junctions. *Phys. Lett. A*, 140:251–257, 1989.

[41] W. H. Louisell. *Quantum Statistical Properties of Radiation*. John Wiley and Sons Canada, 1973.

[42] John Lambe and S. L. McCarthy. Light emission from inelastic electron tunneling. *Phys. Rev. Lett.*, 37:923–925, 1976.

[43] J. K. Gimzewski, B. Reihl, J. H. Coombs, and R. R. Schlittler. Photon emission with the scanning tunneling microscope. *Zeitschrift für Physik B Condensed Matter*, 72(4):497–501, 1988.

[44] R. Berndt, A. Baratoff, and J. K. Gimzewski. *in: Scanning Tunneling Microscopy and Related Methods*. eds. R. J. Behm, N. Garcia and H. Rohrer, NATO ASI Series E 184, Kluwer Academic Publisher, 1990.

[45] Richard Berndt, James K. Gimzewski, and Peter Johansson. Inelastic tunneling excitation of tip-induced plasmon modes on noble-metal surfaces. *Phys. Rev. Lett.*, 67:3796–3799, 1991.

[46] R. Berndt, James K. Gimzewski, and Reto R. Schlittler. Enhanced photon emission from the stm: a general property of metal surfaces. *Ultramicroscopy*, 42–44:355 – 359, 1992.

[47] I.I. Smolyaninov and O. Keller. Light emission from stm by means of the cherenkov effect. *Surface Science*, 331:1310–1316, 1995. ISSN 0039-6028.

[48] A. Downes and M. E. Welland. Photon emission from ag and au clusters in the scanning tunneling microscope. *Applied Physics Letters*, 72(21):2671–2673, 1998.

[49] Y. Suzuki, H. Minoda, and N. Yamamoto. Stm light emission from ag/si(111). *Surface Science*, 438:297–304, 1999. ISSN 0039–6028.

[50] N. Nilius, N. Ernst, H.-J. Freund, and P. Johansson. Photon emission spectroscopy of nial(110) in the scanning tunneling microscope. *Phys. Rev. B*, 61: 12682–12685, May 2000.

[51] Germar Hoffmann, Jörg Kliewer, and Richard Berndt. Luminescence from metallic quantum wells in a scanning tunneling microscope. *Phys. Rev. Lett.*, 87:176803, 2001.

[52] M. Iwami, Y. Uehara, and S. Ushioda. Stm light emission from si(111)-(7*7) surface using a silver tip. *Applied Surface Science*, 169–170:188–192, 2001. ISSN 0169–4332.

[53] Michael G Boyle, J Mitra, and Paul Dawson. The tip-sample water bridge and light emission from scanning tunnelling microscopy. *Nanotechnology*, 20 (33):335202, 2009.

[54] Guillaume Schull, Nicolas Néel, Peter Johansson, and Richard Berndt. Electron-plasmon and electron-electron interactions at a single atom contact. *Phys. Rev. Lett.*, 102:057401, 2009.

[55] Natalia L. Schneider, Guillaume Schull, and Richard Berndt. Optical probe of quantum shot-noise reduction at a single-atom contact. *Phys. Rev. Lett.*, 105:026601, 2010.

[56] Palash Bharadwaj, Alexandre Bouhelier, and Lukas Novotny. Electrical excitation of surface plasmons. *Phys. Rev. Lett.*, 106:226802, 2011.

[57] F. Xu, C. Holmqvist, and W. Belzig. Overbias light emission due to higher-order quantum noise in a tunnel junction. *Phys. Rev. Lett.*, 113:066801, 2014.

[58] F. Xu, C. Holmqvist, G. Rastelli, and W. Belzig. Dynamical coulomb blockade theory of plasmon-mediated light emission from a tunnel junction. *Phys. Rev. B*, 94:245111, 2016.

[59] Kristen Kaasbjerg and Abraham Nitzan. Theory of light emission from quantum noise in plasmonic contacts: Above-threshold emission from higher-order electron-plasmon scattering. *Phys. Rev. Lett.*, 114:126803, 2015.

[60] Natalia L. Schneider, Peter Johansson, and Richard Berndt. Hot electron cascades in the scanning tunneling microscope. *Phys. Rev. B*, 87:045409, 2013.

[61] M. Hofheinz, F. Portier, Q. Baudouin, P. Joyez, D. Vion, P. Bertet, P. Roche, and D. Esteve. Bright side of the coulomb blockade. *Phys. Rev. Lett.*, 106: 217005, 2011.

[62] Ciprian Padurariu, Fabian Hassler, and Yuli V. Nazarov. Statistics of radiation at josephson parametric resonance. *Phys. Rev. B*, 86:054514, 2012.

[63] M. Blencowe, A. Armour, and A. Rimberg. *Fluctuating Nonlinear Oscillators: From Nanomechanics to Quantum Superconducting Circuits.* eds. M. Dykman, Oxford University Press, 2012.

[64] A. D. Armour, M. P. Blencowe, E. Brahimi, and A. J. Rimberg. Universal quantum fluctuations of a cavity mode driven by a josephson junction. *Phys. Rev. Lett.*, 111:247001, 2013.

[65] B. Kubala, V. Gramich, and J. Ankerhold. Non-classical light from superconducting resonators coupled to voltage-biased josephson junctions. *Physica Scripta*, 2015(T165):014029, 2015.

[66] Juha Leppäkangas, Mikael Fogelström, Alexander Grimm, Max Hofheinz, Michael Marthaler, and Göran Johansson. Antibunched photons from inelastic cooper-pair tunneling. *Phys. Rev. Lett.*, 115:027004, 2015.

[67] Simon Dambach, Björn Kubala, Vera Gramich, and Joachim Ankerhold. Time-resolved statistics of nonclassical light in josephson photonics. *Phys. Rev. B*, 92:054508, 2015.

[68] T. Uemura, M. Furumoto, T. Nakano, M. Akai-Kasaya, A. Saito, M. Aono, and Y. Kuwahara. Local-plasmon-enhanced up-conversion fluorescence from copper phthalocyanine. *Chem. Phys. Lett.*, 448:232–236, 2007.

[69] A. Fujiki, Y. Miyake, Y. Oshikane, M. Akai-Kasaya, A. Saito, and Y. Kuwahara. Stm-induced light emission from thin films of perylene derivatives on the hopg and au substrates. *Nanoscale Research Letters*, 6(1):347, 2011.

[70] Z.-C. Dong, X.-L. Guo, A. S. Trifonov, P. S. Dorozhkin, K. Miki, K. Kimura, S. Yokoyama, and S. Mashiko. Vibrationally resolved fluorescence from organic molecules near metal surfaces in a scanning tunneling microscope. *Phys. Rev. Lett.*, 92:086801, 2004.

[71] Z.-C. Dong, X. L. Zhang, H. Y. Gao, Y. Luo, C. Zhang, L. G. Chen, R. Zhang, X. Tao, J. L. Yang, and J. G. Hou. Generation of molecular hot electroluminescence by resonant nanocavity plasmons. *Nat. Photon.*, 4:50–54, 2010.

[72] J. Tobiska, J. Danon, I. Snyman, and Yu. V. Nazarov. Quantum tunneling detection of two-photon and two-electron processes. *Phys. Rev. Lett.*, 96: 096801, 2006.

[73] M. Kindermann and Yu. V. Nazarov. Interaction effects on counting statistics and the transmission distribution. *Phys. Rev. Lett.*, 91:136802, 2003.

[74] Yu. V. Nazarov. Universalities of weak localization. *Ann. Phys.*, 8:SI–193, 1999.

[75] W. Belzig and Yu. V. Nazarov. Full counting statistics of electron transfer between superconductors. *Phys. Rev. Lett.*, 87:197006, 2001.

[76] H. Haken. Cooperative phenomena in systems far from thermal equilibrium and in nonphysical systems. *Rev. Mod. Phys.*, 47:67–121, 1975.

[77] A. O. Caldeira and A. J. Leggett. Quantum tunnelling in a dissipative system. *Ann. Phys.*, 149:374–456, 1983.

[78] Ramón Aguado and Leo P. Kouwenhoven. Double quantum dots as detectors of high-frequency quantum noise in mesoscopic conductors. *Phys. Rev. Lett.*, 84:1986–1989, 2000.

[79] G. B. Lesovik. Excess quantum noise in 2d ballistic point contacts. *JETP Lett.*, 49:592, 1989.

[80] B. Yurke and G. P. Kochanski. Momentum noise in vacuum tunneling transducers. *Phys. Rev. B*, 41:8184–8194, 1990.

[81] Yu. V. Nazarov. *Quantum Noise in Mesoscopic Physics*. Proceedings of the NATO Advanced Research Workshop, 2002, Delft, Kluwer Academic Publisher,, 2003.

[82] Arnold Adams and P. K. Hansma. Light emission from small metal particles and thin metal films excited by tunneling electrons. *Phys. Rev. B*, 23:3597–3601, 1981.

[83] M. J. Bloemer, J. G. Mantovani, J. P. Goudonnet, D. R. James, R. J. Warmack, and T. L. Ferrell. Observation of driven surface-plasmon modes in metal particulates above tunnel junctions. *Phys. Rev. B*, 35:5947–5954, 1987.

[84] A. Köck, W. Beinstingl, K. Berthold, and E. Gornik. Surface plasmon polariton enhanced light emission from schottky diodes. *Appl. Phys. Lett.*, 52: 1164, 1988.

[85] R. W. Rendell, D. J. Scalapino, and B. Mühlschlegel. Role of local plasmon modes in light emission from small-particle tunnel junctions. *Phys. Rev. Lett.*, 41:1746–1750, 1978.

[86] Bernardo Laks and D. L. Mills. Photon emission from slightly roughened tunnel junctions. *Phys. Rev. B*, 20:4962–4980, 1979.

[87] B. N. J. Persson and A. Baratoff. Theory of photon emission in electron tunneling to metallic particles. *Phys. Rev. Lett.*, 68:3224–3227, 1992.

[88] R. J. Schoelkopf, A. A. Clerk, S. M. Girvin, K. W. Lehnert, and M. H. Devoret. *in: Quantum Noise in Mesoscopic Physics*. eds. Yu.V. Nazarov, Proceedings of the NATO Advanced Research Workshop, 2002, Delft, Kluwer Academic Publisher, 2003.

[89] N. L. Schneider, J. T. Lü, M. Brandbyge, and R. Berndt. Light emission probing quantum shot noise and charge fluctuations at a biased molecular junction. *Phys. Rev. Lett.*, 109:186601, 2012.

[90] A. Burtzlaff, N. L. Schneider, A. Weismann, and R. Berndt. Shot noise from single atom contacts in a scanning tunneling microscope. *Surf. Sci.*, 643: 10–12, 2016.

[91] Germar Hoffmann, Richard Berndt, and Peter Johansson. Two-electron photon emission from metallic quantum wells. *Phys. Rev. Lett.*, 90:046803, 2003.

[92] A. Downes, Ph. Dumas, and M. E. Welland. Measurement of high electron temperatures in single atom metal point contacts by light emission. *Appl. Phys. Lett.*, 81:1252, 2002.

[93] R. Pechou, R. Coratger, F. Ajustron, and J. Beauvillain. Cutoff anomalies in light emitted from the tunneling junction of a scanning tunneling microscope in air. *Appl. Phys. Lett.*, 72:671, 1998.

[94] J. W. Gadzuk and E. W. Plummer. Hot-hole-electron cascades in field emission from metals. *Phys. Rev. Lett.*, 26:92–95, 1971.

[95] Michael Galperin and Abraham Nitzan. Molecular optoelectronics: the interaction of molecular conduction junctions with light. *Phys. Chem. Chem. Phys.*, 14:9421–9438, 2012.

[96] Peter-Jan Peter, Fei Xu, Kristen Kaasbjerg, Gianluca Rastelli, Wolfgang Belzig, and Berndt Richard. Quantum coherent multi-electron processes in an atomic scale contact. *unpublished*, 2017.